To the Graduate Council:

I am submitting herewith a dissertation written by Jude Atogho Abia entitled "Radial Heterogeneity and Surface Properties of Columns Used in High Performance Liquid Chromatography." I have examined the final electronic copy of this dissertation for form and content and recommend that it be accepted in partial fulfillment of the requirements for the degree of Doctor of Philosophy, with a major in Chemistry.

Georges Guiochon
Major Professor

We have read this dissertation
and recommend its acceptance:

Frank Vogt

Michael Best

Rebecca Prosser

Accepted for the Council:

Carolyn R. Hodges
Vice Provost and Dean of the Graduate School

(Original signatures are on file with official student records.)

Radial Heterogeneity and Surface Properties of Columns Used in High Performance Liquid Chromatography

A Dissertation Presented for

the Doctor of Philosophy

Degree

The University of Tennessee, Knoxville

Jude Atogho Abia

May 2010

DEDICATION

I dedicated this dissertation to my parents (Lucy and Lucas Abia) who have always encouraged me to study hard and be a good student. Also, I especially thank my wife (Tomia Abia) and baby girl (Paris-Pearl Bessem Abia) for their loyal support.

ACKNOWLEDGMENTS

I sincerely thank my advisor Prof. Georges Guiochon for his wonderful support during my graduate research. I also will like to thank Dr. Youngmi Lee who afforded me a head start in her research group during her tenure at the department of chemistry.

I also express my appreciation to Dr. Frank Vogt, Dr. Michael Best, and Dr. Rebecca Prosser for accepting to become members of my dissertation committee.

For offering me an opportunity to pursue a Ph.D. program in Chemistry, I sincerely thank the faculty of the department of Chemistry at the University of Tennessee.

I wholeheartedly thank my family members (Irene Abia-Angeh, Jerry Angeh, Sandy-Sheryl Angeh, and Kyra-Kay Angeh) for their unflinching support all throughout my study program.

I want to take this opportunity to express my most sincere gratitude to all the people who helped to make this work possible. Above all else, credit goes to God, through whom I have the strength to accomplish any task.

ABSTRACT

The radial heterogeneity of some columns used in high performance liquid chromatography (HPLC) was investigated using an on-column microelectrochemical amperometric detector. Such a detector allowed the recording of the elution profiles at different spatial positions throughout the column exit cross-section. From this, we obtain information about the radial distribution of the mobile phase velocity, column efficiency, and analyte concentration. In all cases, the results obtained show that the spatial distribution of the mobile phase velocity does not follow a piston-flow behavior but exhibits radial heterogeneity with differences not exceeding 5% between the center and wall regions of any column. The efficiency was found to be lower in the wall region of the column than in its core region (the central core with a radius of 1/3 the column inner radius) by up to 40-50% in some columns. The radial distribution of the maximum concentration of the peaks varies throughout the column exit section, partially due to the radial variations of the column efficiency. The technology used in constructing the microelectrochemical detectors was further exploited to fabricate and incorporate an online detector array for a pressurized flat wide column measuring 10x10x0.1 cm in dimensions. Thus, unlike traditional thin layer chromatography, samples in this pressurized flat bed are completely eluted and detected in a time-based mode just like they are in HPLC. Also, a lateral arrangement of the detector array allows for an easy monitoring of the homogeneity of the flat wide column. Also, information on the

surface properties of three novel chemically bonded phase packing materials for HPLC was obtained using solid state cross-polarization (CP) magic-angle spinning (MAS) nuclear magnetic resonance (NMR) spectroscopic experiments for the ^{29}Si, and ^{13}C nuclei. These packing materials were: Cogent bidentate C_{18} bonded to type-C silica, hybrid packing materials XTerra MS C_{18}, and XBridge Prep. C_{18}. The spectra obtained using cross-polarization magic angle spinning (CP-MAS) on the Cogent bidentate C_{18} bonded to type-C silica show the surface to be densely populated with hydride groups (Si-H), with a relative surface coverage exceeding 80%. The hybrid packing materials XTerra and XBridge gave spectra that reveal the silicon atoms to be bonded to alkyl moieties embedded in the molecular structure of these materials with over 90% of the alkyl silicon atoms found within the completely condensed silicon environments.

TABLE OF CONTENTS

Abstract IV

List of Tables X

List of Figures XI

Chapter 1 1

Introduction and Background 1

1.1. Introduction to Colum Heterogeneity 1

1.2. The Objectives of High Performance Liquid Chromatography 3

1.3. Methods for Consolidating HPLC Columns 4

1.4. Descriptors of Column Performance 8

1.4.1. Column Permeability 8

1.4.2. Analysis Time 9

1.4.3. Column Efficiency 10

1.4.4. Bed Homogeneity 14

1.5. Recent Advances in Column Technology 15

1.5.1. Surface Properties of Some Recent Packing Materials 17

1.5.2. Characterization of the Surface Properties of Some Recent Packing Materials Using Solid State NMR 23

1.6. Reasons for Radial Heterogeneity within Particle Packed Columns 25

1.7. Reasons for Radial Heterogeneity within Monolithic Columns 26

1.8. Methods for Investigating Column Heterogeneity 28

1.8.1. Visual Method 28

1.8.2. Spectroscopic Method 29

1.8.3. Electrochemical Method 30

1.9 Research Objectives 31

Chapter 2 32

Experimental 32

2.1. Materials and Chemicals 32

2.2. Instrumentation and Experimental Conditions 35

2.3. Process for Local Detection 37

2.3.1. Fabrication and Description of the Microelectrochemical Detector Ensemble 37

2.4. Column Setup for Measuring Radial Heterogeneity 42

2.4.1. Setup for Monolithic and Particle-Packed Columns 42

2.4.2. Setup for Flat Wide Column 45

2.4.2.1. Instrumentation 45

2.4.2.2. Column Housing 45

2.4.2.3. Column Bed Preparation 49

2.4.2.4. Operation of the Instrument 50

2.5. Microelectrochemical Detector setup 51

2.6. Calibration 53

Chapter 3 54

Results and Discussion 54

3.1 Figures of Merits of the Electrochemical Detector 54

3.2. Distributions of the Mobile Phase Velocities 58

3.2.1. At the Exit Cross Section of the Particle Packed Columns 58

3.2.2. At the Exit Cross Section of the Monolithic Columns 62

3.2.3. At the Exit of a Flat Wide Column 64

3.3. Distribution of Column Efficiency 65

3.3.1. At the Exit Cross Section for the Particle Packed Columns 65

3.3.2. At the Exit Cross Section for the Monolithic Columns 67

3.3.2.1. Radial Distribution of the Contributions to Band Broadening for the Silica-Based Semi-Preparative Monolithic Column 70

3.3.2.1.1. Distribution of the Eddy Diffusion Term across the Column Exit 71

3.3.2.1.2. Distribution of the Axial Molecular Diffusion Term across the Column Exit 73

3.3.2.1.3. Distribution of the Mass Transfer Resistance Term across the Column Exit 75

3.3.3. Efficiency Distribution at the Exit of the Flat wide Column 77

3.3.3.1. Further Evaluation of Performance of the Online Microelectrode Detector for the Flat Wide Column 78

3.4. Distribution of Analyte Concentration across the Column Exit for Semi-Preparative Monolithic Column……80

3.5. Surface Characterization of Some Novel Bonded Phase Packing Materials for HPLC Columns Using Magic Angle Spinning-Nuclear magnetic Resonance Spectroscopy……...82

3.5.1. Surface Characterization of the Cogent bidentate C_{18} on type-C silica……..84

3.5.2. Surface Characterization of the XTerra Packing Material……....89

3.5.3. Surface characterization of the XBridge Packing Material……...93

3.5.4. Hydrolytic Stability of Packing Materials in Aqueous Acidic Conditions……...93

Chapter 4……98

Summary and Conclusions……98

References……104

Vita……..112

LIST OF TABLES

Table 2.1. Summary of characteristics of packing materials for surface characterization using solid state NMR……...**34**
Table 3.1. Peak assignment and their percentage distribution for bare silica…...**85**
Table 3.2. Peak assignment and their percentage distribution for Cogent bidentate C_{18} on type-C silica……**88**
Table 3.3. Effect of hydrolysis on the percentage distribution of the different peaks in the NMR spectra of Cogent bidentate C_{18} ……..**97**

LIST OF FIGURES

Figure 1.1. Schematic diagram of an instrument for axial compression of materials for chromatographic beds 5
Figure 1.2. Diagram of a column being radially compressed 7
Figure 1.3. Setup used for slurry packing 7
Figure 1.4. Visual depiction of the main terms of the Van Deemter equation 13
Figure 1.5. SEM-image of the porous structure of a typical silica-based monolithic column (left) and enlarged view of the entrance to a throughpore (right) 16
Figure 1.6. Fused core particle (HALO) and a typical fully porous particle showing difference between diffusion paths of solute 18
Figure 1.7. Representative surface chemical structure of ordinary silica (a) and type C silica (b) 20
Figure 1.8. Silanization reaction used in making silicon hydride groups to give to type C silica material 20
Figure 1.9. Surface chemical structure of the Cogent bidentate C18 on type C silica 21
Figure 1.10. Representative surface chemical structure of the silica/organic hybrid materials XTerra (a), and XBridge (b) 22
Figure 1.11. Surface chemical structure of XTerra MS C_{18} (a) and XBridge Prep C_{18} (b) 24
Figure 1.12. Photographed band front of a dye zone at a fixed mobile phase velocity (a), and radial distribution of the mobile phase velocity derived from the position of the band front of the dye (b) 28
Figure 1.13. Schematic diagram of an optical fiber assembly for spectroscopic determination of column radial heterogeneity 29
Figure 2.1. Schematic diagram of the microelectrochemical working electrode 39
Figure 2.2. Optical image of the combination electrode surface platform (a), and cross section view of the reference electrode showing layers of Ag/AgCl deposition (b) 41
Figure 2.3. Column setup for measuring radial heterogeneity for both particle-packed and monolithic beds 43
Figure 2.4. Column cross section indicating sample positions where radial heterogeneity measurements were made for a 10 mm i.d. (a) and 4.6 mm i.d. (b) columns 44
Figure 2.5. 1D view of the top plate used for pressurizing the flat wide column 46
Figure 2.6. D view of the bottom plate used to contain the sorbent layer for the flat wide column 47
Figure 2.7. 3D cross-section view of the bottom plate showing the positioning of the electrochemical microsensors 52
Figure 3.1. Overlay of three chromatograms at center position of column cross section for the analytical monolith (a), HALO (b), and LUNA (c) Interval between each measurement is at least 36 hours 55

Figure 3.2. Chloride response using the combination electrode showing the useful lifetime (a) and its reproducibility (b).
Background electrolyte is a 0.05 M tris-H_2SO_4, pH 7.4 buffer 57
Figure 3.3. 3D spatial distribution of the relative differences between the local mobile phase velocity and the mobile phase velocity at the column center for the HALO.....60
Figure 3.4. 3D spatial distribution of the relative differences between the local mobile phase velocity and the mobile phase velocity at the column center for the LUNA.....60
Figure 3.5. 3D spatial distribution of the relative differences between the local mobile phase velocity and the mobile phase velocity at the column center of the SemiPrep monolithic column.....63
Figure 3.6. Distribution of retention time for p-Benzoquinone across the exit of the flat column bed.....65
Figure 3.7. 3D spatial distribution of reduced HETP for HALO 66
Figure 3.8. 3D spatial distribution of reduced HETP for LUNA.....66
Figure 3.9. 3D spatial distribution of HETP for the analytical monolithic column.....68
Figure 3.10. Spatial distribution of the column efficiency at the exit cross section for the SemiPrep monolithic column 68
Figure 3.11. Elution profiles of four peaks recorded at the column center and distances of 1, 2.5, and 4.5 mm from the center for the SemiPrep monolithic column.....69
Figure 3.12. Local column efficiency along two perpendicular axes at the column exit for the SemiPrep monolithic column 70
Figure 3.13. Overlay of HETP plots at the center and 1mm radius of the SemiPrep monolithic column.....72
Figure 3.14. Distribution of the values of the eddy diffusion term at the center and on three concentric circles for the SemiPrep monolithic column.....72
Figure 3.15. 3D spatial plot of the *A* values for all positions at the column exit for the SemiPrep monolithic column 73
Figure 3.16. 3D spatial plot of the *B* values for all positions at the column exit for the SemiPrep monolithic column 74
Figure 3.17. Plot of average molecular diffusion values with respect to column cross sectional radius for the SemiPrep monolithic column.....74
Figure 3.18. 3D spatial plot of the *C* values for all positions at the column exit for the SemiPrep monolithic column 76
Figure 3.19. Plot of average mass transfer resistance values with respect to column cross sectional radius for the SemiPrep monolithic column.....76
Figure 3.20. Average HETP plots simultaneously recorded by four microelectrochemical detectors at the exit of the flat wide column 77
Figure 3.21. Hydrodynamic voltammograms for epinephrine and norepinephrine with isocratic elution. A flow rate of 0.5mL/min was used to elute the compounds in the mobile phase composed of 5.0 g/L of NaCl, 3.0 g/L acetic acid and 0.25 g/L of ethylendiaminetetraacetic acid in 80% methanol and 20% water 79

Figure 3.22. Combined chromatograms for epinephrine and norepinephrine. Recorded at +750mV *vs* Ag/AgCl. A flow rate of 0.5mL/min was used to elute the compounds in the mobile phase composed of 5.0 g/L of NaCl, 3.0 g/L acetic acid and 0.25 g/L of ethylendiaminetetraacetic acid in 80% methanol and 20% water **79**
Figure 3.23. Radial distribution of local analyte concentration along two perpendicular axes at the exit cross section of the SemiPrep monolithic column **81**
Figure 3.24. Elution profiles of two peaks recorded at two opposite positions at distance of 1mm from the center of the SemiPrep monolithic column **83**
Figure 3.25. Representation of the maximum concentration and the peak area relative to the maximum concentration and peak area at the column center at different positions of the SemiPrep monolithic column **83**
Figure 3.26. ^{29}Si CP-MAS spectrum of bare silica **85**
Figure 3.27. ^{29}Si CP-MAS spectrum of Cogent bidentate C_{18} on type-C silica **87**
Figure 3.28. ^{29}Si CP-MAS spectrum of underivatized XTerra (a) and XTerra MS C_{18} (b) **90**
Figure 3.29. ^{13}C CP-MAS spectra and peak assignments for XTerra MS C_{18} **92**
Figure 3.30. ^{29}Si CP-MAS spectra for underivatized XBridge (a) and XBridge prep C_{18} **94**
Figure 3.31. ^{29}Si CP-MAS spectra for bulk Cogent bidentate C_{18} and sample treated for five days with acidic water at pH 3.0 ..... **96**

CHAPTER 1

INTRODUCTION AND BACKGROUND INFORMATION

1.1 Introduction to Column Heterogeneity

Liquid chromatography – especially high performance liquid chromatography (HPLC) remains one of the most widely used methods in separation sciences. With this method, analysts are provided with both qualitative and quantitative information on the composition on a wide variety of samples [1–5]. By some estimates, more than 75% of all separations made in environmental, pharmaceutical, and medical analysis are performed with HPLC [6].

The work horse of most HPLC setup is the chromatographic column bed where the actual chemical separation is effected. These beds are made to be porous because the percolation of the mobile phase through the stationary phase is a key feature of the process of chromatography. High column efficiency is often desired, and this depends on the condition of near equilibrium where the exchange of solute molecules between the stream of mobile phase and column bed must be fast and frequent. Other desirable properties of a chromatographic bed are that the surface area between the stationary phase and mobile phase must be large, while the hydraulic resistance between the bed and the stream of mobile phase should not be high.

Another very important aspect of all column beds is its degree of heterogeneity. By definition, heterogeneous is an adjective used to describe an

object or system consisting of multiple items having a significant number of structural variations. Conventional wisdom has it that the radial flow profile in chromatographic columns is flat, as it should be when there is piston flow [7]. As a result, most studies (theoretical or experimental) have assumed that columns are radially homogeneous. Therefore, chromatographic modeling assumes generally one spatial dimension only, the column length. This assumption has been falsified by Guiochon et al [8] in a work based on the results of earlier investigations pursued by Knox et al. [9], Eon [10], Baur et al. [11,12], Farkas et al. [13,14], Bayer et al. [15-17] and Fernandez et al. [18]. These studies have demonstrated that particle packed columns were not radially homogeneous but that the velocity of the mobile phase as well as the local column efficiency significantly vary across the diameter of these columns.

All columns exhibit some degree of radial heterogeneity across any column section [19-29]. While the degree of variations may be random in a small given region of a column, typically, a distinct trend can be observed between the core region of the column and its wall region. For silica-based monolithic columns, the mobile phase velocity is observed to be greater at the wall region than at the core region of the column cross section. For some modern packed columns, the mobile phase velocity is higher in the center than close to the wall, while for others, it is the reverse trend that is observed. This difference is due to the method used to pack the column and will be discussed in detail later. For column efficiency, all columns seem to show an improved efficiency in the core region than at the wall region.

In recent years, new packing materials have emerged and column technology has rapidly evolved, prompted by new requirements of analysts. Many modern applications of chromatography require faster and more efficient columns than those traditionally available. Three main lines of approach are currently pursued: the development of silica-based monolithic columns, the structure of which attracts much interest [30-33]; (2) the Fused-Core or porous shells particles having a solid core [34, 35]; (3) the very fine particles having a diameter between 1 and 3µm [36, 37]. These approaches each have their advantages and drawbacks. It is important, however, to better understand their properties to determine the degree to which these new columns are radially heterogeneous. This improved understanding would be required for any further progress in packing technology.

1.2. The Objectives of High Performance Liquid Chromatography

The purpose of high performance liquid chromatography (HPLC) is the separation of the components of a plug of a sample into string bands of its components during the migration of this plug along a porous bed that is percolated with a suitable solution. This separation requires the proper selection of the material making the porous bed and of the solution. Once the sample solution is in contact with a second stationary phase, the different solutes will interact with the solid phase to differing degrees due to differences in adsorption, ion-exchange, partitioning, or size. These differences allow the solutes varying transit times through a stationary

phase and thus a mixture of components can be separated from each other.

Today, stationary phases made of columns filled with a porous bed and plates covered with a thin porous layer have been the preferred tool to implement liquid chromatography [38-45]. Both approaches have been used successfully to achieve the analysis of most complex mixtures, sometimes using appropriate methods of two-dimensional chromatography [46, 47]. Today, however, the field is dominated by column-based separations. The main reasons for the preference of column over plate chromatography are (1) the fact that columns are eluted, a process easier than plate development; (2) the detection and quantitation of the bands of separated compounds exiting columns with the stream of mobile phase is much easier than that of bands spread on plates of porous materials that scatter light; and (3) column separations were easily instrumentalized while considerable difficulties are still encountered to do so for plate separations [48]. Therefore, any attempt to instrumentalize plate separations so as to make it operate in a manner similar to HPLC will be a noble objective.

1.3. Methods for Consolidating HPLC Columns

There are three common methods used for consolidating particles to form a chromatographic bed and these are: axial, radial and slurry packing [49]. The packing procedure chosen is usually based upon characteristics of the packing material as well as what the column being packed would be used for.

Sometimes, radial compression is used to prepare analytical columns (inner diameter ≤ 4.6mm), but the most commonly used packing technique for packing analytical columns is the method of slurry packing [50]. For larger inner diameter columns intended for preparative applications, axial compression [51-53] and radial compression [54-55] packing methods are used for the preparation.

Axial packing requires the use of a column that can be thought of as a huge syringe, the barrel of which contains the packing material, and the piston being moved by a hydraulic jack that can apply a mechanical stress up to 100kg/cm^2. The instrument schematic for axial packing is illustrated in Figure 1.1. A dilute slurry of the packing material is placed in the column barrel, and the barrel is closed with a frit and a bolted flange. The jack is then used to move the piston upward so as to compress the slurry. At the end of the column opposite the piston, excess liquid can exit through the frit. A consolidated bed is progressively built up as the liquid is forced out of the column [56].

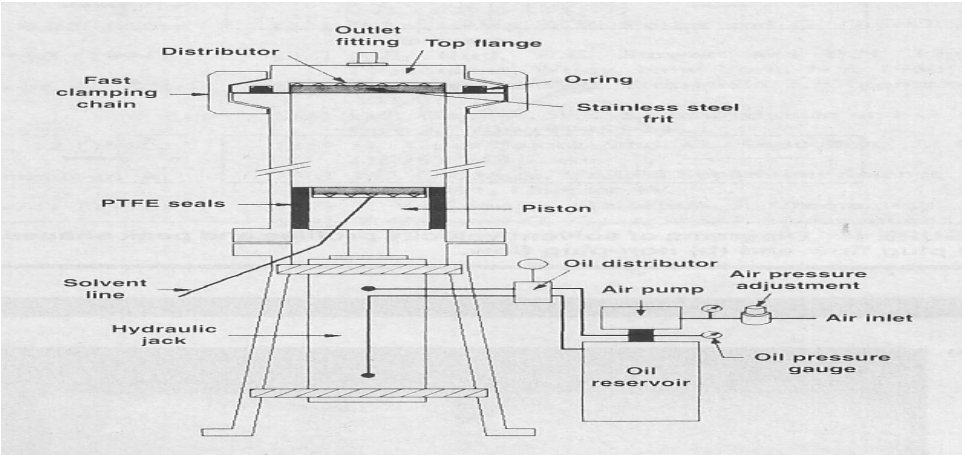

Figure 1.1. Schematic diagram of an instrument for axial compression of materials for chromatographic beds.

In radial packing, a plastic cartridge is filled with the packing material and placed inside a steel cylinder. This cartridge is closed at both ends by a frit and a stream distributor. The setup of the radial packing process in shown in Figure 1.2 and the design is such that both the plastic cartridge and steel cylinder are leak-proof sealed at both ends of the column. The bed is radially compressed by forcing a hydraulic fluid, under pressure, between the plastic cartridge and the steel cylinder [57]. The plastic cartridge takes on the shape of the bed when the column is under pressure from the hydraulic fluid.

In slurry packing, high pressure (up to 800 atmospheres) is used to push dilute slurry of stationary phase through a stainless steel column that is closed at the outlet with a frit and end fitting to prevent the stationary phase from being extruded from the column. The setup for a slurry packer is shown in Figure1.3.
To make suitable slurry, it is important to use a solvent that is effective at wetting and dispersing the packing material [50]. This is necessary to prevent aggregation of the stationary phase particles during the packing process and to prevent the particles from settling out of the slurry solvent prior to the packing process. High flow rate and pressure are used to push the solvent through the column and force the bed to consolidate.

Monolithic beds are consolidated in a manner quite differently from methods used for particulate materials. Monolithic columns are prepared by a sol-gel reaction in the presence of water-soluble polymer. This reaction produces a single monolithic structure consisting of a single porous rod; and this makes monolithic beds structurally different from beds made of distinct particles.

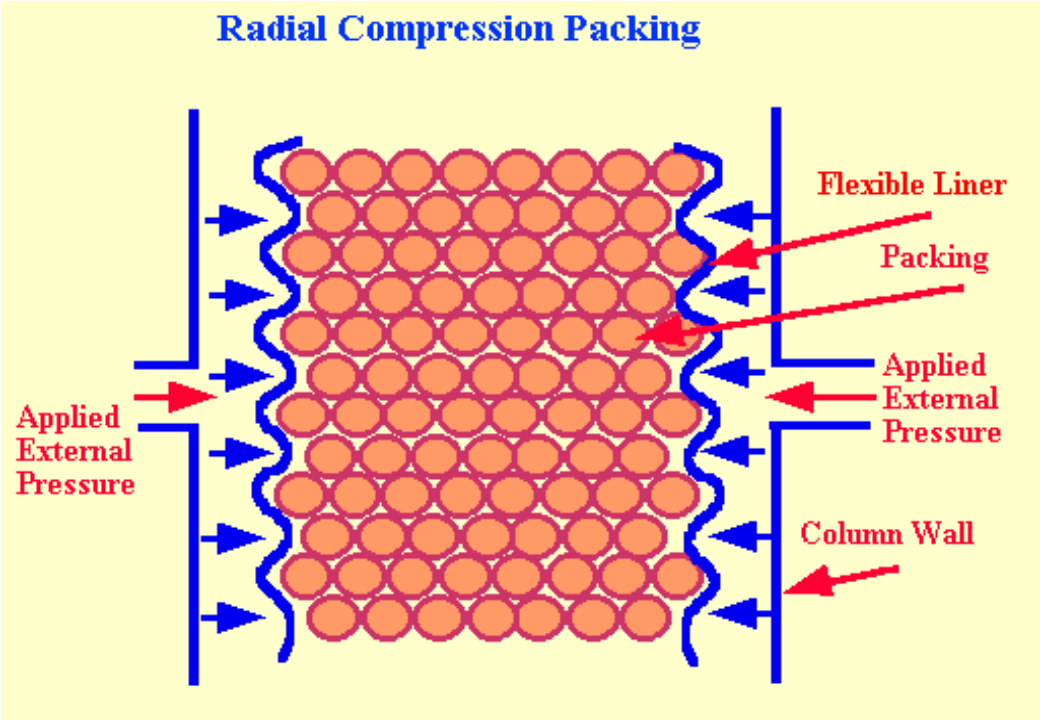

Figure 1.2. Diagram of a column being radially compressed.

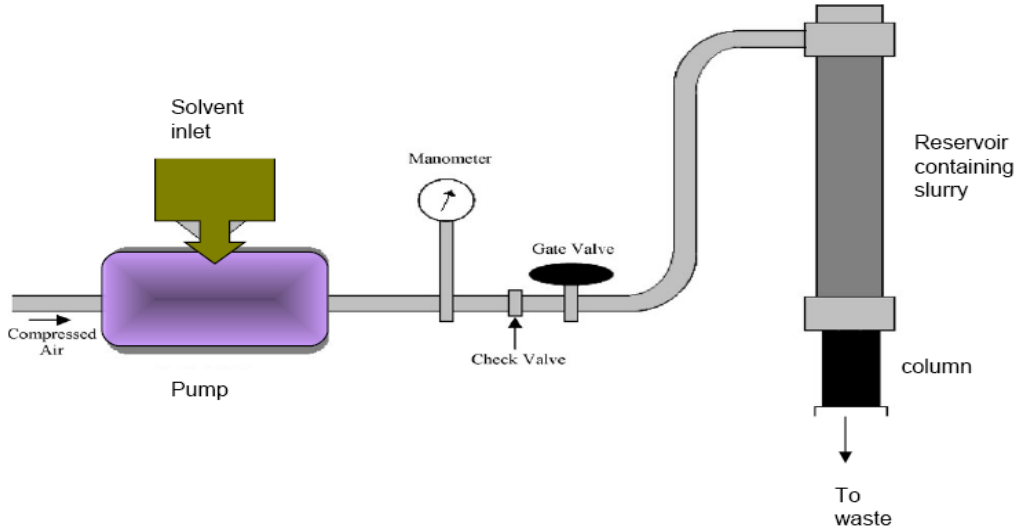

Figure 1.3. Setup used for slurry packing.

During the polymerization process for monolithic rods, shrinking occurs and the rod separates from the tube in which it is being prepared. The rod is then placed in heat-shrinkable polyether ether ketone (PEEK) tube and is radially compressed or encapsulated to give a chromatographic bed that can be percolated by the mobile phase [58, 59].

Each of the above mentioned bed consolidation techniques involve the application of a certain level of mechanical stress to the bed during the preparation process. However, this mechanical stress is not conveyed homogeneously throughout the bed during the preparation process; it varies depending upon the axial and radial position. This leads to heterogeneity within the beds of both analytical columns (typically having inner diameter up to 4.6mm) and preparative scale columns (typically having inner diameter of at least 10.0mm).

1.4. Descriptors of Column Performance

Once a column has been manufactured, it is necessary to evaluate its performance. There are several parameters that can be used to evaluate the performance of a given column. Some of these parameters are discussed below.

1.4.1. Column Permeability

The linear velocity, *u,* of a viscous fluid percolating through a packed bed under a pressure difference, *ΔP,* is given by Darcy's law [19]:

$$u = \frac{k_o d^2_p \Delta P}{\eta L} \qquad \text{(Eqn. 1.1)}$$

η is the viscosity of the fluid; *dp,* the average particle size of the packing material, L the column length and k_o the specific permeability of packed beds. Since pressure is uniformly transmitted through fluids, the same pressure drop drives the fluid along each stream-path through the packed bed. The corresponding linear velocity of the mobile phase is thus determined by the local value of the bed permeability.

1.4.2. Analysis Time

In chromatography, the retention times (the characteristic time it takes for a particular analyte to pass through the system from the column inlet to the detector under a specified set conditions) are all referred to the column hold-up time, t_0, defined as the elution time of an unretained tracer [60]. Hold-up time is related to the chromatographic velocity (u_0) and is defined as:

$$u_0 = L / t_0 \qquad \text{(Eqn. 1.2)}$$

L is the column length.

Another common parameter often used to reference analysis time is called the retention factor. The retention factor (k') is a measure of the time a sample component resides in the stationary phase relative to the time it resides in the mobile phase. It is an expression of how much longer a sample component is retarded by the stationary phase than it would take to travel through the column with the velocity of the mobile phase and is defined as:

$$k' = (t_R - t_0) / t_0 \qquad \text{(Eqn. 1.3)}$$

Where t_R is the retention time of the compound of interest. So, all retention times are proportional to t_0.

All these relationships apply to both monolithic and packed columns. For columns of a given length and at constant inlet pressure, analysis times are proportional to the mobile phase viscosity and to the column porosity. They are inversely proportional to the column permeability.

1.4.3. Column Efficiency

The efficiency of a chromatographic column is a measure of the capacity of the column to restrain peak dispersion, and thus provide high resolution. The higher the efficiency, the more the peak dispersion is restrained, and the better the column. The column efficiency is characterized by the Height Equivalent to Theoretical Plate (HETP or *H*), and is given by:

$$H = L/N \qquad \text{(Eqn. 1.4)}$$

with L being the column length and *N* the number of theoretical plates, given by

$$N = 5.54\,[(t_R - t_{R\,ex})^2 / (w^2_{1/2} - w^2_{1/2\,ex})] \qquad \text{(Eqn. 1.5)}$$

t_R is the retention time and $w_{1/2}$ is the peak width at half height. Both retention time and peak width should be corrected for the contributions of the extra column volumes ($t_{R\,ex}$ and $w_{1/2\,ex}$, respectively. These are the retention time and peak width at half height measured in the absence of the column. These values are

subtracted from those measures in the presence of the column so as to account for the column alone). *H* is a measure of the column efficiency per unit length, and small *H* values indicate a more efficient or better column.

The column efficiency depends on some of the physical characteristics of the column and on the velocity of the mobile phase. Actually, the efficiency of a column is generally derived from the profile of the analyte concentration of the bulk mobile phase at the column outlet. This profile depends on the relative width of the elution profiles recorded at the column exit and on their retention time distribution. Even if the average local efficiency along a stream-line were constant across the whole column diameter, the column efficiency measured after the conventional record of the elution band concentration would depend on the radial velocity distribution.

The reduced height equivalent to a theoretical plate (*h*), also referred to as the reduced plate height, is useful when describing column quality. It can be found using equation:

$$h = H/d_p \qquad \text{(Eqn. 1.6)}$$

dp is the average particle size of the packing material. The reduced plate height is a unitless number, and a smaller value indicates better column quality. Columns possessing high efficiency and giving narrower and well resolved peaks are often desired. In practice however, peaks are broadened. In 1956, van

Deemter proposed the first and simplest plate height equation accounting for band broadening [61, 62]. This equation is given by:

$$H = A + B/u + Cu \qquad \text{(Eqn 1.7)}$$

H is the height equivalent to a theoretical plate; *u* is the average velocity of the mobile phase. The numerical coefficients *A, B,* and *C* represent the different contributions to peak broadening and corresponds to the eddy diffusion contribution to band broadening, the axial molecular diffusion contribution, and the mass transfer resistance, respectively [63]. A visual depiction of the main terms of the van Deemter equation is shown in Figure 1.4. The origin of the Eddy diffusion (*A* term) is that as the mobile phase moves through the column, which is packed with stationary phase, the solute molecules will randomly take different paths through the stationary phase. Since different paths are of different lengths, solute molecules will arrive at the detector at different times, thus causing a broadening of the solute band. Molecular diffusion (*B* term) is simply the result of molecules diffusing from a region of higher concentration to one of lower concentration. Since the concentration of analyte is less at the edges of the band than at the center, the analyte diffuses out from the center to the edges. This leads to band broadening. The origin of the resistance to mass transfer (*C* term) is that every analyte molecule takes a certain amount of time to equilibrate between the stationary and mobile phase.

$$H = A + B/u + Cu$$

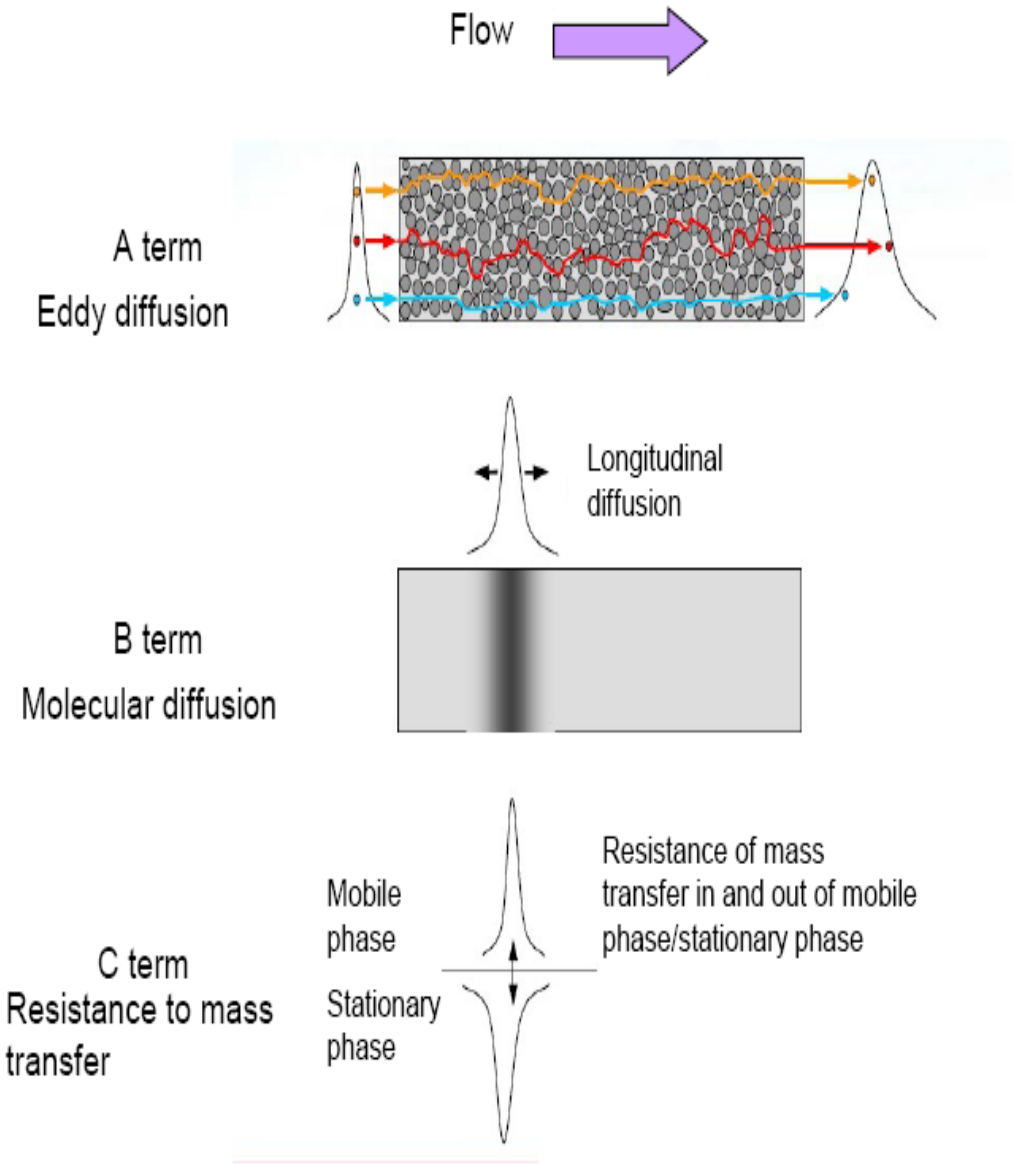

Figure 1.4. Visual depiction of the main terms of the Van Deemter equation.

If the velocity of the mobile phase is high, and the analyte has a strong affinity for the stationary phase, then the analyte in the mobile phase will move ahead of the analyte in the stationary phase. The band of analyte is broadened. The higher the velocity of mobile phase, the worse the broadening becomes.

Following early work by Huber [64], Knox [65] derived another HETP equation that has become most popular. This is given as:

$$H = \frac{B}{u} + Au^{1/3} + Cu \qquad \text{(Eqn. 1.8)}$$

The definitions of parameters are the same as for Eqn. 1.7. The *A* term has the dimensions of length (L) and time (T) by $L^{0.7}\ T^{0.3}$, the *B* term the dimensions of $L^2\ T^{-1}$, and the *C* term the dimensions of T. For columns that have been particularly well packed, $A \approx 1$, $B \approx 2$, and $C \approx 0.1$ [66].

Summarily, for columns of the same kind, the one that shows less variation in column efficiency in its cross section will have an overall better efficiency than one that shows more variations in the local efficiencies.

1.4.4. Bed Homogeneity

The radial homogeneity of a bed, whether it is of thermal or mechanical make up, is an important characteristic of all porous beds used in HPLC. The underlying reason why radial homogeneity is so important is because column efficiency is closely linked to it. For example, if a bed is not radially homogenous, then part of a band from a specific area of the column cross section may elute before the rest of the band at other areas. This will lead to band broadening and

hence poorer resolution [67, 68]. For this reason, bed homogeneity will remain an important factor to be considered during column manufacturing.

1.5. Recent Advances in Column Technology

Recent innovations in column technology are geared toward providing scientists the ability to extend the limits of HPLC technology for higher speed, higher column efficiency, more symmetrical peak shapes, and column stability in a wider pH range. Three main lines of approach are currently pursued: (1) the development of silica-based monolithic columns [30-33]; (2) the Fused-Core or porous shells particles having a solid core [34-35]; (3) the very fine particles having a diameter between 1 and 3µm [36-37]. These approaches each have their advantages and drawbacks, but in all cases, it is important to better understand their properties to determine to which degree these new columns are radially heterogeneous. This improved understanding would be required for any further progress in packing technology.

Consider the monolithic column. Its production and marketing came as a sudden advance in column technology, almost ten years ago. Monolithic columns consist of a continuous, porous rod that has a bimodal porosity and is tightly sealed against its tube [69]. These columns are made of a network of throughpores separated by a thin, porous silica skeleton. The average size of the throughpores measured using mercury intrusion porosimetry is estimated to be 1.7µm, and the average size of the mesopores measured by nitrogen adsorption is 14 nm [70]. The larger size pores let the mobile phase percolate along the column under a reasonable head pressure, at the velocities required for

satisfactory operation. The smaller size pores give to the column the large surface area that permits a sufficient retention of the analytes, good column efficiency, and a sufficient saturation capacity. A scanning electron microscope (SEM) photograph of a silica-based monolith is shown in Figure 1.5. The current high degree of interest for monolithic columns is justified due the very nature of the new monolithic beds that give these columns some significant advantages over the particle-packed columns. They have a larger volume of throughpores that are separated by a thin, porous skeleton of silica. These throughpores let the mobile phase percolate along the column under a relatively low head pressure, allowing the easy reach of the velocities required for satisfactory operation. The smaller size mesopores in the silica skeleton give to the column the large surface area that permits an adequate retention of analytes. A sufficiently high analyte saturation capacity is usually provided within the monolithic structure by the abundance of the small mesopores.

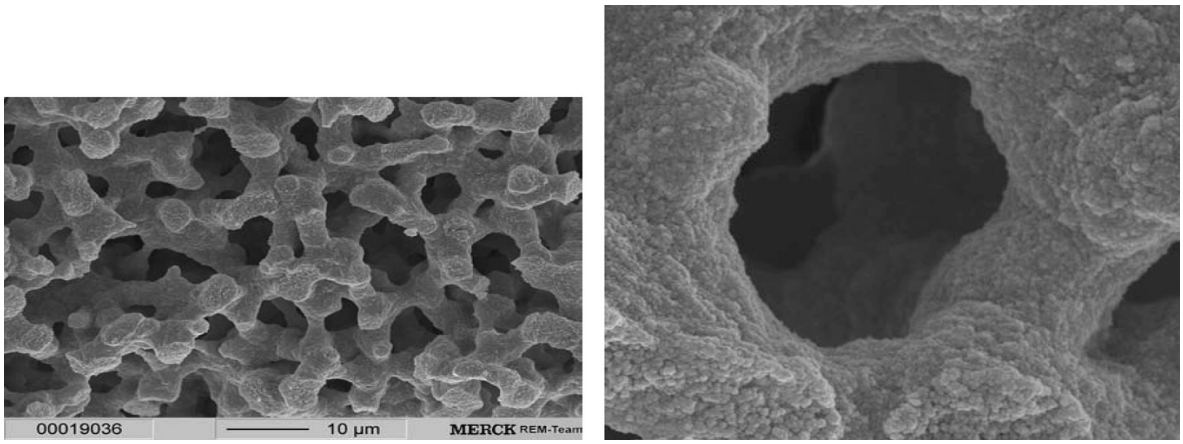

Figure 1.5. SEM-image of the porous structure of a typical silica-based monolithic column (left) and enlarged view of the entrance to a throughpore (right)

Compared to packed columns having throughpores of a similar size, monolithic columns show relatively high separation efficiency, especially at high mobile phase velocities, because of their enhanced radial mass transfer kinetics. These characteristics make monolithic columns very attractive for many high performance liquid chromatography applications.

1.5.1. Surface Properties of Some Recent Packing Materials

Much work is being invested in extending the analytical capability of reverse-phase high performance liquid chromatography (RPLC) and these efforts are concentrated on the preparation of fine particles of new silica-based, chemically bonded packing materials (CBPs). Alkyl bonded ligands like C_2, C_8, and C_{18} are the most widely used to prepare packing materials for RPLC, whereas specific applications may require CBP with polar functional groups (*e.g.*, -CN, $-NH_2$, $-NO_2$, -OH) or some other chiral moiety. Fully porous silica particles are commonly used in the preparation of CBPs. However, a recent advancement came in the form of particles manufactured to have a fused core surrounded by the thin porous shell. Figure 1.6 shows the difference between a typical fully porous particle and the fused core counterpart marketed as HALO.

The HALO is credited with generating hyper-fast separations and this comes from the unique Fused-Core particle technology that creates a 0.5μm porous shell fused to a solid core particle. This is because when the mobile phase flow rate is increased to speed-up a separation, the slow mass transfer of solute molecules inside the particles can limit resolving power. Fused-Core particle technology addresses this limitation.

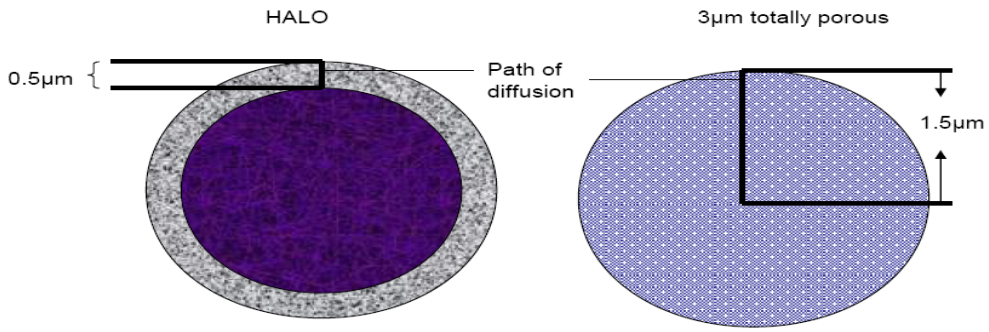

Figure 1.6. Fused core particle (HALO) and a typical fully porous particle showing difference between diffusion paths of solute.

These particles provide an incredibly small path (0.5µm) for diffusion of solutes into and out of the particles, thereby reducing the time solute molecules spend inside the particles and reducing a main barrier to fast chromatographic separations.

Other recent advances in column technology are geared toward improving the physico-chemical characteristics by replacing the surface silanol (Si-OH) groups of silica-based stationary phases with other more desirable chemical moieties so as to optimize separation processes based on RPLC. Typically, polar, acidic silanol functional groups are found on the surface of all silica-based stationary phases. Even after a surface has been derivatized, numerous residual silanols remain on the unbonded regions of the surface, in part because silica particles have a complex structure of many small pores and bulky reagents used for derivatizing the surface of these particles, such as octadecylsilane, have a limited ability to reach their surface, or in part because some silanol groups are hindered by previously bonded ligands or have a low reactivity. This is

undesirable if it contributes to unwanted interactions like the electrostatic attraction of analytes by these Si-OH groups. For example, ion-exchange interactions of basic compounds with acidic residual silanols can also cause tailing of their peaks and lesser resolution [71]. Overcoming such shortcomings was the rationale for the development of column packing material like the Cogent bidentate [72]. Unlike a typical silica material that has its surface densely populated by the Si-OH groups (type B silica), the Cogent packing material is populated with silicon-hydride groups (Si-H) and is refered to as a type C silica. This type C silica is the basis upon which the Cogent packing material is made and Figure 1.7 shows its representative surface chemical structure. The basic chemical reaction used in the fabrication process for silica hydride involves the utilization of a silanization reaction that produces a surface populated with silicon-hydride groups (Si-H) and is illustrated in Figure 1.8 [72].

The conversion of the Si-OH groups to make Si-H groups is not 100% efficient, thus some Si-OH groups (though very limited) will still be found on the type C silica. It is upon the type C silica that the commercial Cogent bidentate packing material is made. Figure 1.9 shows the surface chemical structure of the Cogent bidentate C_{18} material.

Another approach in the design of improved packing materials for HPLC columns was suggested a decade ago. The structure of the underlying matrix was redefined in a fundamental way by producing organic/inorganic hybrids, which combine positive attributes of both silica and polymers. These columns are now marketed under the commercial names of XTerra and XBridge.

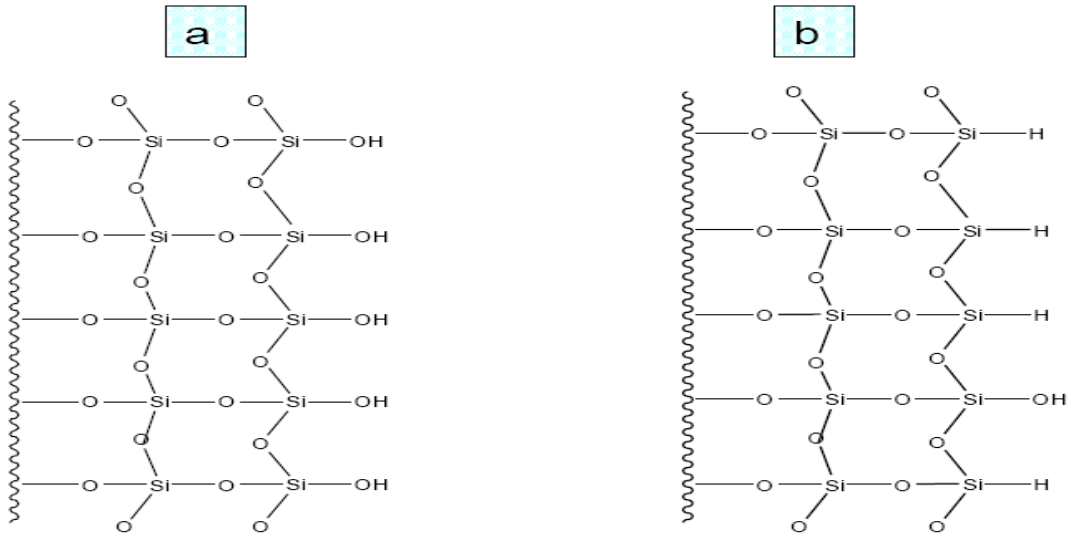

Figure 1.7. Representative surface chemical structure of ordinary silica (a) and type C silica (b).

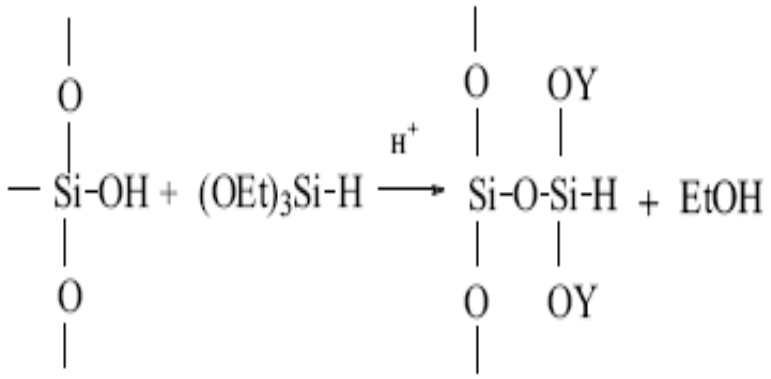

Y = Si or H depending on the extent of cross-linking.

Figure 1.8. Silanization reaction used in making silicon hydride groups to give to type C silica material.

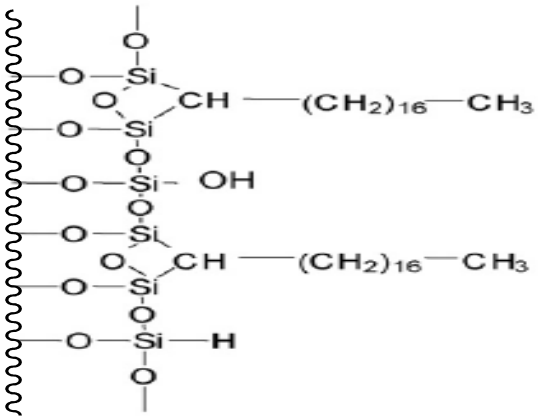

Figure 1.9. Surface chemical structure of the Cogent bidentate C18 on type C silica.

The surface chemical structures of the XTerra and XBridge materials are shown in Figure 1.10. In the patented manufacturing process of these columns or Hybrid Particle Technology, one out of every three silanol groups is replaced with an alkyl group, a methyl group for XTerra, an ethyl bridge for XBridge. Because the entire structure of the particle backbone has a distributive hydrophobicity, the result is a rugged hybrid (inorganic/organic) particle. The process for making these hybrid materials is illustrated in Eqn. 1.9 [73].

$$(RO)_4Si + n\,(RO)_3SiR^* + (1.5\,n + 2)\,H_2O = SiO_2(R^*SiO_{1.5})_n + (3\,n + 4)\,ROH \qquad \text{(Eqn. 1.9)}$$

R represents an alkyl group. Two high-purity monomers are mixed. During particle formation, inorganic units (SiO_2), and organosiloxane units ($RSiO_{1.5}$) combine. A carefully controlled polymerization process creates particles having the right organic/inorganic balance.

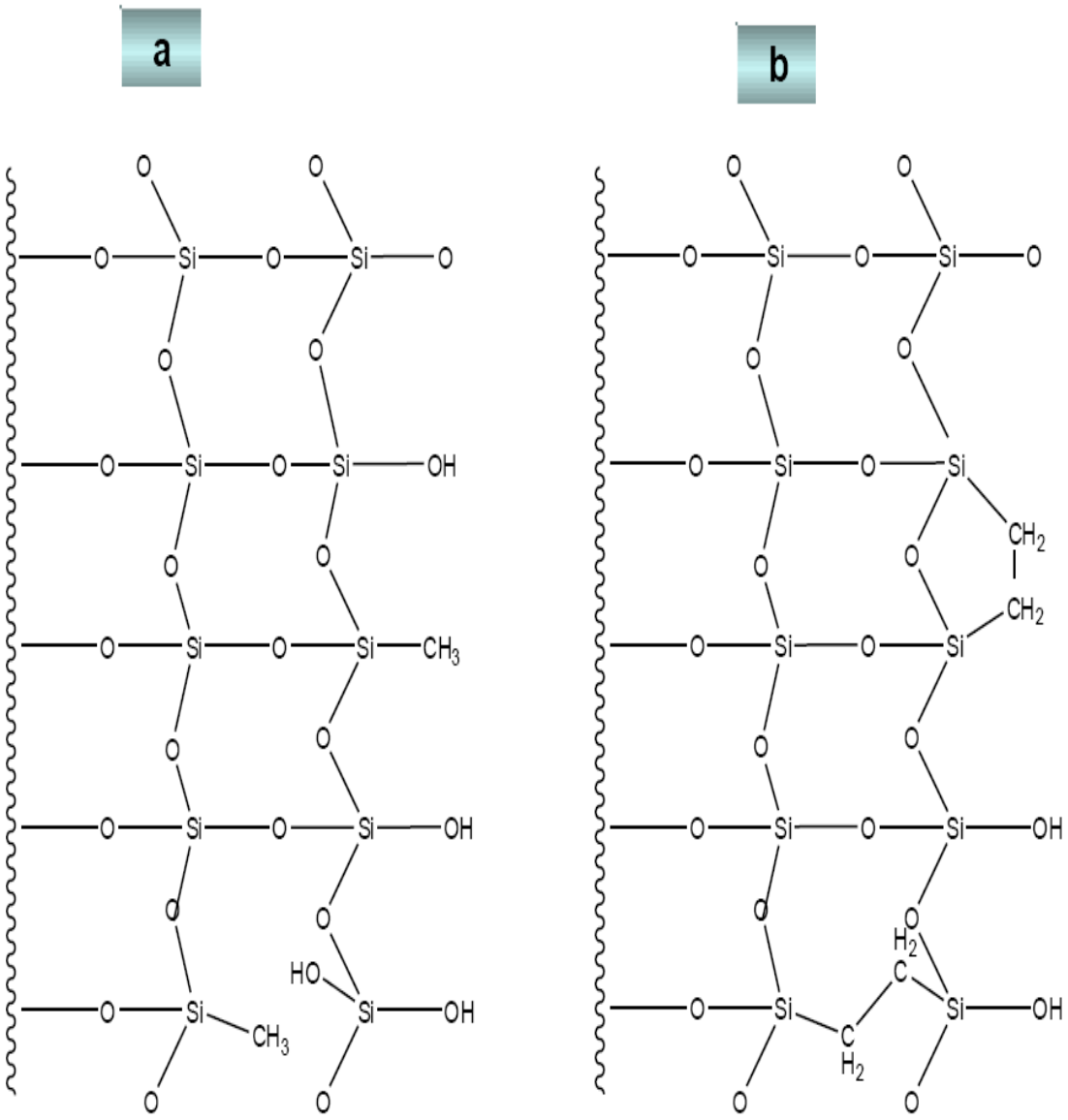

Figure 1.10. Representative surface chemical structure of the silica/organic hybrid materials XTerra (a), and XBridge (b).

These particles can then be surface-bonded and nonpolar groups (e.g., C_{18}, C_8) are attached. Examples of when C_{18} groups are attached for reverse phase liquid chromatography applications is shown in Figure 1.11, and these stationary phases are marketed as XTerra MS C_{18} and XBridge Prep C_{18}.

1.5.2. Characterization of the Surface Properties of Some Recent Packing Materials Using Solid State NMR

A powerful technique that provides chemical and structural information on solid samples and has been used to characterize chemically bonded stationary phases for chromatography is cross-polarization and magic-angle spinning (CPMAS) NMR [74-87]. In usual organic solids, strong dipole-dipole interactions are predominant. For an isolated spin pair the dipole-dipole interaction ***D*** depends on the magnetogyric ratios γ_I, and γ_s of the two spins I and S, the distance r between the nuclei, and the orientation of their binding vector relative to the external field and is expressed by the angle Θ in the relationship shown in Eqn. 1.10.

$$\boldsymbol{D} \alpha \gamma_I \gamma_s r^{-3} (1 - 3\cos^2\Theta) \qquad \text{(Eqn. 1.10)}$$

The interaction between the dipole can cause lines to broaden by up to several kHz. In the case of nuclei of low chemical abundance like ^{31}P or those with low natural abundance like ^{13}C and ^{29}Si in organic materials, the homonuclear dipole-dipole interactions are small as a result of the large distance between two spin pairs and so heteronuclear dipole-dipole interactions with protons are predominant.

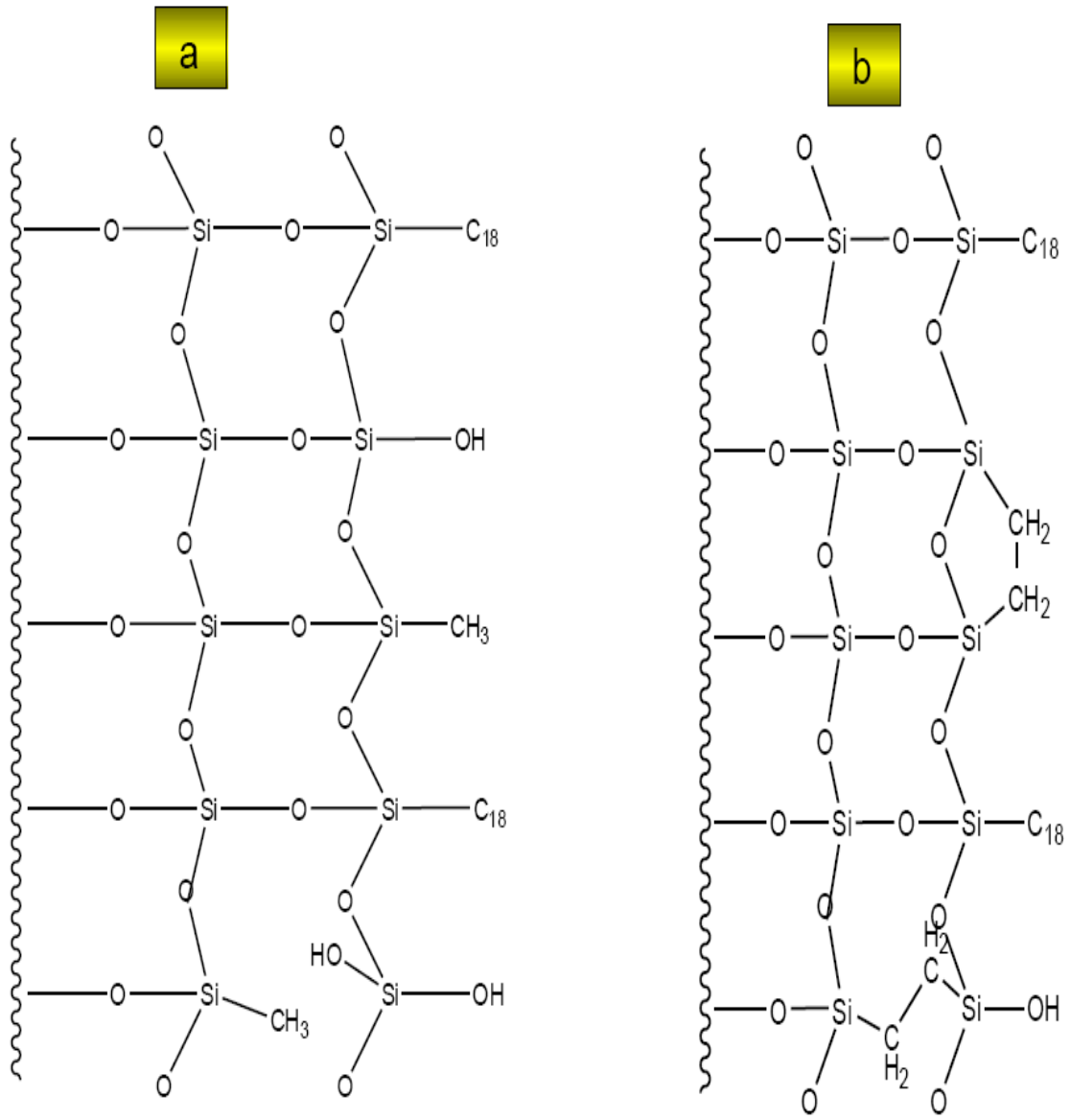

Figure 1.11. Surface chemical structure of XTerra MS C_{18} (a) and XBridge Prep C_{18} (b)

However, these heteronuclear interactions can be reduced by fast sample-spinning around the magic angle $\theta = 54.74^{o}$ (MAS).

In a CP-MAS NMR experiment the magnetization that is detected is generated by polarization transfer from a second nuclide (most commonly ^{1}H). The sensitivity enhancement of the "rare spin" (e.g. ^{29}Si) due to both the polarization transfer and the shorter proton relaxation times enables faster pulse repetition rates [88]. Thus, whenever it was necessary, CP-MAS was used to improve the sensitivity of NMR, to help determine structural connectivity, and to produce information on the silicon environments within the solid matrices of some novel materials used in HPLC [89].

1.6. Reasons for Radial Heterogeneity within Particle Packed Columns

The simplest explanation for the radial heterogeneity within particle-packed columns is the radial variation of the local packing density of their beds [69]. For columns packed by the slurry packing process, there is friction between particles and between the bed and the column wall. This friction leads to a radial variation of the packing density, which is higher close to the wall than in the column center. The net result is a cylindrical distribution of the packing density, resulting in fluctuations along the column of its local porosity, its permeability and its retention characteristics.

The physical implications of this result can be explained using Darcy's law [see Eqn 1.1]. Darcy's law shows that, under a given value of the inlet pressure applied, the regions of higher packing density (i.e., of lower permeability) will experience a slower flow than the regions of low packing density. If

chromatographic beds were ideally homogeneous, the radial distribution of the column permeability, hence that of the mobile phase velocity would be flat. If a radial distribution of the mobile phase velocity is observed, it suggests that there is a significant variation of the local bed permeability in the radial direction [20-29, 63, 90].

1.7. Reasons for Radial Heterogeneity within Monolithic Columns

Little information on the degree of radial heterogeneity of monolithic columns can be found in the literature. For the most part, their structure has been investigated with optical methods (notably using Scanning Electron Microscopy photographs of bed slices). These photographs provide good estimates of the average sizes of the through-pores and of the skeleton. Even though, such studies cannot provide any precise value of the size distribution of these pores because they do not have the spatial resolution needed to portray the radial heterogeneity of the network of through-pores across the column diameter [30, 63]. Yet, this information is needed to understand the behavior of monolithic columns.

There are several reasons for monolithic columns to be radially heterogeneous and thus to exhibit a radial distribution of mobile phase velocity and of local column efficiency. Some of these reasons are related to the method of preparation of these columns. Silica-based monoliths are prepared by a sol-gel reaction involving the hydrolysis of silanes. The polycondensation of silanes is an exothermal process and the heat generated is radially evacuated through the wall [69]. The result is that, the central region being warmer than the wall region,

the polycondensation reaction occurs faster in the warmer center of the column bed, which might lead to a denser network of through-pores in the center than in the wall region. Also, once a solid network is formed, further reactions tend to shrink the monolith [32, 33]. This causes a mechanical stress at the interface between the column wall and the monolith. If the stress is more than a certain threshold, the interface breaks and the monolith becomes separated from the wall. Since the deformation of the interface between the monolith and the wall under stress is probably not in an elastic fashion, its properties differ from those of the bulk core leading to radial heterogeneity.

No photograph among the many published has ever clearly suggested a significant degree of radial heterogeneity in the distribution of the local size or density of the throughpores [91]. Admittedly, small fluctuations of the local porosity cause large fluctuations of the local permeability. The physical implications can be explained using the Kozeny-Karman equation relating to monolithic columns, which states that the permeability, k_F, is given by:

$$k_F = \zeta^2 \varepsilon^3_e / 180(1-\varepsilon_e)^2 \qquad \text{(Eqn. 1.11)}$$

ε_e is the external porosity and ζ is a scaler parameter related to the average size of throughpores and their density. A small change by even 1% of ζ would not be seen on a SEM photograph but would cause a large enough radial variation of the axial velocity of the mobile phase velocity leading to a loss in column efficiency.

1.8. Methods for Investigating Column Heterogeneity

Some of the common methods used in measuring column structural heterogeneity are visual, spectroscopic, and electrochemical in nature. Each of these is described below.

1.8.1. Visual Method

This is a direct method in which a sample of a dye (e.g. Cibacron Blue) dissolved in the mobile phase is injected into the column at a particular flow rate [92]. Considerable time is allowed for the solute to migrate some fraction of the length of the column, and then the elution is interrupted by switching off the pump. The top flange of the column is removed and the packing pushed out and cut into sections along the axial direction. Cakes of wet packings are carefully handled and photographed. Qualitative determinations of the radial distribution of the mobile phase velocity are made, based on the scanning of the dye zone observed in the radial direction and is illustrated in Figure 1.12.

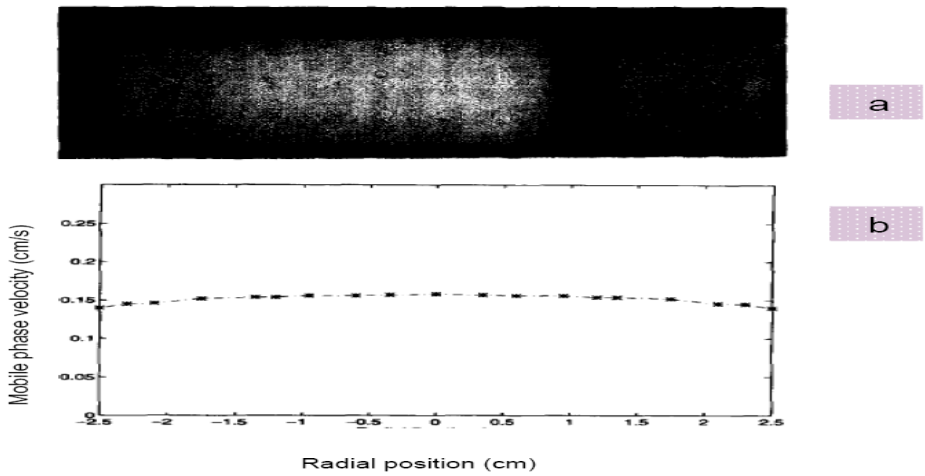

Figure 1.12. Photographed band front of a dye zone at a fixed mobile phase velocity (a), and radial distribution of the mobile phase velocity derived from the position of the band front of the dye.

A drawback of this method is the brittleness of the wet packing once it is removed from the column as it can easily disintegrate. Also, it is not very easy to make excellent quantitative determination of radial heterogeneity from the photographed dye zones.

1.8.2. Spectroscopic Method

In one aspect of this method, the radial distribution of analyte molecules within an elution band in HPLC is determined by local, on-column, fluorescence detection at the column outlet. Several optical fiber assemblies are implanted in the exit frit at different points over the column cross-section and the fluorescence of a laser-dye analyte is measured [14]. A beam of a laser (e.g. argon ion laser) is directed with optical fibers to locations of choice at the column outlet.

The design of such an optical fiber assembly is illustrated in Figure 1.13. The fluorescence signal induced by the excitation of the analyte molecules is collected by other optical fibers and carried to the appropriate pixels of a diode-array.

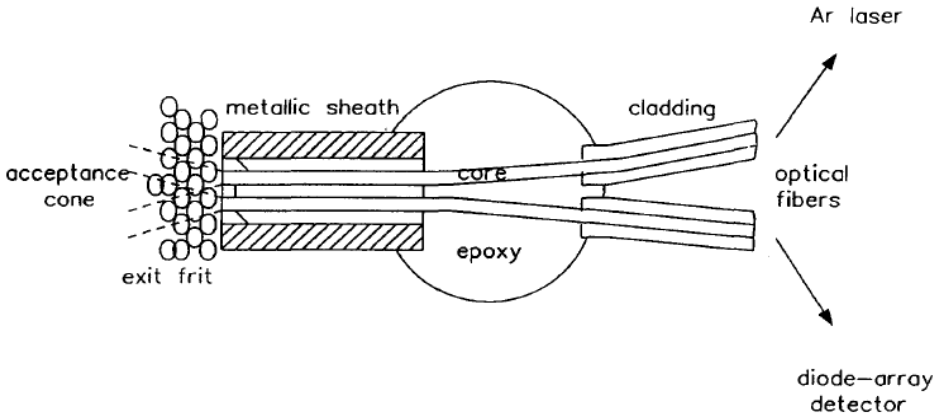

Figure 1.13. Schematic diagram of an optical fiber assembly for spectroscopic determination of column radial heterogeneity.

The individual elements of a diode array can be used as independent detectors. The distribution of the mobile phase velocity across the column can be measured as well as the column efficiencies obtained from the band profiles by the optical fibers.

1.8.3. Electrochemical Method

This was our method of choice in the acquisition of all data for column radial heterogeneity. In this method, an on-column electrochemical microdetector is used to determine accurately the radial distribution of the mobile phase velocity and of the column efficiency at the exit of HPLC columns. Such electrochemical detectors usually consist of a three electrode system namely; a working electrode (where the oxidation or reduction of a tracer component takes place), an auxiliary electrode (which is used to compare the current delivered by the working and the reference electrodes), and a reference electrode (which compensates for any change in the electrical conductivity of the mobile phase). A micro-sized working electrode is positioned at specific spots at the exit of a column to measure band profiles of solutes that show redox properties.

A common mode used in conjunction with HPLC is the amperometric mode. Amperometry is an electrochemical technique that enables the detection of electroactive species at the surface of a working electrode. When these molecules encounter the electrode surface, current flows as they are oxidized or reduced. The amount of current is proportional to the number of molecules oxidized per unit of time. The applied potential of the electrode is held fixed so that all of the molecules are oxidized. Prior knowledge as to what potential to use

is desirable and it depends on the analyte and the reference electrode being used. Also, the analyte must be electrochemically active.

1.9 Research Objectives

The goal of this work is to use an electrochemical microdetector to investigate the radial variation of the local velocity of the mobile phase and local efficiencies at the exit cross section of columns that incorporate recent advances made in column technology. Measurements were made for both particle packed columns (HALO, LUNA) and monolithic columns (analytical and semi-preparative).

Measurements were made of the van Deemter plots at different locations at the exit of the semi-preparative silica-based monolithic column. The results will then be fitted to the Knox equation, from which mapping of the radial distribution of the *A*, *B*, and *C* terms can be determined.

Also, the technology for microelectrochemical detector fabrication was further exploited to design and build an array of micro-electrode sensors and to assess its potential performance for online detection of eluent at the exit of a pressurized flat wide column. The arrangement of the electrodes also enabled a fast assessment of the lateral homogeneity of the bed.

Finally, the surface properties of some novel unconsolidated packing materials (Cogent bidentate C_{18} on type-C silica, XTerra, and XBridge) were characterized using solid state ^{29}Si, and ^{13}C NMR, and the results obtained were correlated to observed chromatographic behavior of these materials.

CHAPTER 2

EXPERIMENTAL

2.1 Materials and Chemicals

All water and methanol were of HPLC grade, and purchased from Fisher Scientific (Fair Lawn, NJ, USA). p-Benzoquinone and potassium chloride were reagent grade and purchased from Aldrich (Milwaukee, WI, USA). A 0.05 M solution of KCl in H_2O:CH_3OH; 80:20 was used as the mobile phase. The sample was a 0.2 mM solution of p-benzoquinone in the mobile phase. A small sample size of 10.0µL of the dilute solution was injected for each analysis. Benzoquinone exhibits stable and predictable redox properties. It is easily detected with the application of a potential of a –0.30 Volts vs. Ag/AgCl.

Two particle packed column were investigated for the radial heterogeneity and these were a 4.6 x 150mm HALO column, packed with 2.7µm C_{18}-bonded silica particles (Advanced Material Technology, Wilmington, DE); and a 4.6 x 150mm LUNA column, packed with 3µm C_{18}-bonded silica particles (Phenomenex, Torrance, CA, USA). The average pore sizes of the HALO and the LUNA particles are 90 and 100 Å, respectively [34]. Only one column in each brand was studied. This is because the columns are representative. Generally, when chromatographic columns are manufactured, they are tested to make sure the differences in the performance of each column do not exceed 1.5-2.0% before being marketed.

Two silica-based monolithic columns were used in this study (one for each kind). These are: a 4.6 x 100 mm C_{18} column (Merck, Darmstadt, Germany); and a 10×100 mm semi-preparative C_{18} column (Merck, Darmstadt, Germany). Both columns have a bimodal porous silica structure. The macropores are 2µm in average diameter; the mesopores are ca. 13 nm.

For experiments involving the use of the flat wide column, pure methanol was used as the mobile phase. Unless otherwise stated, the mobile phase flow rate was 0.50 mL/min. The sample was a 0.04M solution of *p*-benzoquinone in the mobile phase. The column was packed with silica gel (average particle size, 5 µm; surface area 500 m^2/g; pore volume 0.75 cm^3/g; average pore size 60 Å) purchased from Sigma (Sigma–Aldrich, St. Louis, MO, USA). Calcium sulfate hemihydrate from Sigma (Sigma–Aldrich, St. Louis, MO, USA) was added to consolidate the bed during operations.

For the solid state NMR experiments, the packing materials used for our studies were fine white powder generously contributed from two sources: J. Pesek (McroSolv Tech Corp., Eatontown, NJ, USA) donated bare silica (spherical shaped 5.2µm, 98Å, thermally treated sol-gel-type-B silica; washed with acid for low metal content of < 10ppm) and the packing material Cogent bidentate C_{18} on type-C silica. The hybrid packing materials (both underivatized and derivatized) XBrigde and XTerra were also generously contributed by U. Neue (Waters Corp., Milford, MA, USA). A summary of some key properties of the packing materials (with the exception of the bare silica material) used for the solid state NMR experiments is shown in Table 2.1.

Table 2.1. Summary of characteristics of packing materials for surface characterization using solid state NMR.

	Cogent bidentate C_{18}	**XTerra**	**XTerra MS C_{18}**	**XBridge**	**XBridge Prep. C_{18}**
Particle size (µm)	4	5	5	5	5
Pore size (Å)	100	120	120	135	135
Pore volume (mL/g)	0.92	0.64	0.64	0.70	0.70
Surface area (m^2/g)	350	176	176	185	185
Carbon load (%)	16.0	n/a	15.5	n/a	18.0
Ligand density ($\mu mol/m^2$)	n/a	n/a	2.40	n/a	3.10
Endcapped	No	n/a	Yes	n/a	Yes
Particle shape	Spherical	Spherical	Spherical	Spherical	Spherical

Prior to NMR measurements, sample sizes of 250-350mg were tightly packed into a cylinder and placed in a special double-bearing rotor of ZrO_2 so that the cylinder was oriented at 54.74° to the magnetic field of the NMR instrument and spun.

2.2. Instrumentation and Experimental Conditions

All liquid chromatography experimental data were obtained using an automated HP 1090 Series II liquid chromatograph (Agilent Technologies, Palo Alto, CA, USA). This instrument was equipped with a multi-solvent 88 delivery system, an autosampler with a 25µL sample loop, a diode-array UV detector, and a computer data station. The diode array UV detector was used as a bulk detector. The data station is equipped with the software needed to control the various functions of the instrument, to acquire the data, and to analyze them. An HP1050 microprocessor-controlled standalone pump unit with full programming capabilities (Agilent Technologies, Palo Alto, CA, USA) was used to deliver the mobile phase.

The UV detector was seldom used in our measurements because it records only the cross-section average composition of the eluent at the outlet of a column, and thus unable to monitor the elution profiles at well-defined, localized positions at the outlet of the column. Instead, we used a home-made micro-electrochemical detector. In all cases where the electrochemical detector was used, analyte signals were acquired using a CHI900B scanning

electrochemical potentiostat (CH Instruments, Austin, TX, USA) operated in the amperometric mode. The CHI900B provides the potential between the working electrode (WE) and the reference electrode (RE) and the detection of the current between the working electrode and the auxiliary electrode (AE). The CHI900B could examine chemistry at high resolution, near the interface and provides the powerful tool needed for this work. The CHI900B was also sometimes used in the cyclic voltammetric mode, to clean the electrodes and avoid excessive electrochemical fouling.

For the cross-polarization, magic-angle spinning (CP-MAS) NMR experiments, spectra were recorded with a solid state Varian INOVA 400 MHz wide-bore magnet spectrometer (Varian, Inc. Palo Alto, CA, USA) that is equipped with a chemagnetic 5mm MAS probe and spinning at 5kHz. The conditions used for acquiring the spectra were: a 2 ms contact time, a pulse width of 7μs, and a delay time of 3s. To acquire the ^{13}C CP-MAS spectra, 512 scans were used while for ^{29}Si CP-MAS spectra, 1024 scans were obtained. All spectral shifts were recorded relative to tetramethylsilane. For the ^{29}Si CP-MAS experiments, the Hartmann-Hahn match was set using an external standard hexamethylcyclotrisiloxane (^{29}Si CP-MAS NMR, δ -9.62), with a sample spinning rate of 5 kHz. On the other hand, adamantane (^{13}C CP-MAS NMR, δ 38.55), was used as the external standard for the chemical shift referencing for the ^{13}C CP-MAS experiments. A Gaussian apodization function was used to increase the signal to noise ratio for the spectra, which resulted in a band broadening of no more than 0.3 ppm. When necessary, the relative concentrations of the different

environments around silicon could be obtained using spectral deconvolution (using Mestrenova software) by comparing the relative intensities of the different silicon resonances.

2.3 Process for Local Detection

The UV detector, like all other conventional detectors used in chromatography, measures the cross-section average composition of the eluent at the column outlet. The determination of the consequences of a column radial heterogeneity requires the measurement of the radial distribution of the analyte concentration over the column cross-section. This requires the use of a local detection method capable of mapping this distribution. In this work, we used electrochemical detection in the amperometric mode. The detector consists of three electrodes, the working electrode, the auxiliary electrode, and the reference electrode. In the amperometric detection process, the mobile phase flows past the electrodes, the solute being continuously swept away as the peak elutes from the column. While there is solute present between the electrodes, a current will be maintained. The intensity of this current is a function of the local concentration of the chemical that it is set to monitor.

2.3.1. Fabrication and Description of the Microelectrochemical Detector Ensemble

In one approach for fabricating the microdetector, first, a 150μm i.d. capillary glass (World Precision Inc., Sarasota, FL, USA) was pulled using a laser pipette puller (model P-2000, Sutter Instrument, Novato, CA, USA). The parameters of the laser pipette puller were adjusted to produce glass tips that are

less than 0.5 cm long and about 0.5 mm O.D. The opening at this tapered glass end was then sealed by placing it in the flame of a bunsen burner for a few seconds. A complete sealing of this end was confirmed by observation under a light microscope. Next, a 1cm length of 25μm diameter platinum wire (Goodfellow Corp. Oakdale, PA, USA) was inserted from the open end of the pulled glass capillary so as to reach the sealed tip. The platinum wire was then fused with the glass by placing the tip in the middle of an 8.0V electrically heated coil of copper wire for about 5-8 min. Again, this fusing must be confirmed, and this was done using a light microscope. The next and most critical step was to establish an electrical connection between the platinum wire in the glass tip and another conducting wire (copper wire; Goodfellow Corp. Oakdale, PA, USA) that was eventually connected to the instrument (CHI900B Scanning Electrochemical Microscope; CH Instruments, Austin, Texas, USA) used for measuring currents. This electrical connection was achieved by inserting three or four 0.5 cm long pieces of lead down to the tip of the glass. After inserting the copper wire as well, a gentle and careful heating in the flame of a burner smolders the lead. This provides a suitable connection between the platinum and copper wires through the smoldered lead. Finally, the tip of the glass was gently polished so as to re-expose the platinum surface. The open end of the glass capillary was sealed with epoxy to complete the microdetector, which was used as the working electrode. A schematic diagram showing a completed working electrode is shown in Figure 2.1. Another approach used for fabricating the working electrode (less robust than the previous method but easier to fabricate) was also implemented.

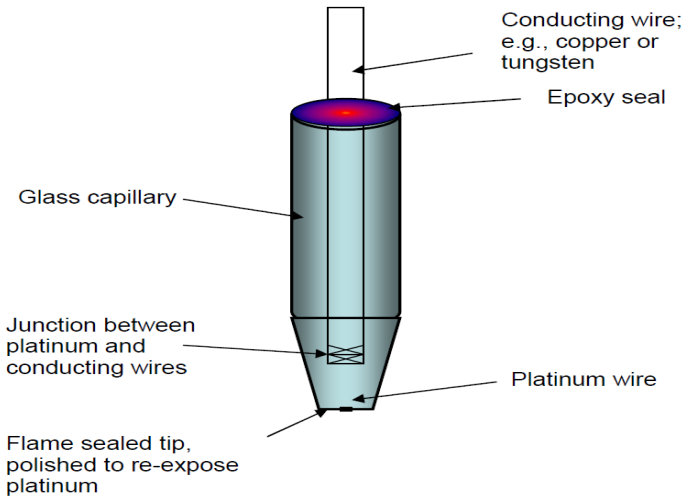

Figure 2.1. Schematic diagram of the microelectrochemical working electrode.

A 2cm piece of a 25μm-diameter platinum (Pt) wire was spun around one end of a tiny 10cm tungsten rod, leaving a 0.5mm Pt protrusion. Next, electrical conductivity was established between the rod and the Pt wire using silver (Ag) conducting epoxy. The Ag epoxy was then dried in an oven at 120^0 C for about 10 minutes. Under Observation of a light microscope, the Pt wire (attached to the tungsten) was then carefully inserted into the glass capillary to just about the opening of the tapered end. Using the flame of a bunsen burner, the tapered end opening was sealed and then gently polished to expose the Pt surface. The non-tapered end of the glass capillary was sealed with epoxy resin, so a protruding tungsten wire would serve as an electrical connector between the microsensor and data acquisition instrument. Unlike the previous method, the Pt wire is not electrically fused with the glass at the tip, thus the electrode was relatively less robust as the Pt wire could become disjointed from the glass with repeated use.

For both approaches, the working electrode was accompanied by a Pt wire auxiliary electrode and a commercial Ag/AgCl (sat. 3M KCl) reference electrode to complete the detector cell.

A third fabrication procedure that was used for the microelectrochemical detector is the construction of a combination electrode consisting of a dual working and reference electrodes on the same platform. To fabricate the combination electrode, two Pt wires (a 25 µm and a 75 µm diameter Pt wires) were each inserted into a separate barrel in a septum theta borosilicate glass capillary to prevent direct electrical contact between the WE and RE. For the construction of the reference electrode, a thin silver layer was deposited on the surface of a 75 µm diameter Pt wire using an electrodepostion bath composed of 30 g/L silver chloride, 500 g/L sodium thiosulfite, and 30 g/L potassium metabisulfite at a current density of 0.5 A/dm^2 for 3 min. The reagents for the Ag electroplating bath were purchased from Sigma–Aldrich (St. Louis, MO, USA). Following this, the electrode tip was immersed in a saturated ferric chloride solution for 10 min to form a Ag/AgCl layer, which will serve as the reference electrode. Figure 2.2 shows the optical image (acquired using a stereomaster zoom light microscope from Fisher Scientific, Fair Lawn, NJ, USA), of this combination electrode as well as the cross section view of the reference electrode showing layers of deposition. The potential applied between the working electrode and the reference electrode for the detection of the sample of p-benzoquinone was –0.30 Volts *vs* Ag/AgCl.

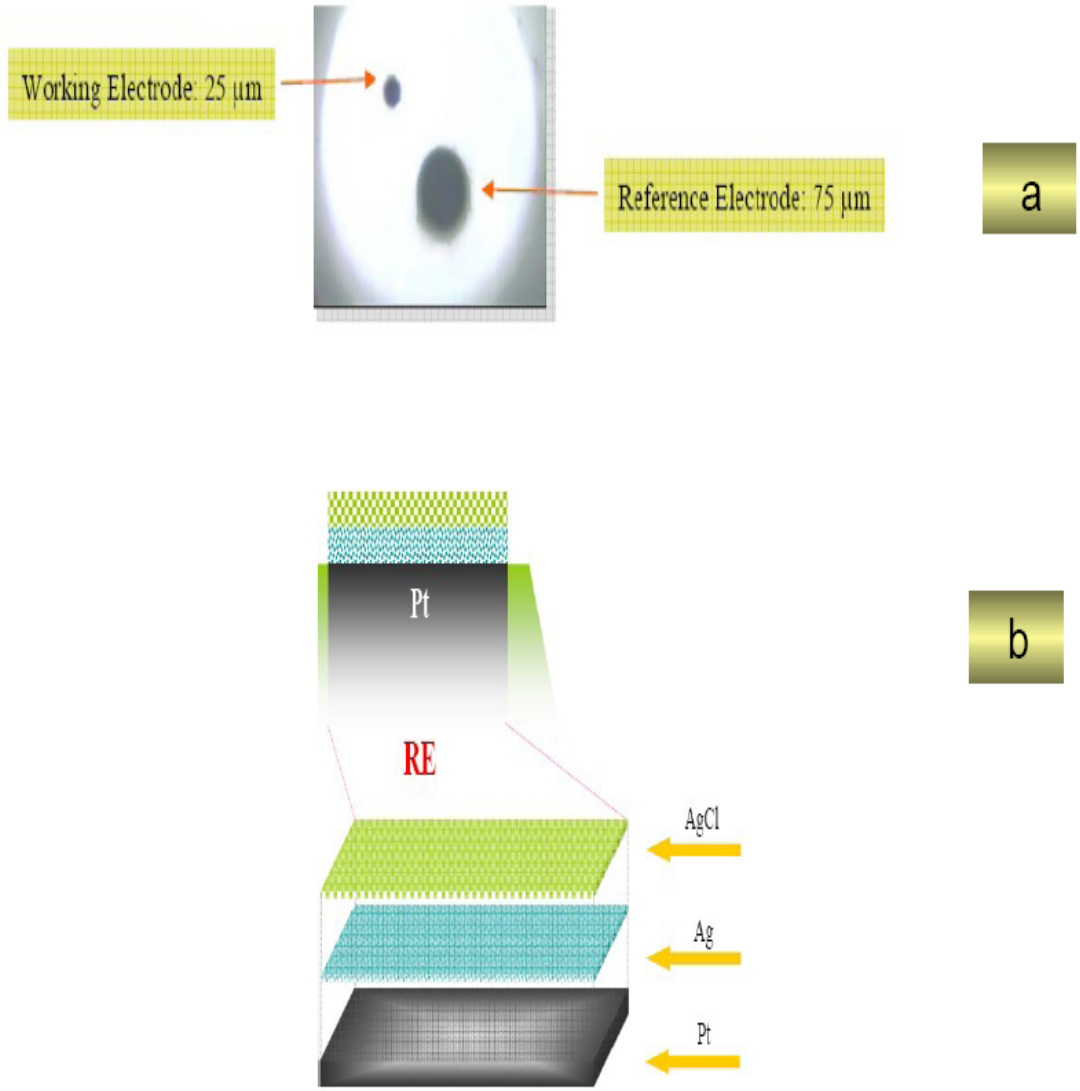

Figure 2.2. Optical image of the combination electrode surface platform (a), and cross section view of the reference electrode showing layers of Ag/AgCl deposition (b).

2.4. Column Setup for Measuring Radial Heterogeneity

2.4.1. Setup for Monolithic and Particle-Packed Columns

All particle-packed columns need a retaining frit pressed against the consolidated bed with a cap to hold the particles from flowing out of the column tube with the mobile phase. These caps have a tiny hole to insert a narrow tubing that carries the solute and mobile phase into and out of the column. Since measurements for radial heterogeneity were made at the exit of the column, it was necessary to modify the exit caps of these columns through machining to keep the frit in place and allow a sufficient space to place the microelectrochemical detector(s). To avoid electrical short-circuit of the electrodes, columns that had metallic frits were replaced with poly ether ether ketone (PEEK) frits of similar characteristics (Upchurch Scientific, Oak Harbor, WA, USA).

In contrast, the silica-based monolithic columns do not require a retaining frit because the monolithic rod is firmly fixed in the tube in which it is supplied by the manufacturer. Upon the removal of the end cap, the microdetector could be placed directly against the surface of the monolith.

The column setup showing the placement of electrodes is shown in Figure 2.3. The column cross section indicating sample positions were measurements were made for a 10mm i.d. and 4.6mm i.d. columns is shown in Figure 2.4.

Three distinct regions could be identified; regions at or close to the center of the column, regions between the center and wall, and those close to the column wall.

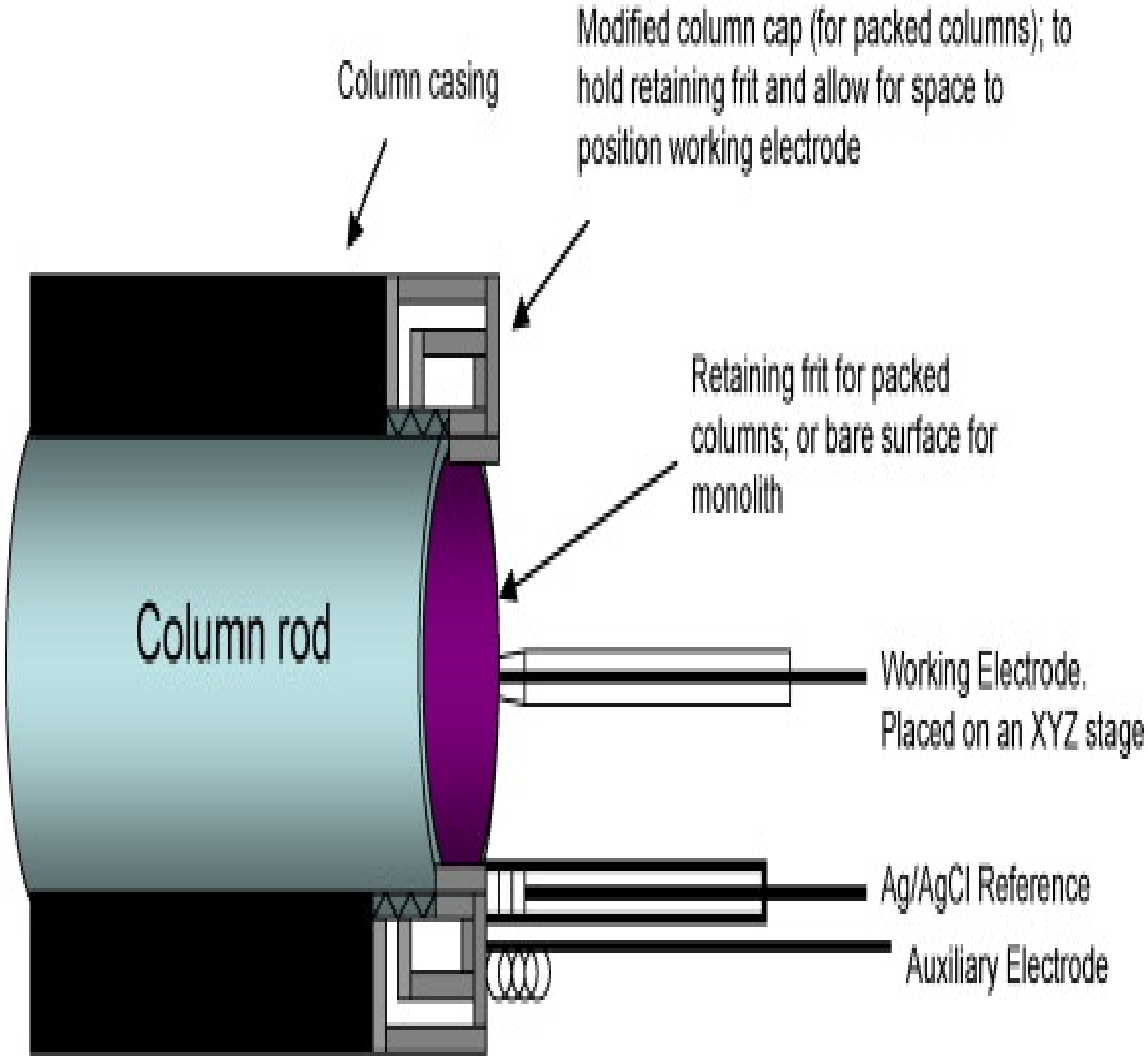

Figure 2.3. Column setup for measuring radial heterogeneity for both particle-packed and monolithic beds.

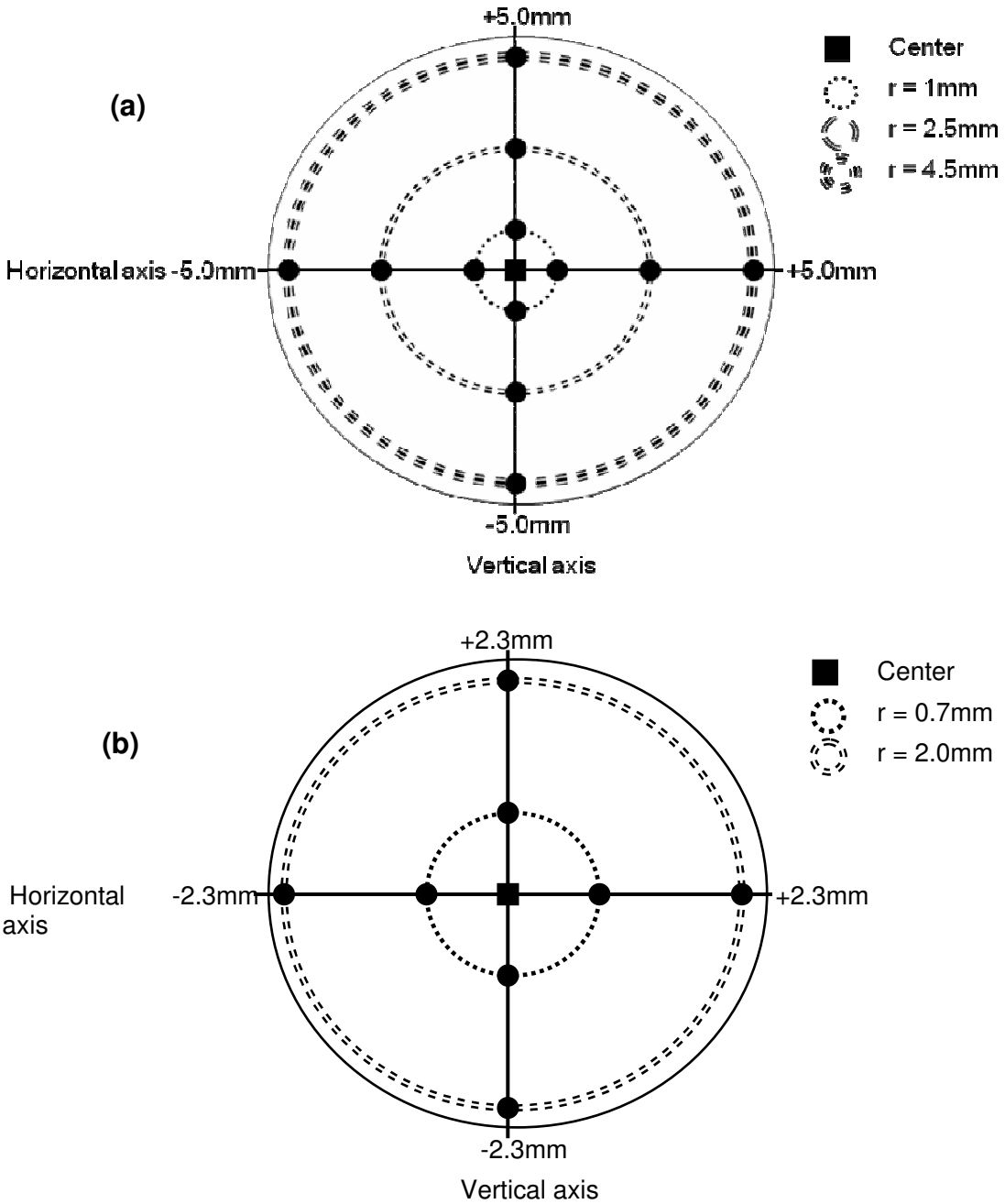

Figure 2.4. Column cross section indicating sample positions where radial heterogeneity measurements were made for a 10 mm i.d. (a) and 4.6 mm i.d. (b) columns.

By measuring the mobile phase velocities and column efficiencies at these regions, an excellent idea of how different regions contribute to column heterogeneity would be achieved. Overall, the primary interest was in investigating the possibility of a trend in heterogeneity existing between the column center and the wall regions.

2.4.2. Setup for Flat Wide Column

2.4.2.1. Instrumentation

The instrument for planar column was home-built and includes key features of HPLC such as a pressurized column, methods to access the bed (for sampling and detection), to pressurize the column, to control the mobile phase flow rate, and an online detector consisting of an array of electrochemical microsensors placed across the exit slit of the mobile phase stream. Analyte signals were acquired using a CHI900B scanning electrochemical microscope (CH Instruments, Austin, TX, USA) operated in the amperometric mode. An HP1050 microprocessor-controlled standalone pump unit with full programming capabilities (Agilent Technologies, Palo Alto, CA, USA) was used to deliver the mobile phase.

2.4.2.2. Column Housing

The housing for the flat wide column is made of two 15x15x2.5 cm blocs separated by a 0.24 mm Mylar sheet purchased from Fisher Scientific. A 1-dimensional (1-D) schematics of the top and bottom blocs are shown in Figures 2.5 and 2.6 respectively.

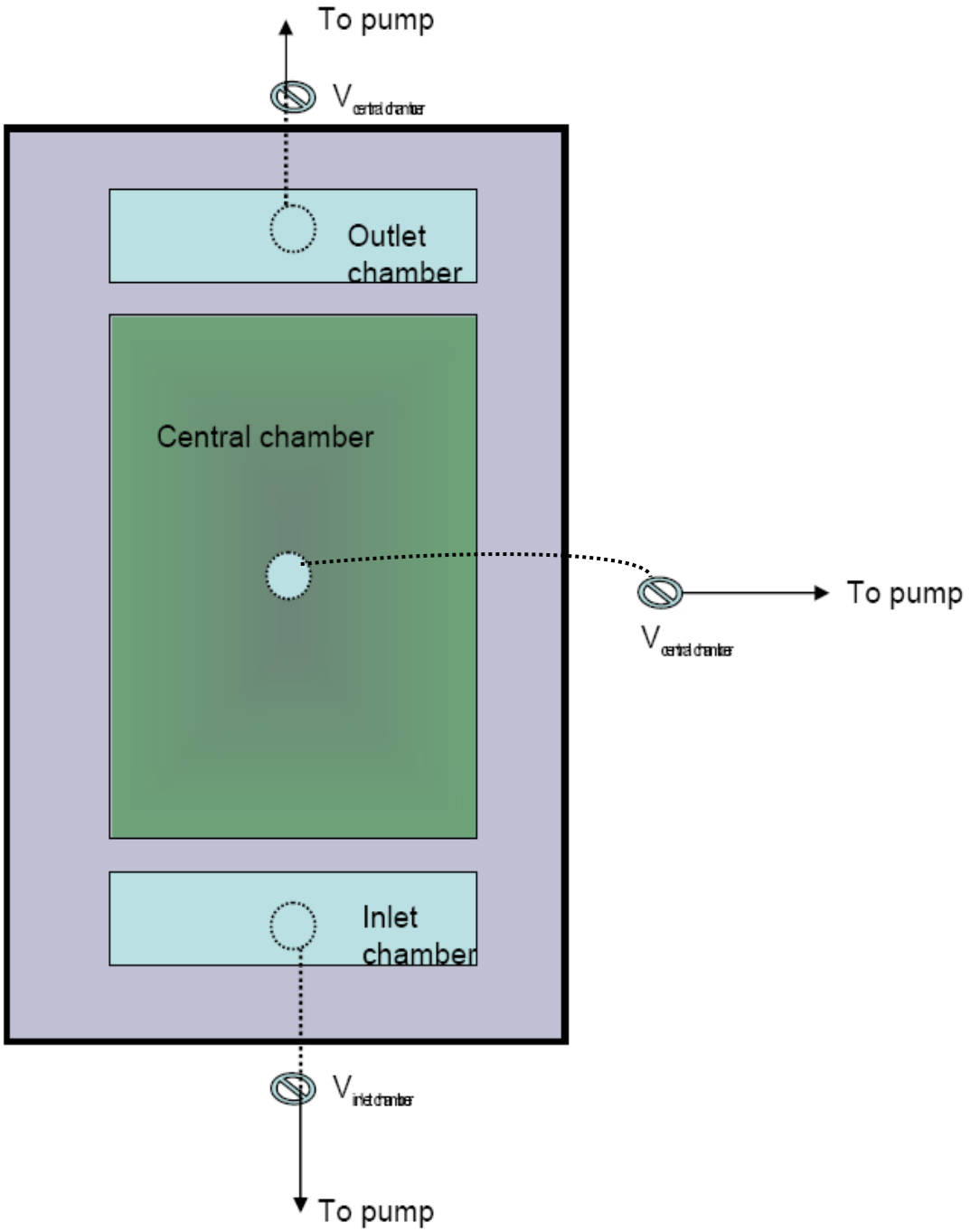

Figure 2.5. 1-D view of the top plate used for pressurizing the flat wide column.

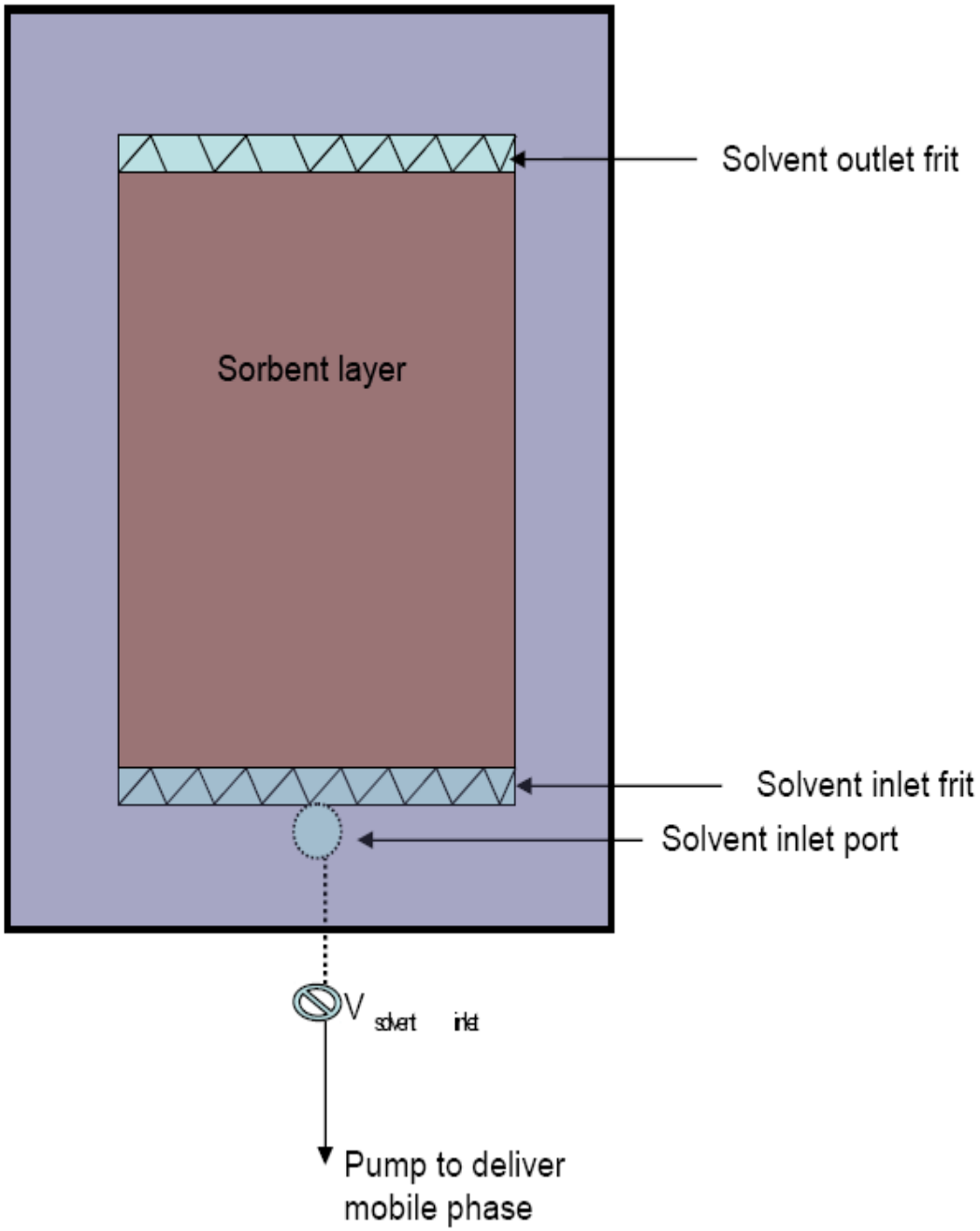

Figure 2.6. 1-D view of the bottom plate used to contain the sorbent layer for the flat wide column.

The system is designed to control the mobile phase stream through very thin and wide channels, for which there are no convenient valves. The top plate is made of plexiglass (Figure 2.5), the bottom one of stainless steel (Figure 2.6).

The top plate contains three chambers used for pressurizing the Mylar sheet against the lower plate. Primarily, the top plate contains three chambers used for pressurizing the bed. Applying pressure to the column bed by pumping water into the central cavity of the top bloc compresses strongly the Mylar sheet against the packing material contained in the central chamber of the lower bloc, prevents particles to drift downstream, and forces the mobile phase to percolate through the bed in the central cavity of the lower bloc, preventing it from passing the bed. Thus, by sealing the packing material inside its cavity, the central chamber maintains the pressure applied on the column bed during the experiment. The flow of mobile phase in and out of the flat wide column is controlled by applying pressure in the other two chambers (inlet and outlet chambers) of the top bloc, which function as valves. Applying pressure in these chambers compresses the Mylar sheet against the bottom plate, preventing the mobile phase from flowing through the bed. When the pressure is relieved, the Mylar sheet is pushed back into the compression chamber and the mobile phase flows freely. A Gilson pump model 302 (Fisher Scientific) was used to deliver the water needed to pressurize the

column bed and to switch the mobile phase stream on and off through the valves V_{inlet}, $V_{central}$, and V_{outlet}.

The mobile phase is delivered by an HP1050 microprocessor-controlled standalone pump, into the column through an inlet groove parallel to the column edge, through the valve $V_{solvent\ inlet}$ of the bottom plate. The packing material is contained in a 10x10x0.1 cm cavity, with two thin, long rectangular frits inserted in the steel block, at the opposite sides of this cavity, one at the inlet, the other at the outlet, to avoid that any particle of the bed move downstream. The mobile phase entering the inlet groove flows first through the inlet frit, which has a relatively low permeability (compared to those of the inlet valve and the column bed). This enables a constant pressure to be established along the groove, which ensures a uniform flow velocity across the bed and which eventually percolates through the exit frit.

2.4.2.3. Column Bed Preparation

The bed cavity is entirely filled with a thick slurry of the packing material, mechanically homogenized and composed of 15.0 g of silica gel with an average particle size of 5 µm, 2.0g of a gypsum binder (calcium sulfate hemihydrate), and 32.0 mL of water. A thick flat metal bar is slid over the bloc to eliminate the excess of slurry while making sure that the cavity is filled. After a few minutes the slurry solidifies, is left overnight to dry, and is dried for 30 min in an oven at 110 ^{o}C, to activate the silica.

2.4.2.4. Operation of the Instrument

After the bed has been prepared, the two plates are strongly applied against each other using a hydraulic jack that pushes the bottom plate against the top one, squeezing the Mylar sheet and the bed between these plates. The hydraulic cylinder helps to keep the bottom and the top plates pressed together such that their position would not be affected when pressure is applied in the compression chamber to press the Mylar sheet against the column bed in the bottom column housing. The compression pressure of the Mylar film against the bed can be of up to 50 bars, and this is desirable as it allows for the use of high inlet mobile phase pressure and the generation of a sufficiently high flow rate through the column bed. This combination permits the use of relatively small particle sizes to pack the bed; hence sufficiently high bed efficiency is achieved. The pressure applied to the bed by the Mylar sheet is perpendicular to the bed, so there is no side movement of the bed.

The instrument was operated in the on-line mode, with the array of micro-electrochemical sensors serving as detectors. Unless otherwise stated, the sample (10.0μL aliquot) dissolved in the mobile phase was injected through the inlet port into and through the sorbent layer. When pressure is released from the two side chambers of the top bloc, the inlet valve port opens, allowing the establishment of a stable pressure distribution across and along the column bed. At the exit of the bed, the

sample components pass through a microelectrochemical detector array, at which point they are detected.

2.5. Microelectrochemical Detector setup

The electrochemical detector responds to species that show redox property and the electrical output results from an electron flow caused by the chemical reaction that takes place at the surface of the electrodes. Our detector cell consists of three electrodes, the working electrode, an auxiliary electrode, and a reference electrode. Directly after the exit frit, a narrow slit perpendicular to the column bed was machined through the bottom plate, so that the mobile phase flows out of the instrument as a liquid curtain. Five special compartments were designed to accommodate the microelectrochemical detector. These electrodes were placed at equidistant 1, 3, 5, 7, and 9 cm from the side of the bed. A 3-D cross-section view of the bottom plate showing the placement of these microsensors is shown in Figure 2.7. The tip of the working electrode was inserted so as to be immediately after the exit slit while the other two electrodes were placed at 2.0cm downstream. While there is solute present between the electrodes, a current will be maintained. This arrangement ensures that the current generated by the redox reaction involving the analyte is immediately measured as the analyte exits the flat wide column. This also eliminates the band broadening due to post column contributions.

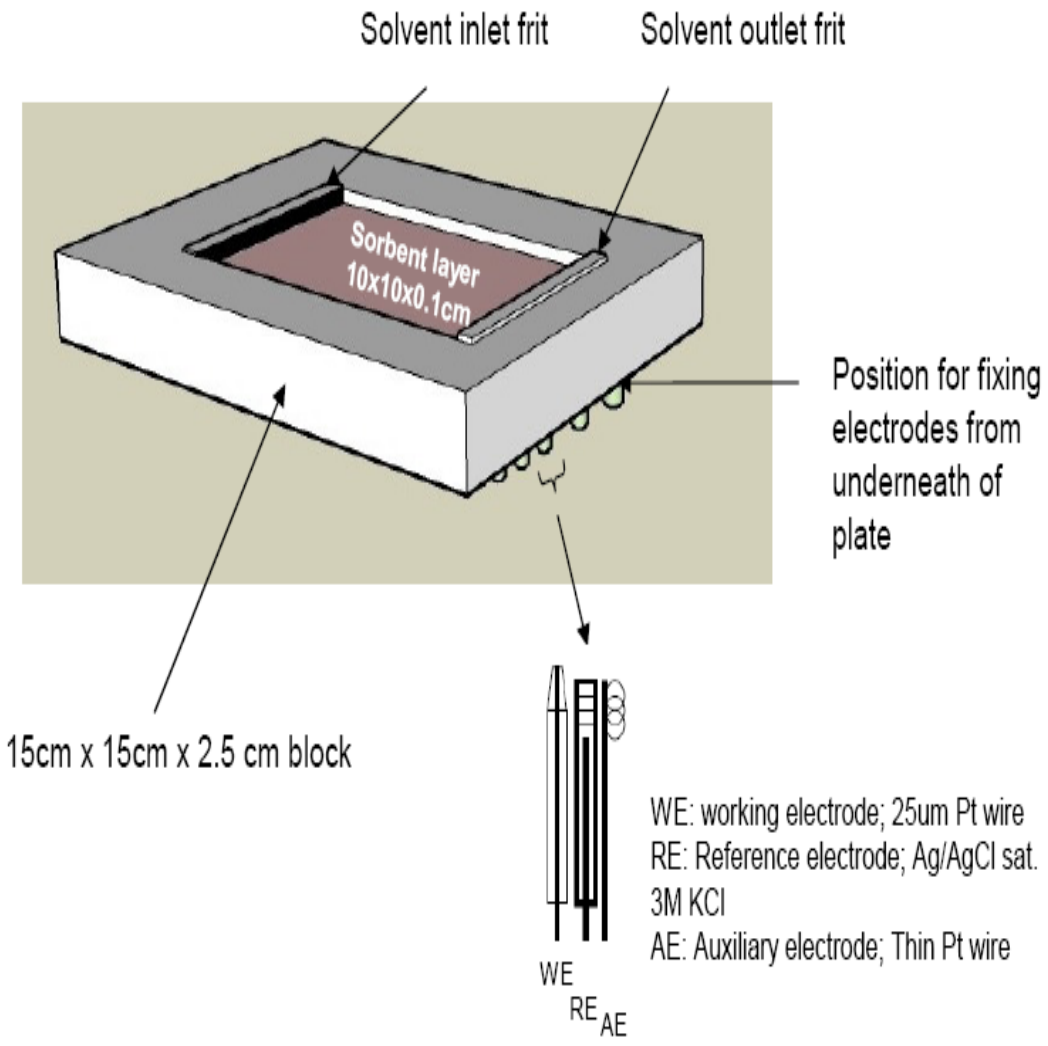

Figure 2.7. 3D cross-section view of the bottom plate showing the positioning of the electrochemical microsensors.

2.6. Calibration

Whenever it was necessary to measure column radial concentration distribution of analyte, a calibration of the detector signal was done using frontal analysis. At each location through the cross section of the column, the electrodes measured the concentration of the sample when the plateau concentration had been reached. This calibration process was used to determine the concentration at the selected locations. The other results were compared relative to the center of the column and calibration was not performed.

CHAPTER 3

RESULTS AND DISCUSSION

3.1 Figures of Merits of the Electrochemical Detector

As a test of the reproducibility of our results, three chromatograms were recorded at the center of each analytical column, at an interval of at least 36 hours between each successive measurement. Figures 3.1 show a very good reproducibility of the chromatograms for each three columns.

A possible problem with the medium- or long-term reproducibility of the signals of electrochemical detector is the fouling of their electrodes. This fouling reduces the active area on the surface of the working electrode. Care was taken to minimize this effect by periodically polishing the working electrode and rinsing it several times with deionized water. The detector sensitivity was satisfactory. The noise was low and an excellent signal-to noise ratio, in excess of 100, was obtained with the electrochemical microdetector. This allowed the very good level of precision and the reproducibility reported. Also, because the working electrode was fastened to a XYZ stage, the relative position of its tip is known within ±5μm in each direction.

For the work involving the flat wide column, a homemade combination electrode was fabricated and tested out in an effort to miniaturize the detector cell as it may become even more necessary in future instrument designs. A combination electrode is one in which the working and reference electrodes are constructed to be on the same sensor platform.

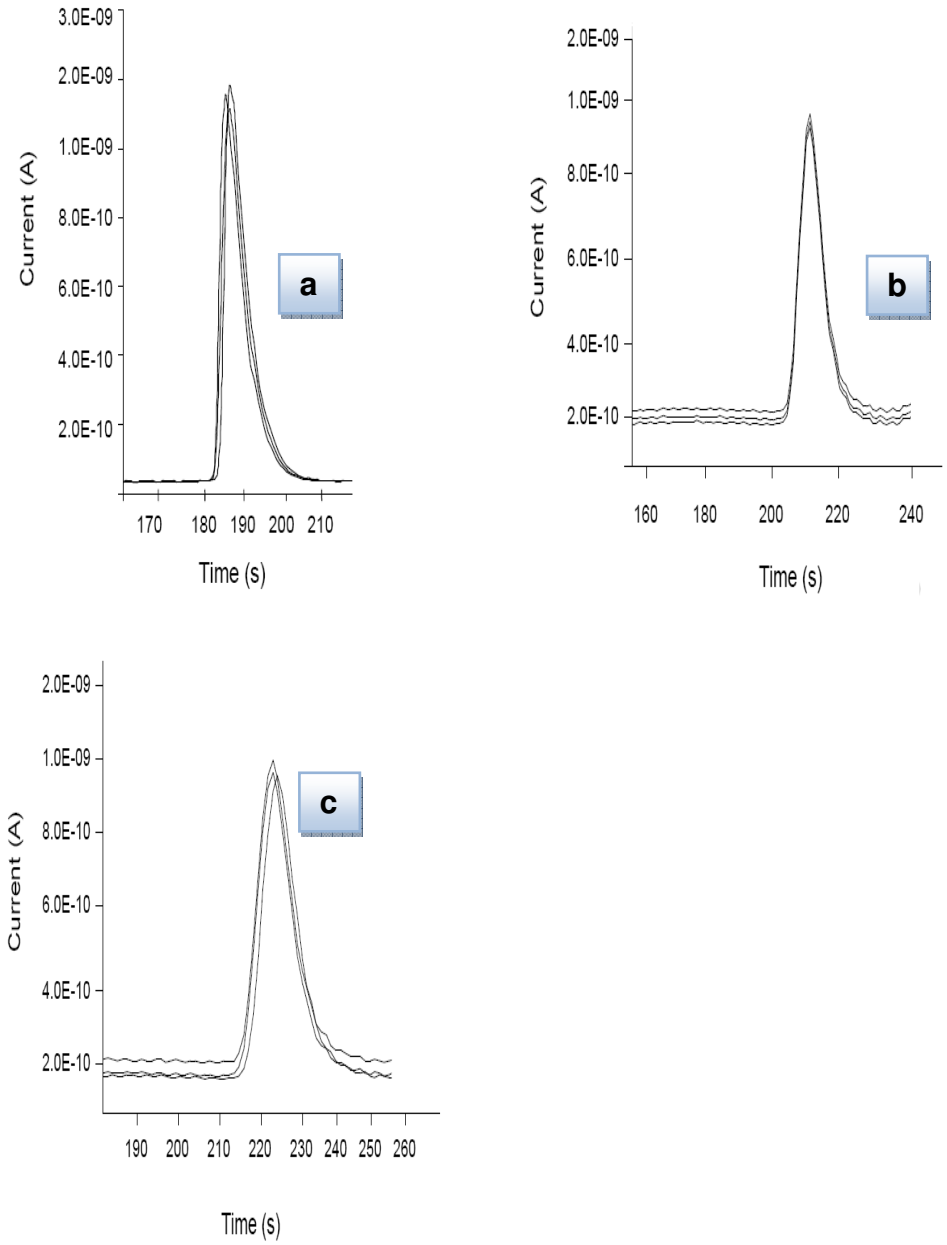

Figure 3.1. Overlay of three chromatograms at center position of column cross section for the analytical monolith (a), HALO (b), and LUNA (c). Interval between each measurement is at least 36 hours.

The surface diameter of our fabricated combination electrode at the point of completion ranged from 300-500 µm depending on the extent of polishing of the glass around the active electrode surfaces, whereas the diameter for the commercial reference electrode alone is 4.5 mm. However, a drawback for the combination electrode was its short life time. The useful lifetime of the combination Ag/AgCl electrode is shown in Figure 3.2 and was found to be 3 days.

For the work involving the flat wide column, a homemade combination electrode was fabricated and tested out in an effort to miniaturize the detector cell as it may become even more necessary in future instrument designs. A combination electrode is one in which the working and reference electrodes are constructed to be on the same sensor platform. The surface diameter of our fabricated combination electrodes at the point of completion ranged from 300-500 µm, whereas the diameter for the commercial reference electrode alone is 4.5 mm. However, a drawback for the combination electrode was its short life time. The useful lifetime of the combination Ag/AgCl electrode is shown in Figure 3.2 and was found to be 3 days. During its useful lifetime, the homemade combination electrode exhibited a highly linear response (r^2 = 0.996) over a Cl^- concentration from 1.0 x 10^{-4} to 1.0 x 10^{-1} M with a slope of 55.2 mV/pCl^- in a background electrolyte of 0.05 M tris-H_2SO_4, pH 7.4 buffer (see Figure 3.2a). As shown in Figure 3.2b, the combination reference electrode also showed high reproducibility and responses that are equivalent to a commercial Ag/AgCl sat. 3M KCl reference electrode.

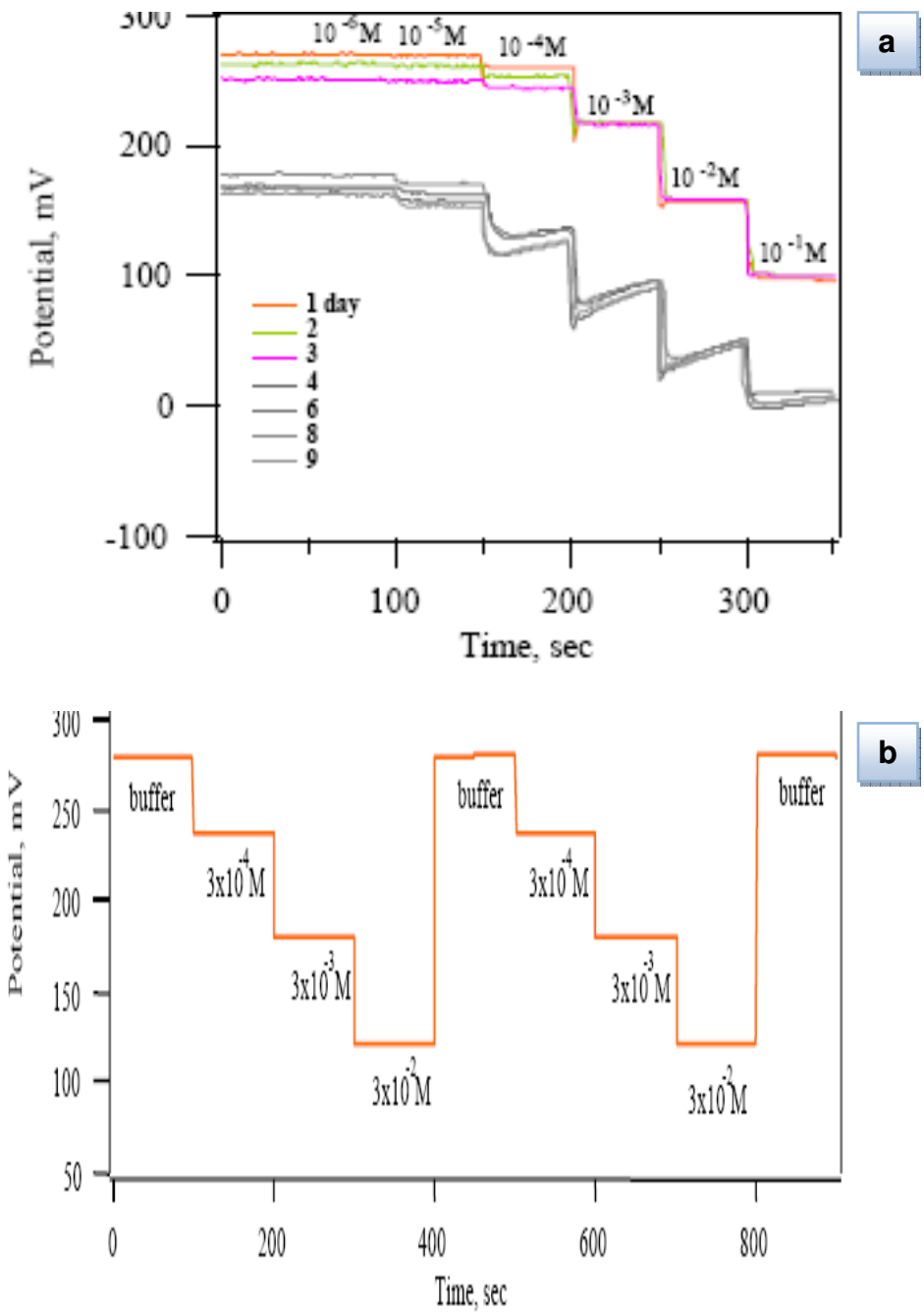

Figure 3.2. Chloride response using the combination electrode showing the useful lifetime (a) and its reproducibility (b).
Background electrolyte is a 0.05 M tris-H_2SO_4, pH 7.4 buffer.

The homemade combination electrode can be easily renewed by gently polishing the surface on a filter paper impregnated with methanol, then re-depositing the Ag/AgCl layer. However, since the commercial Ag/AgCl sat. 3M KCl reference electrode exhibits long term stability, it was the obvious choice for all data acquisition.

3.2. Distributions of the Mobile Phase Velocities

3.2.1. At the Exit Cross Section of the Particle-Packed Columns

Two particle-packed columns were investigated as to their radial distribution of mobile phase velocities at their exit cross section. These columns were a 4.6 x 150mm HALO C_{18} column, packed with 2.7µm C_{18}-bonded silica particles, and a 4.6 x 150mm LUNA C_{18} column, packed with 3µm C18-bonded silica particles. The average pore sizes of the C_{18}-HALO and the LUNA were 90 and 100 Å, respectively.

To determine the radial distribution of the mobile phase velocities, a 10.0µL sample of p-benzoquinone was injected at a flow rate of 1.0mL/min, and the peaks resulting from these injections were recorded at different locations at the outlet of the columns using an electrochemical detector. Six measurements were obtained at each location (RSD did not exceed 0.7%). The retention times measured at these respective positions were used to calculate a length-average velocity of the mobile phase, and to generate a map of this velocity distribution. At a location x, the length-averaged mobile phase velocity u_x, is calculated using the equation:

$u_x = L/t_x$ (*Eq. 3.1*)

L is the column length and t_X the retention time at the location x. Since we are interested in trends in the structural properties of the tested columns, all velocities will be normalized relative to that measured at the column center. Therefore, the relative velocity differences between any given spot where the velocity was measured and the center will be reported. This relative percent difference is calculated as:

Relative velocity difference = $[u_X - u_0] / u_0 \times 100\%$ (*Eq. 3.2*)

u_0 is the velocity at the column center.

A 3D plot of the local distribution of these relative differences in the mobile phase velocities for each of the two particle packed columns is shown in Figures 3.3 and 3.5. It both cases, the velocity distribution are not smooth nor flat, indicating some heterogeneity of the column permeability, hence, porosity. The flow rate distribution at the outlet of these particle-packed columns indicates that the linear velocity is maximal in the regions close to the column centers and becomes smaller when the point of detection moves from the column center to its wall region (see Figures 3.3 and 3.4). The relative velocity difference for both particle-packed columns are moderate- that for the HALO column does not exceed 3%, that for the LUNA column is less than 5.0%. This observation can be explained by a radial variation of the local packing density of the beds of these columns.

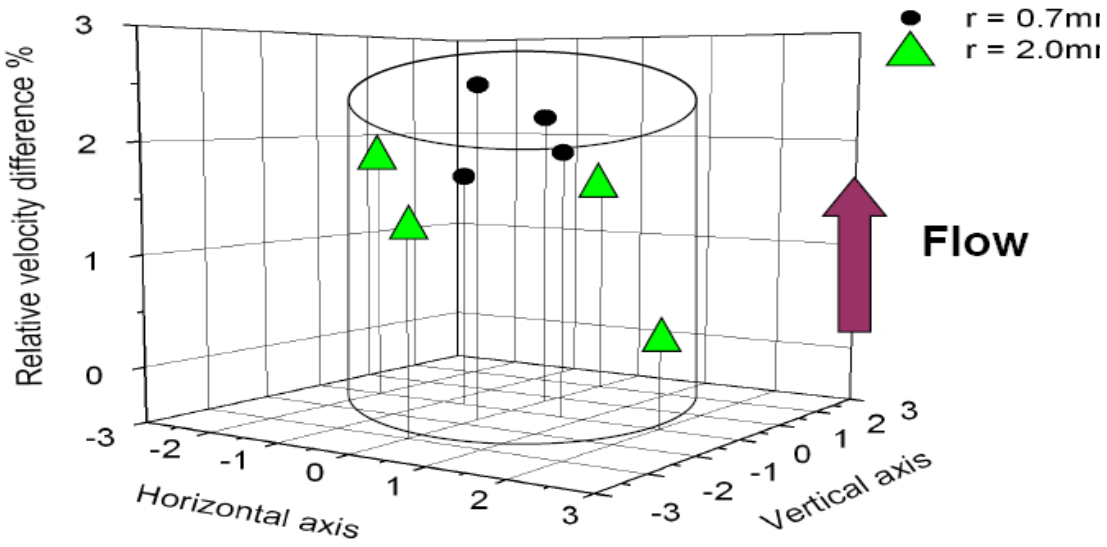

Figure 3.3. 3D spatial distribution of the relative differences between the local mobile phase velocity and the mobile phase velocity at the column center for the HALO.

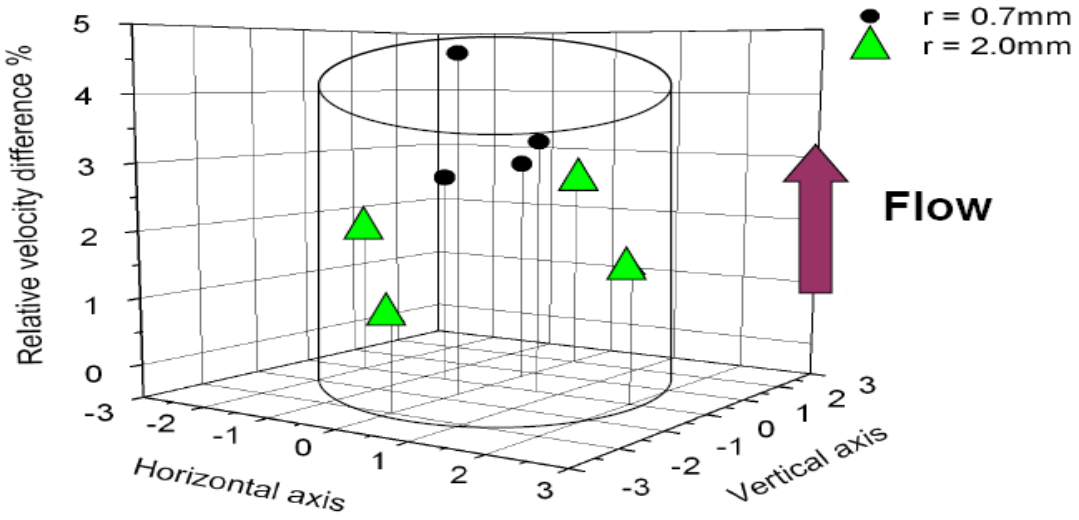

Figure 3.4. 3D spatial distribution of the relative differences between the local mobile phase velocity and the mobile phase velocity at the column center for the LUNA

For columns packed by the slurry packing process, the bed is compressed during the packing process by the stress due to the hydraulic pressure applied to the slurry. This stress becomes denser along the wall because there is friction not only between the particles, but also between the bed and the column wall [69, 93-96]. The result is a cylindrical distribution of the packing density, resulting in fluctuations along the column of its local porosity, its permeability and its retention characteristics.

The numerical values obtained for the radial variations of the relative differences of local velocities of the mobile phase at the exit of the column are similar to those measured earlier, with a local spectrometric detection on columns packed with Zorbax particles that were coarser (average diameter 10µm) [26]. Values of between 2 and 5% had been reported in this earlier work. Although slightly better, the radial homogeneity of the HALO column is not markedly different from those of the Zorbax column [26] and from the LUNA column studied in this work. This is an important observation since the HALO column is credited for its relatively exceptionally high chromatographic performance. Thus, our results suggest that such higher performance is not the consequence of a greater radial homogeneity of the columns packed with this material [35].

In summary, for the particle-packed HALO and LUNA columns, the mobile phase velocities was found to be lower at the wall region, as was reported by previous authors [22-29, 93] suggesting a denser packing at this region. A denser packing of the wall region would be due to the consequences of the

distribution of stress applied to the particles during the packing process, to their slippage with respect to each other and to the column wall, and to the strain distribution caused by this slippage. The higher strain regions are those where the local external porosity, hence the permeability, are reduced.

3.2.2. At the Exit Cross Section of the Monolithic Columns

The two silica-based monolithic columns investigated were a 10 × 100 mm semi-preparative C18 column, and a 4.6 x 100 mm C_{18} column. Both columns are silica based and have a bimodal porous silica structure. The macropores are 2μm in average diameter; the mesopores are about 13 nm.

The radial distribution of the mobile phase velocity was determined by injecting small amounts of p-benzoquinone and recording its elution in different locations at the column outlet and the velocities are reported in the same manner as for the particle-packed columns.

For the semi-preparative (SemiPrep) monolithic column, radial velocity distribution was plotted against the angular position at different distances from the center of the exit cross section. Figure 3.5 shows the 3D plots of the local distribution of mobile phase velocities. This distribution is not smooth, and a general trend is clear. The length-average velocity along the column increases markedly from the center to the wall, suggesting a similar increase of the external porosity from the central region to the wall region. On average, these variations, although significant, are small (about 4%). From the Kozeny-Karman correlation, a variation of the axial velocity by 4% corresponds to a variation of the external porosity slightly smaller than 1%.

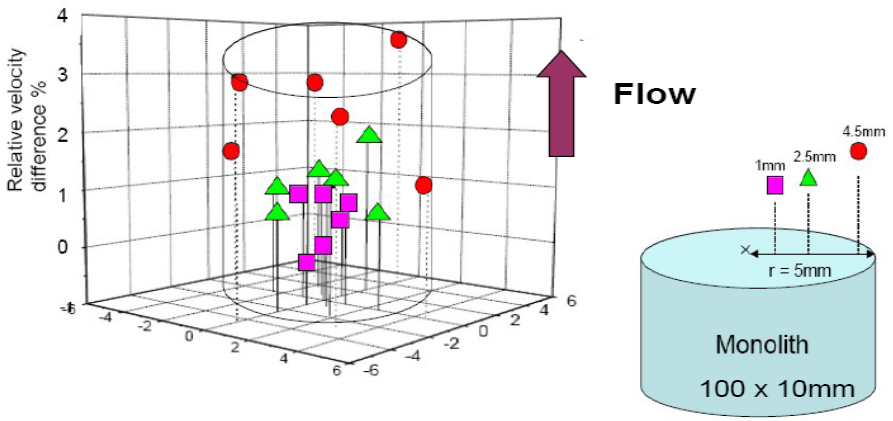

Figure 3.5. 3D spatial distribution of the relative differences between the local mobile phase velocity and the mobile phase velocity at the column center of the SemiPrep monolithic column.

Such a variation is obviously far too small to be visible on photographs such as the ones obtained using SEM that shows the macroporous and mesoporous structure of a monolithic silica rod to be fairly uniform [58]. With our detector, such localized small changes are observable and quantified. Granted, the relative velocity differences fluctuate significantly but they increase systematically with increasing distance from the column center. The fluctuations recorded illustrate the lack of homogeneity and of cylindrical symmetry of this monolithic bed. Again, such systematic variations, from the column center to its wall region, are relatively moderate with amplitude of the velocity differences that does not exceed 4%. Our results are consistent with the origin of the heterogeneity for a silica-based monolithic column discussed earlier by Guiochon et al. [93]. The most likely reason could be the strain resulting from the stress caused by the

shrinkage of the monolithic rod during the process of its polymerization and drying. During this process, the silica layer close to the wall is inelastically deformed as it is pulled, and eventually snaps from the wall of the tube in which it is being prepared. The consequence of this is likely a slightly greater local porosities in the wall region [20], leading to a faster percolation of the mobile phase as evidenced by the higher mobile phase velocities recorded in the wall region.

3.2.3. At the Exit of a Flat Wide Column

Because the bed of a thin layer column is thinner and much broader than the diameter of conventional column beds, the homogeneity of the flat wide beds that we make must be carefully monitored. It is necessary to prepare column beds through which the flow velocity of the mobile phase is uniformly distributed, so that the front of a breakthrough band would be flat. Because our instrument uses localized micro-electrochemical detectors, it is easy to measure and compare the lateral variations of the mobile phase velocities. Because the flat bed is very thin (0.1cm thick), it was not possible to make radial distribution measurements. Instead, measurements were obtained in the lateral direction at the exit of the flat bed. Figure 3.6 shows the lateral distribution of the retention times of p-Benzoquinone across the exit of the flat column bed. This distribution of the retention times across the bed is not flat, but with a random fluctuation of less than about 4%, it is comparable to the results obtained for the relative amplitude of the radial velocity distribution observed for the analytical columns used in HPLC [97, 98].

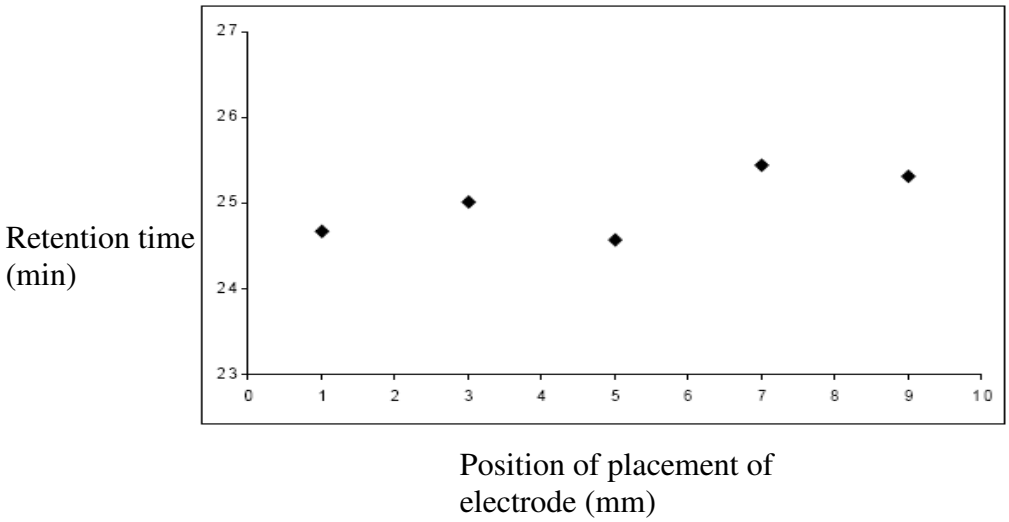

Figure 3.6. Distribution of retention time for p-Benzoquinone across the exit of the flat column bed.

3.3. Distribution of Column Efficiency

It is desirable for chromatographic columns to elute sharp and symmetrical peaks. However, peaks broaden during their elution, due to axial dispersion and to the mass transfer resistances [99]. The theories of band broadening generally consider that the column is radially homogeneous; however, it is now an undisputed fact that columns are not radially homogeneous**.** The column efficiency depends on some of its physical characteristics and on the velocity of the mobile phase. Typically, this efficiency is derived from the width of the recorded elution peaks. The efficiency in this section is given by Eqn. 1.5. The height equivalent to a theoretical plate (HETP) is given by Eqn. 1.4 and Eqn. 1.6.

3.3.1. At the Exit Cross Section for the Particle Packed Columns

Plots in Figures 3.7 and 3.8 show 3D radial distribution of the local efficiencies for the HALO and LUNA columns investigated in this study.

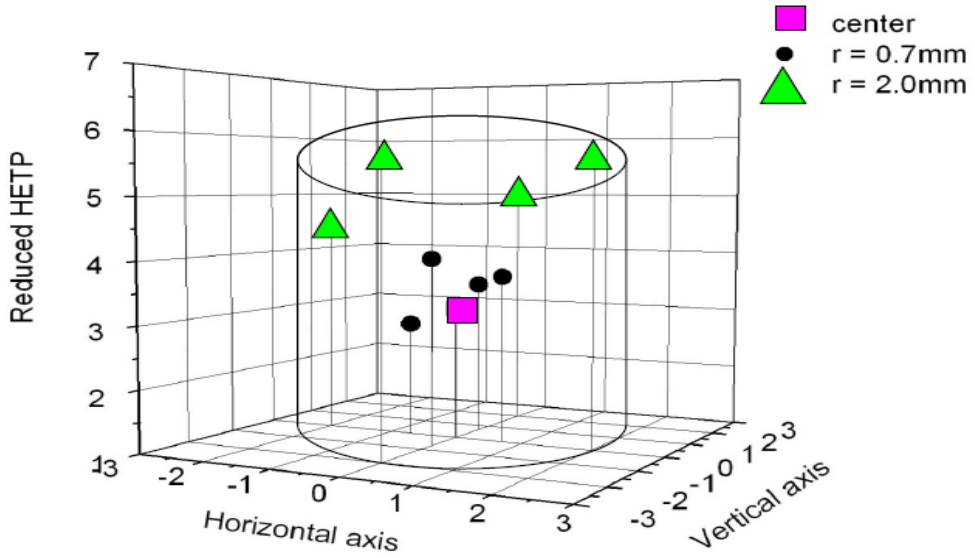

Figure 3.7. 3D spatial distribution of reduced HETP for HALO.

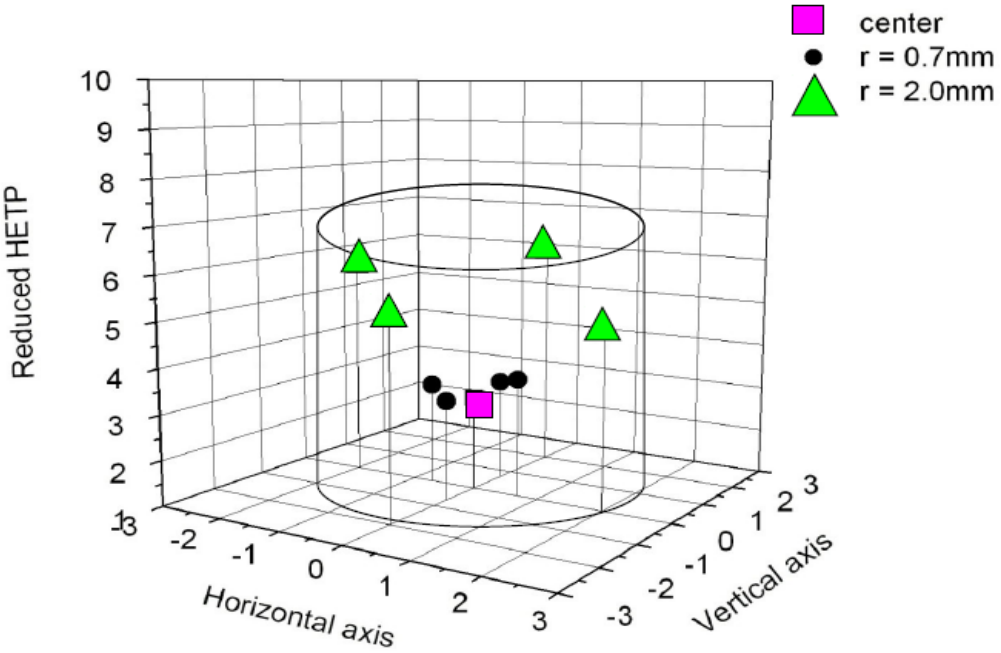

Figure 3.8. 3D spatial distribution of reduced HETP for LUNA.

For both particle packed columns, these distributions are not smooth but vary along the column section. This is due to the radial heterogeneity of these columns. However, some distinct trends can be observed for both the HALO and LUNA columns. The highest local HETP values are found well into the wall region, while the HETP is smaller in the center core region. The local efficiency varies systematically. For the two columns, the efficiency is nearly constant in a core region that has a diameter about one third of the column diameter. For the HALO column, the efficiency is about a third lower in the wall than in the core regions. For the LUNA column the efficiency is nearly 40% lower in the wall than in the core regions. The lower efficiencies recorded in the wall regions are due to the elution profiles in these regions being more diffuse than those that are recorded in the core region [8, 90].

3.3.2. At the Exit Cross Section for the Monolithic Columns

A 3-D spatial distribution of the efficiency for the silica-based analytical monolithic (4.6 x 100 mm C18) column is shown in Figure 3.9. The efficiency is nearly constant in a core region that has a diameter about one third of the column diameter. It is lower in the wall region for this monolithic column than in the core region by about 25%. Figure 3.10 shows a 3-D plot of the column efficiency (H in μm) *vs*. the location of the point where the efficiency was measured in the column cross section for the 10 × 100 mm SemiPrep monolithic column. The column HETP increases systematically from the column center to the wall region. It is approximately 13μm in the column center and twice as large in the wall.

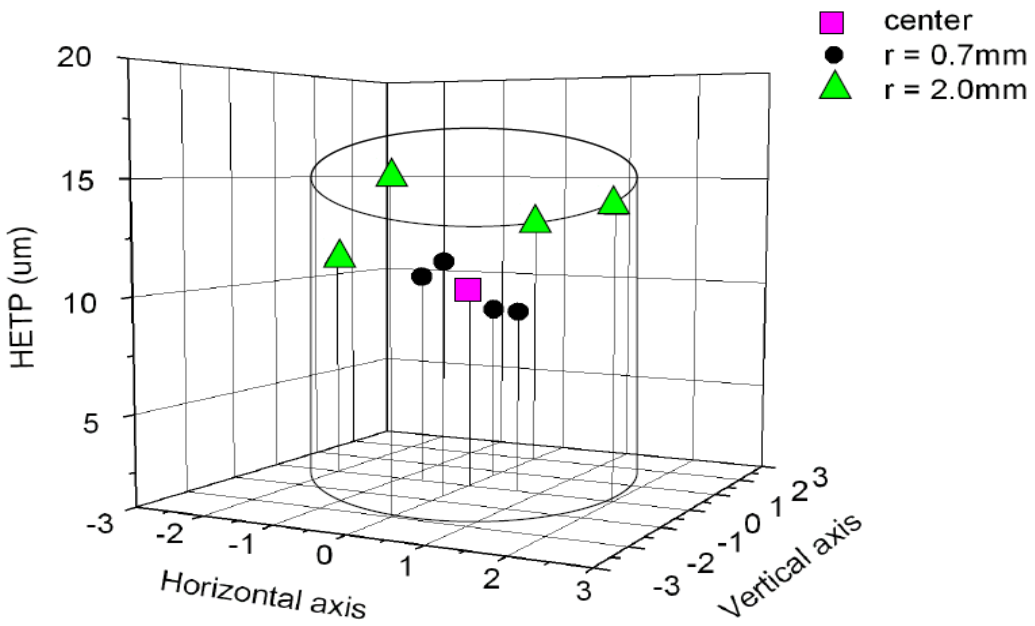

Figure 3.9. 3D spatial distribution of HETP for the analytical monolithic column.

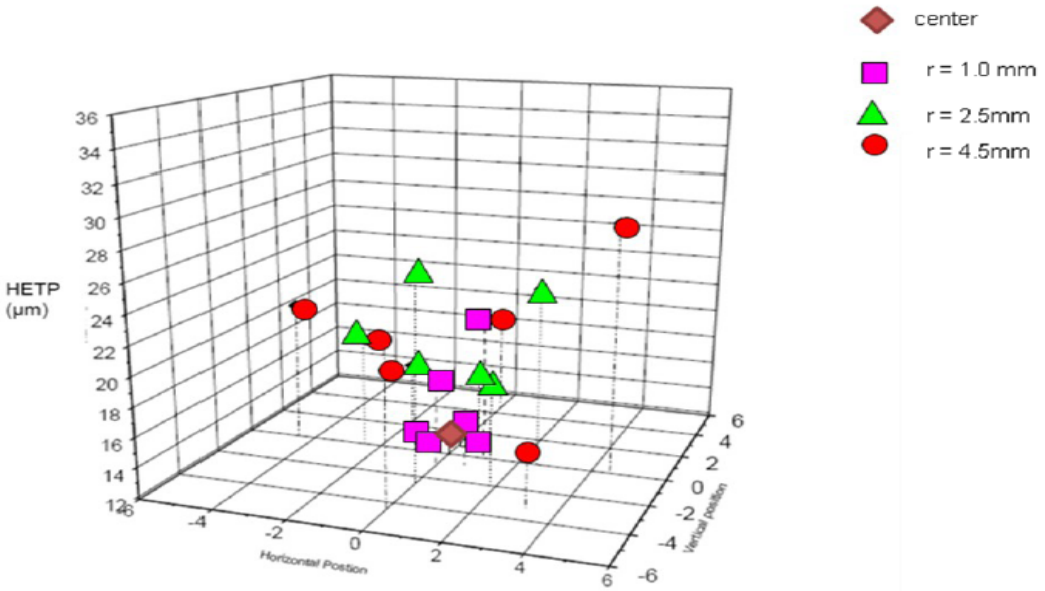

Figure 3.10. Spatial distribution of the column efficiency at the exit cross section for the SemiPrep monolithic column.

These results demonstrate how widely the column efficiency varies with increasing distance from the column center. Figure 3.11 suggests that the variation in the column efficiency significantly results from a systematic variation of the peak profile with increasing distance from the center, more than from the variations of the local mobile phase velocity. This would mean that the network of throughpores is nearly homogeneous in the column center but increasingly less so with increasing distance from the column center.

The fluctuations of the local efficiency along two perpendicular axes are shown in Figure 3.12. While the efficiency is nearly constant in a narrow region around the center of the column, the changes take place at very different rates in the external boundary of this narrow region, depending on the direction followed. The HETP is much lower near the column center than in the wall region but the largest values are not at the points closest to the wall. This illustrates the radial heterogeneity of the column and that the throughpores distribution is not uniform.

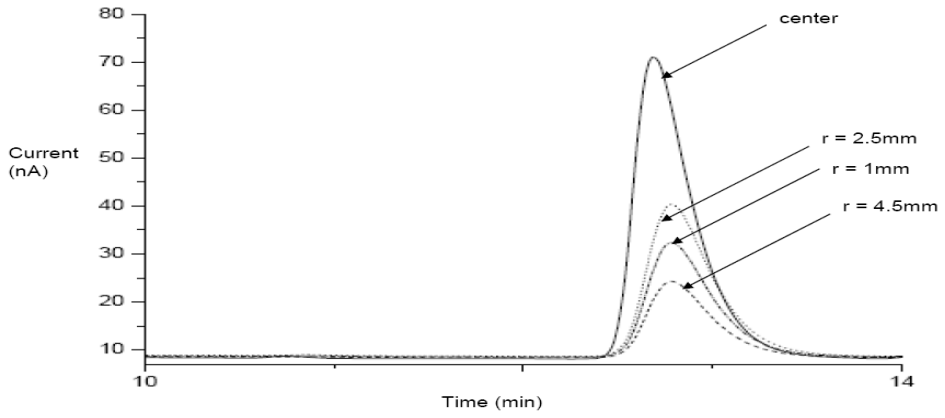

Figure 3.11. Elution profiles of four peaks recorded at the column center and distances of 1, 2.5, and 4.5 mm from the center for the SemiPrep monolithic column.

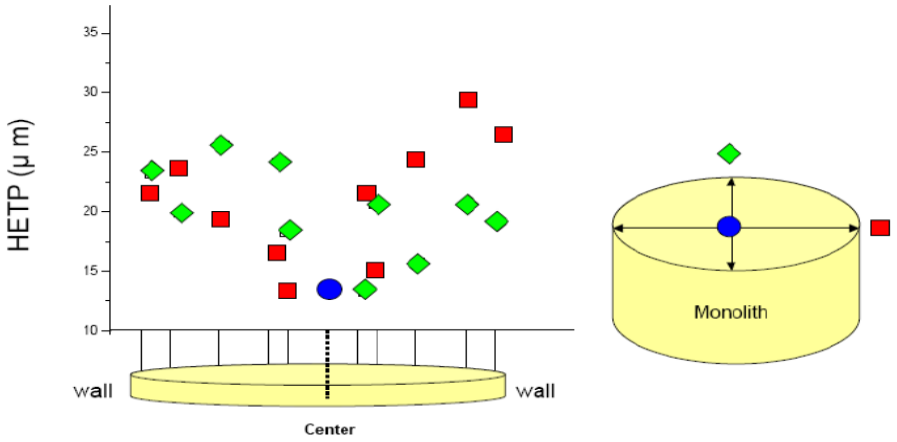

Figure 3.12. Local column efficiency along two perpendicular axes at the column exit for the SemiPrep monolithic column.

3.3.2.1. Radial Distribution of the Contributions to Band Broadening for the Silica-Based Semi-Preparative Monolithic Column

The electrochemical microdetector was placed at different positions at the exit of the SemiPrep monolithic column, and the elution peak profiles were recorded at different mobile phase flow velocities. From these profiles, the HETP (*H*) plots were generated at each of these locations. Mobile phase flow rates from 0.25 to 4.0 mL/min, with increments of 0.25mL/min were used. *H* was calculated using Eqns. 1.4 and 1.5. For each flow velocity, in each location, four records were obtained (RSD ≤ 1.05%) and the average is reported. The experimental plots were fitted to the Knox equation (Eqn 1.8) [65], providing the radial distribution of the three main contributions to band broadening, eddy diffusion (*A*), axial molecular diffusion (*B*), and the mass transfer resistances (*C*). For all positions of measurements, a mean square error of not less than 0.983 was obtained, showing the fittings were valid.

Figure 3.13 shows an overlay of the HETP plots at the center and at a 1 mm distance from the center for the SemiPrep monolithic column. It can be seen from Figure 3.13 that the minimum value of the local HETP can fluctuate by a factor of nearly 3 along a narrow circle around the column center. However, these fluctuations originate essentially in the *A* term. The four curves seem to be similar, merely translated parallel to the *H* axis. In contrast, while the minimum value of the HETP curve at the column center is in the low range, the value of the *C* term is much higher than the average for the other four curves. The *A* term is markedly reduced but the *C* term is much higher.

3.3.2.1.1. Distribution of the Eddy Diffusion Term across the Column Exit

In the eddy diffusion process, peak broadening takes place due to the statistical variations in the length of the different paths that the analyte molecules may follow when passing from one end of the column to the other end. Figure 3.14 shows the local distribution of the values of the eddy diffusion term. A general trend can be observed. The values of the *A* term increase from the center to the wall, suggesting a similar increase in the bed tortuosity from the central region to the wall region. Figure 3.15 shows a 3-D spatial plot of the *A* values for all positions at the column exit. As expected, this distribution is far from level. The highest value of *A* can be found in the wall region. It should be emphasized also that the *A* term contribution to the total band broadening accounts for about half of the overall band spreading. Similar high *A* values have been reported earlier for monolith columns [26, 27, 63, 66, 69, 100, 101].

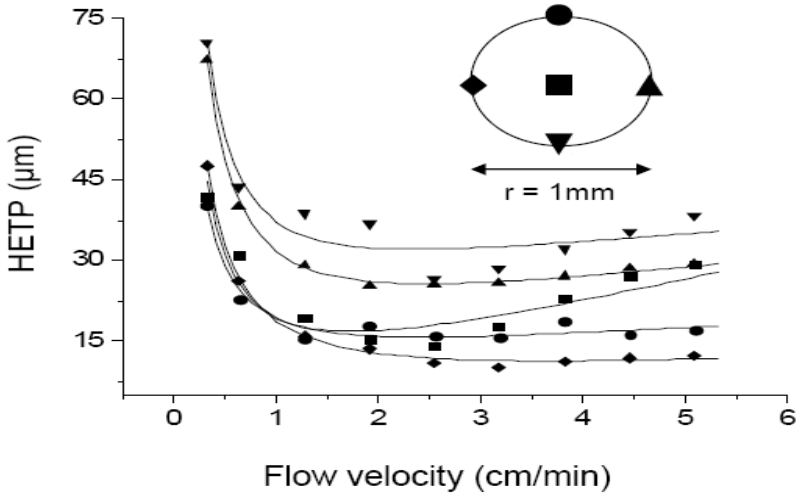

Figure 3.13. Overlay of HETP plots at the center and 1mm radius of the SemiPrep monolithic column.

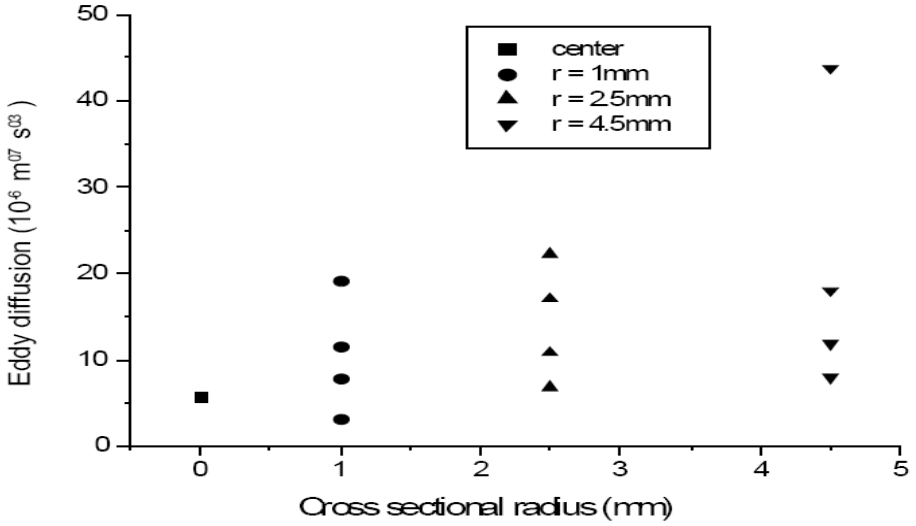

Figure 3.14. Distribution of the values of the eddy diffusion term at the center and on three concentric circles for the SemiPrep monolithic column.

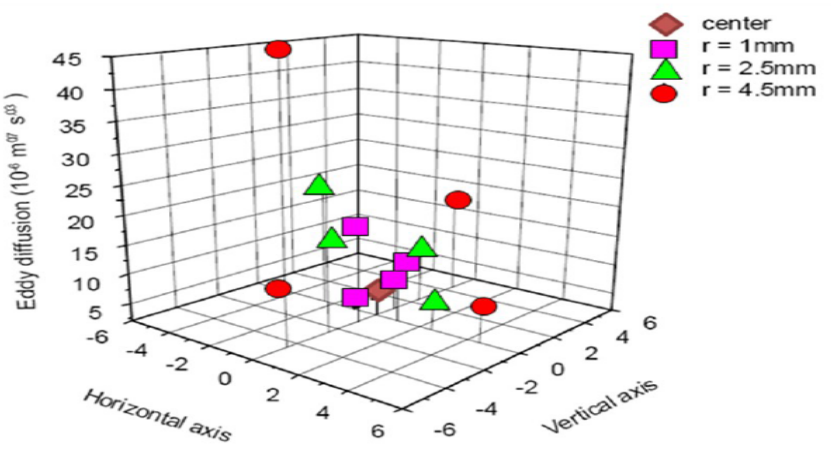

Figure 3.15. 3D spatial plot of the *A* values for all positions at the column exit for the SemiPrep monolithic column.

3.3.2.1.2. Distribution of the Axial Molecular Diffusion Term across the Column Exit

Axial molecular diffusion (*B*) refers to the diffusion of analytes against concentration gradients, from the center of a concentrated band to either side of this band, due to Brownian motion in the mobile phase [102]. This diffusion process takes place whether there is flow along the column or not. Figures 3.16 and 3.17 shows 3D plot of the local *B* values, and the average *B* values (with the standard error of the mean indicated) with respect to column cross sectional radius for the SemiPrep monolithic column.

No particular trend is observed in the distribution of the *B* values, although we noticed somewhat less fluctuations in the wall region of the column than in its central region. This is understandable since the radial concentration gradient of the analyte is not fully relaxed at the exit of the column [100]. Overall, the average values of the *B* term remain fairly constant throughout the whole column.

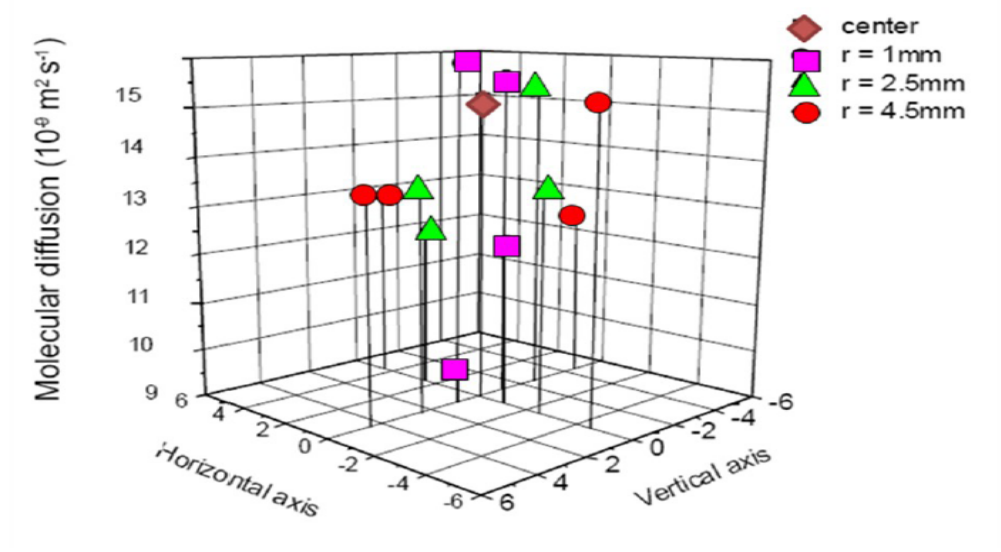

Figure 3.16. 3D spatial plot of the *B* values for all positions at the column exit for the SemiPrep monolithic column.

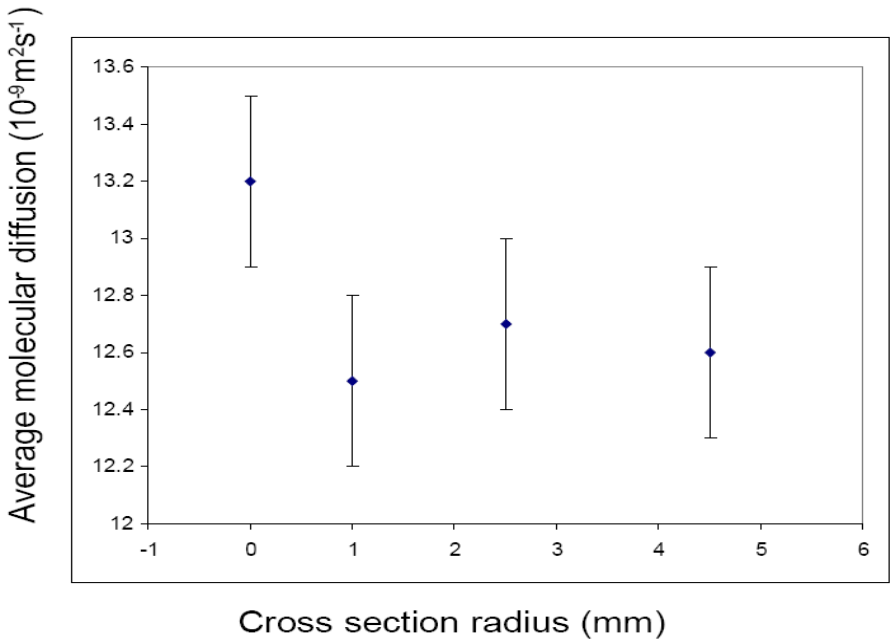

Figure 3.17. Plot of average molecular diffusion values with respect to column cross sectional radius for the SemiPrep monolithic column.

3.3.2.1.3. Distribution of the Mass Transfer Resistance Term across the Column Exit

The mass transfer resistance or influence of the finite kinetics of exchange between the percolating mobile phase that flows between particles of packing material and the stagnant mobile phase impregnating the porous volume of these particles is responsible for this contribution to band broadening called mass transfer resistance (*C term*) [66, 69]. The existence of the resistance to mass transfer means that equilibrium conditions between the mobile and the stationary phase can never be achieved in the column. Figure 3.18 and 3.19 shows a 3D plot of the local *C* values as a function of their position and the average *C* value (with the standard error of the mean indicated) versus increasing distance from the column center.

Figure 3.18 show that the generally smallest *C* values are found close to the wall region of the column, meaning that there is enhanced mass transfer at that location. This might be explained by an increased porosity of the wall region, so that the mobile phase percolates faster in the wall region than in the core region. This result is consistent with our earlier measurements for radial distribution of mobile phase velocity where it was found that the mobile phase velocity was about 4% greater in the wall region of this column than in its central region for the SemiPrep monolithic column. The plot of the average *C* value versus increasing distance from the column center (see Figure 3.19) shows some irregularity. However, the general trend is that of a slow decrease of the mass transfer resistance as one moves away from the column center.

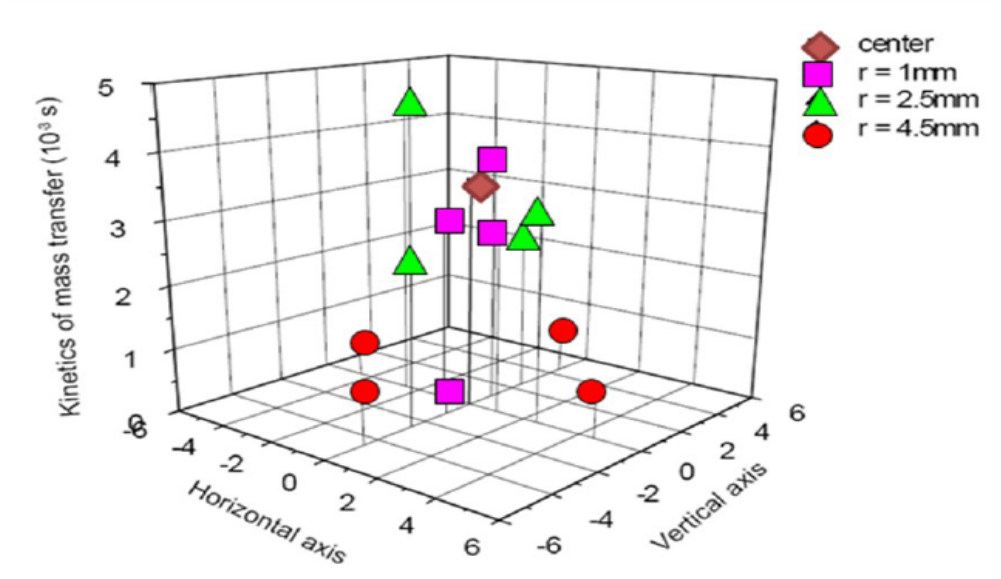

Figure 3.18. 3D spatial plot of the *C* values for all positions at the column exit for the SemiPrep monolithic column.

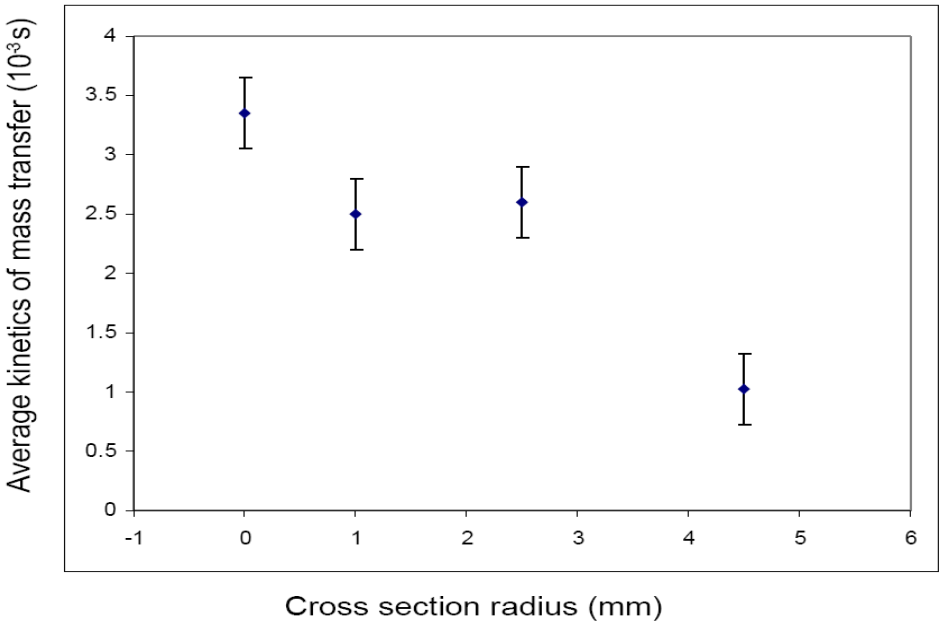

Figure 3.19. Plot of average mass transfer resistance values with respect to column cross sectional radius for the SemiPrep monolithic column.

3.3.3. Efficiency Distribution at the Exit of the Flat wide Column

The efficiency of a flat wide or thin layer chromatographic bed is an assessment of its capacity to maintain narrow and short zones and to restrain the axial and lateral dispersion of a solute migrating along the bed. Plate height equations that explicitly describe axial and lateral dispersion in thin layer chromatography have not have been developed [103]. Since our setup allows a precise adjustment of the mobile phase velocity and the recording of the profiles of elution peaks, it makes it possible to assess the efficiency of thin wide columns in much the same way as it is conventionally done in HPLC. The efficiency was calculated using Eqns 1.4 and 1.5. Figure 3.20 shows a plot of the average HETP obtained as a function of the mobile phase velocity. Each data point is the average of the value obtained for the four detectors used. The mobile phase flow velocity was gradually increased from 0.25cm/min to 2.0cm/min, and the highest efficiency was obtained at a flow of 0.50cm/min.

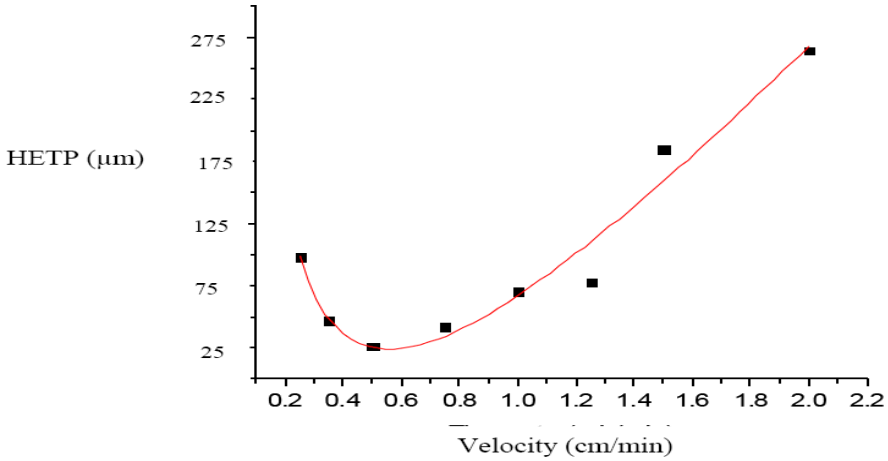

Figure 3.20. Average HETP plots simultaneously recorded by four microelectrochemical detectors at the exit of the flat wide column.

At the flow rate of maximum efficiency, the lateral variation of efficiency of the plate was obtained and was found to be fairly constant with a random fluctuation of less than about 12%. While this is significant, it is less than some variations recorded for some analytical columns used in HPLC [97].

3.3.3.1. Further evaluation of performance of the online microelectrode detector for the Flat Wide Column.

Because the thin layer chromatographic was homemade, as well as the instrument built to operate in much the same way as a conventional HPLC instrument, it was necessary to further test the performance of our instrument (especially the performance of the microelectrode detector array). To do so, the determination of the neurotransmitters epinephrine (*K' = 2.05)* and norepinephrine (*K' = 2.14)*) was investigated at room temperature. These compounds are often used to study the performance of electrochemical detectors, since the determination of neurotransmitters is one of the major applications of these detectors in HPLC [98]. The detector array was again operated in the amperometric mode and the current responses of the electrodes at the maximum of the chromatoamperometric curves for both compounds were obtained and used to plot the hydrodynamic voltammograms and the combined chromatograms for these compounds. This analysis was done under isocratic elution of 30 pg separate injection of each sample and the results is shown in Figures 3.21 and 3.22. Based on the hydrodynamic voltammograms, an applied voltage of + 0.75 *vs* Ag/AgCl was selected and used to investigate the dynamic range of the detectors.

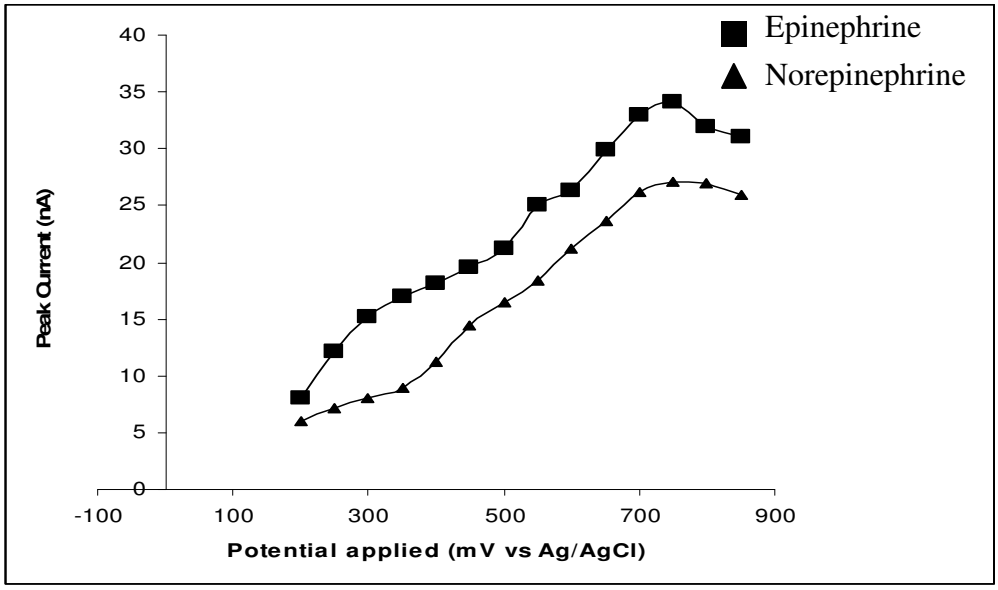

Figure 3.21. Hydrodynamic voltammograms for epinephrine and norepinephrine with isocratic elution. A flow rate of 0.5mL/min was used to elute the compounds in the mobile phase composed of 5.0 g/L of NaCl, 3.0 g/L acetic acid and 0.25 g/L of ethylendiaminetetraacetic acid in 80% methanol and 20% water.

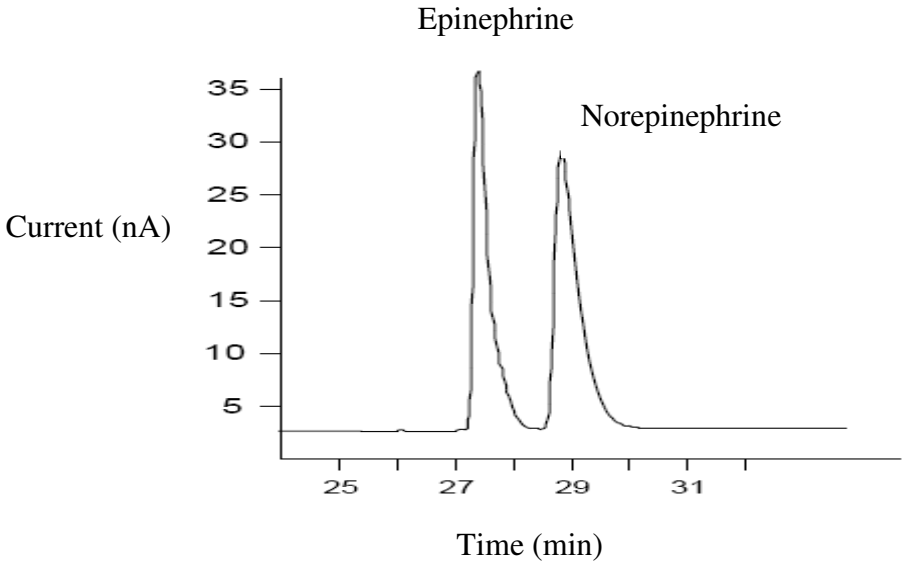

Figure 3.22. Combined chromatograms for epinephrine and norepinephrine. Recorded at +750mV *vs* Ag/AgCl. A flow rate of 0.5mL/min was used to elute the compounds in the mobile phase composed of 5.0 g/L of NaCl, 3.0 g/L acetic acid and 0.25 g/L of ethylendiaminetetraacetic acid in 80% methanol and 20% water.

All detectors gave a linear response between 4.0 pg and 20.0 ng for both compounds injected separately. Using the average value for the five detectors, the limit of detection in both cases was ~ 2.0 pg. The reproducibility of the detectors was checked by using eight successive 20.0 pg injections of both compounds, and the coefficients of variation were found to be 2.4% and 2.0% for norepinephrine and epinephrine respectively.

3.4. Distribution of Analyte Concentration across the Column Exit for Semi-Preparative Monolithic Column

The local maximum concentration of the analyte peak depends on its retention time, the local column efficiency, and the local density of the analyte. If there is a systematic radial variation of the average axial velocity, a radial concentration gradient of analyte will build up. This gradient tends to be relaxed by diffusion. Fick's law shows that a concentration gradient can be considered in practice as entirely relaxed if the Fick number (Fi) exceeds 3 [7] and is given by the equation:

$$Fi = 2\,D\,t\,/X^2 \qquad \text{(Eqn. 3.3)}$$

D is the diffusion coefficient in the system considered, t the time during diffusion takes place, and X the distance over which the gradient took place. In a chromatographic bed, the diffusion coefficient is the product of the molecular diffusivity, D_m, and of the tortuosity factor, 0.75 [7]. Under the experimental conditions of the measurements made in this work, D is of the order of 5×10^{-6} cm^2/sec, X = 0.5 cm, and t = 13 min = 780 sec. So, the Fick number is only 3 ×

10^{-2}, which means that the radial concentration gradient of the analyte is not relaxed when the band elutes. This is consistent with the significant time difference between the elution times of the peak maximum at different locations.

The calibration of the electrochemical detector was done using the breakthrough curves obtained in frontal analysis. The results gave a linear response. Figure 3.23 shows the radial distribution of the local maximum concentrations of the analyte along the two perpendicular axes at the column exit cross section. Six measurements were obtained for each location (RSD ≤ 0.8%). The measured concentration is maximal in the column center but its variations are unsymmetrical and quite different along the two axes. Along the horizontal axis, the peak height decreases faster toward the negative values of x than toward the positive values. The opposite is true along the vertical axis (y-axis).

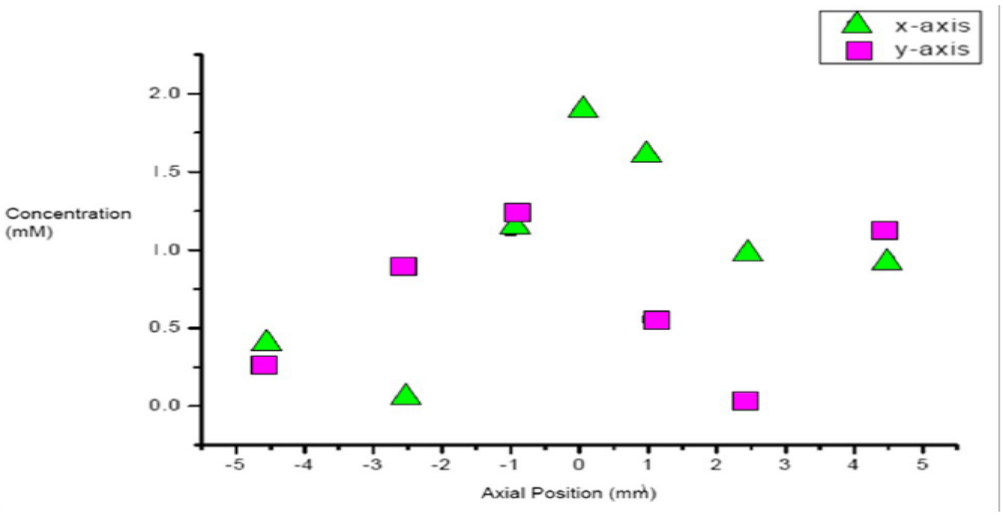

Figure 3.23. Radial distribution of local analyte concentration along two perpendicular axes at the exit cross section of the SemiPrep monolithic column.

The distribution of peak heights is not flat near the column center but is minimal along the second bisector, for $x < 0$ and $y > 0$.

For distances larger than 2.5 mm from the axis, the peak height is less than 50% of the height at the column center. The lowest peak heights were recorded close to but not at the wall. This radial heterogeneity of the concentration distribution is illustrated by the two peaks in Figure 3.24, both recorded at 1 mm from the column center. Because all peaks have similar shapes, their areas are proportional to the product of their heights (i.e., the maximum solute concentrations) and their widths at half height. These products are represented in Figure 3.25, which shows rectangles having a height proportional to the maximum solute concentration as a function of their radial distance from the center, with a number proportional to the peak area. Both rectangle heights and numbers are reported relative to the peak recorded in the column center which is normalized to be 1.0 Coulomb. The observed peak areas are not constant. Peak areas and heights decrease with increasing radial distance at a different rate.

3.5. Surface Characterization of Some Novel Bonded Phase Packing Materials for HPLC Columns Using Magic Angle Spinning-Nuclear magnetic Resonance Spectroscopy

Thus far, all reported experimental results have been on chromatographic beds that have already been consolidated. This section however probes the surface properties of the bulk materials prior to their being consolidated to make a column. The goal here is to characterize the surface properties of the novel Cogent bidentate C_{18} on type-C silica, XTerra MS C_{18},

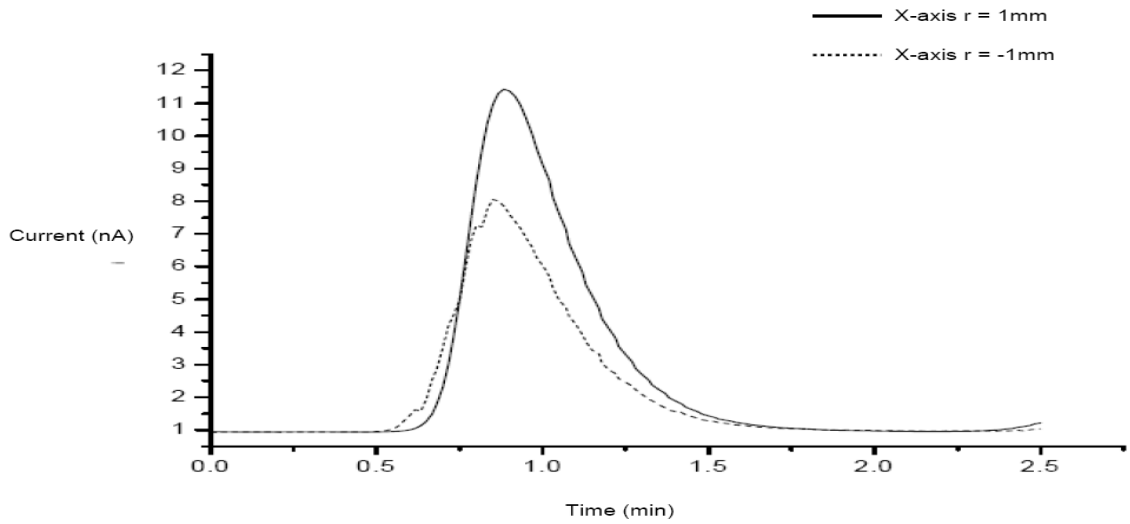

Figure 3.24. Elution profiles of two peaks recorded at two opposite positions at distance of 1mm from the center of the SemiPrep monolithic column.

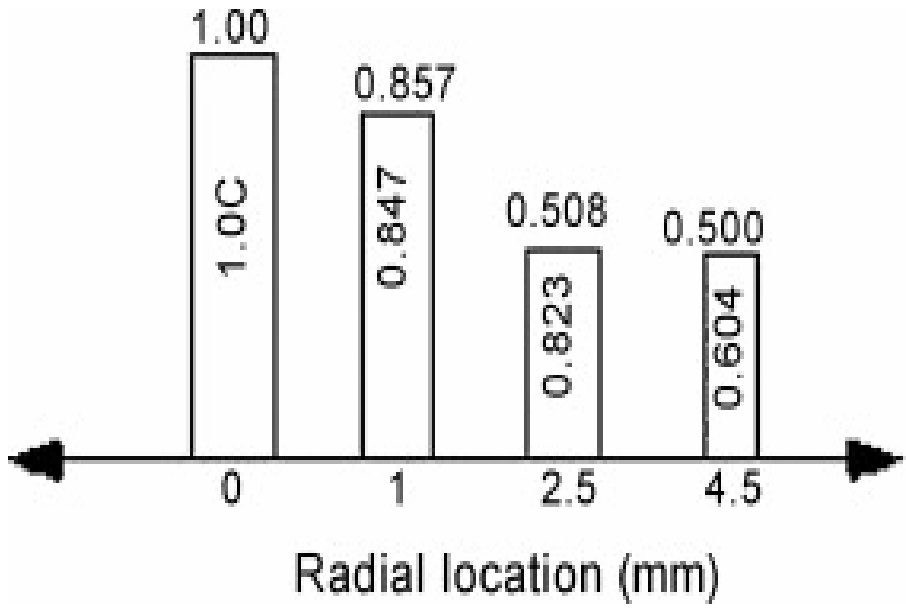

Figure 3.25. Representation of the maximum concentration and the peak area relative to the maximum concentration and peak area at the column center at different positions of the SemiPrep monolithic column.

and XBridge Prep. C_{18} packing materials using solid state ^{29}Si and ^{13}C cross-polarization and magic-angle spinning (CP-MAS) NMR, and to correlate our results to some observed chromatographic behavior of these materials. Both derivatized XTerra and XBridge have trifunctional C_{18} and trimethyl endcapping.

Also, when necessary, the relative concentrations of the different environments around silicon atoms is obtained by comparing of the relative intensities of the different silicon resonances. In general, we do recognize that caution should be exercised when drawing quantitative conclusions based on CP-MAS NMR, because CP-MAS is not an inherently quantitative technique. However, some quantitative inferences have been drawn by other authors between silicon environments based on the spectroscopic areas like Q^3, Q^2, Q^1, T^3, T^2, T^1, D^2, D^1, and M^1 environments [104]. We may do this because the CP-MAS dynamics of these environments are similar (they have similar dipolar coupling constants). While useful structural information that can be obtained for a molecule using CP-MAS, most quantitative attempts are at best relative and should not be interpreted as providing the absolute concentrations of these environments.

3.5.1. Surface characterization of the Cogent bidentate C_{18} on type-C silica

To better understand the extent of surface coverage by Si-H groups on the derivatized type-C silica, it was necessary first to record the ^{29}Si CP-MAS spectrum of an underivatized bare silica material, and is shown in Figure 3.26. Three tetrafunctional silyl groups (Q^2, Q^3, and Q^4) can be identified [105, 106]. Their identities and their relative percentage distributions are shown in Table 3.1.

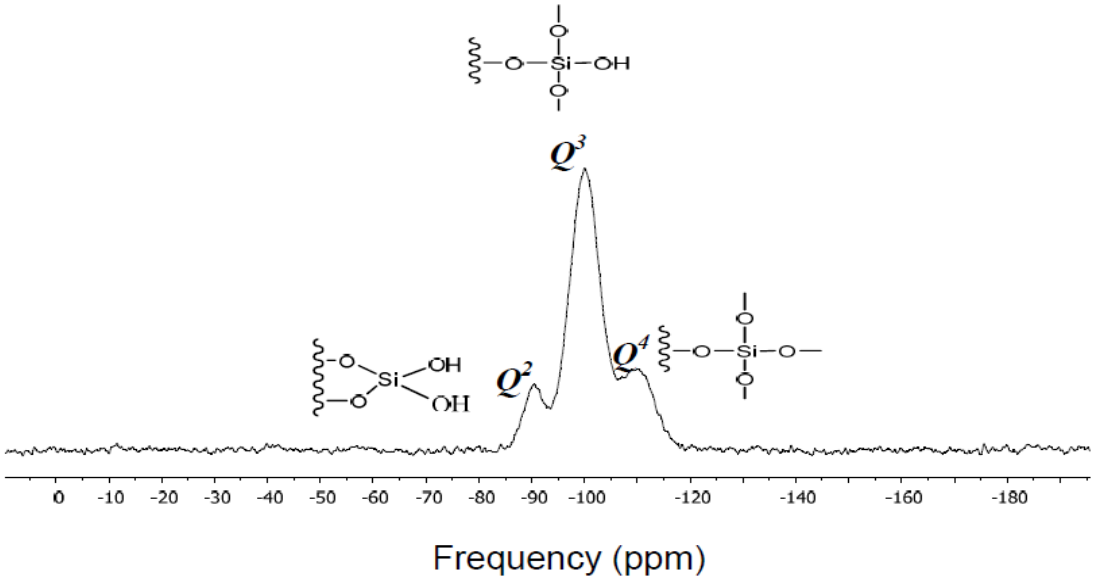

Figure. 3.26. ^{29}Si CP-MAS spectrum of bare silica.

Table 3.1. Peak assignment and their percentage distribution for bare silica.

Chemical moiety	*Percentage (% by peak area)*	*Chemical shift (ppm)*
(Q^2) 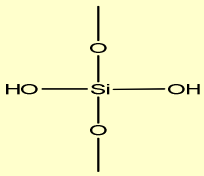	12.95%	-90.50
(Q^3) 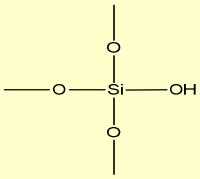	71.94%	-100.04
(Q^4) 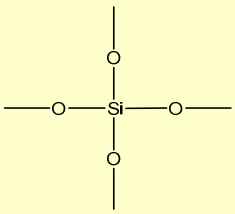	15.11%	-110.03

As expected, the bare silica surface is largely dominated by the mono-silanol groups. Figure 3.27 shows the ^{29}Si CP-MAS spectrum of the Cogent bidentate C_{18} on type-C silica sample and the peak identities as well as their percentage distributions are shown in Table 3.2. The existence of the peak at -65.47 ppm is evidence of the presence on the surface of another bonded moiety that is attached directly to the surface by a stable Si-C bond. One example of such moieties could be groups bonded to two close-by surface silicon atoms, similar with the products that are formed when an alkyne is used in the hydrosilation reaction [45].

The versatility that comes from attaching organic moieties to the surface Si-H groups leads to the possibility of producing such a stationary phase that may not be feasible by other methods. Another important observation is the dominance of the peak at -80.72 ppm. This peak is attributed to the Si-H moiety. The peak intensity corresponds to the substitution of about 80% of the original S-OH groups on the bare silica by Si-H groups. This result is in agreement with the earlier publication of Pesek et al. [45] who reported that the surface of the Cogent bidentate C_{18} on type-C silica adsorbent is predominantly populated with Si-H groups instead of the Si-OH groups that dominate the surface of ordinary silica.

The shoulder at -89.90 ppm corresponding to a silicon atom attached to two hydroxyl groups (Q^2 site) has a drastically reduced intensity for the Cogent bidentate type-C silica. This reduced intensity of the Q^2 site is an indication of the effectiveness of the substitution of silanol with silicon hydride groups in the production of this Cogent bidentate C_{18} on type-C silica adsorbent.

.

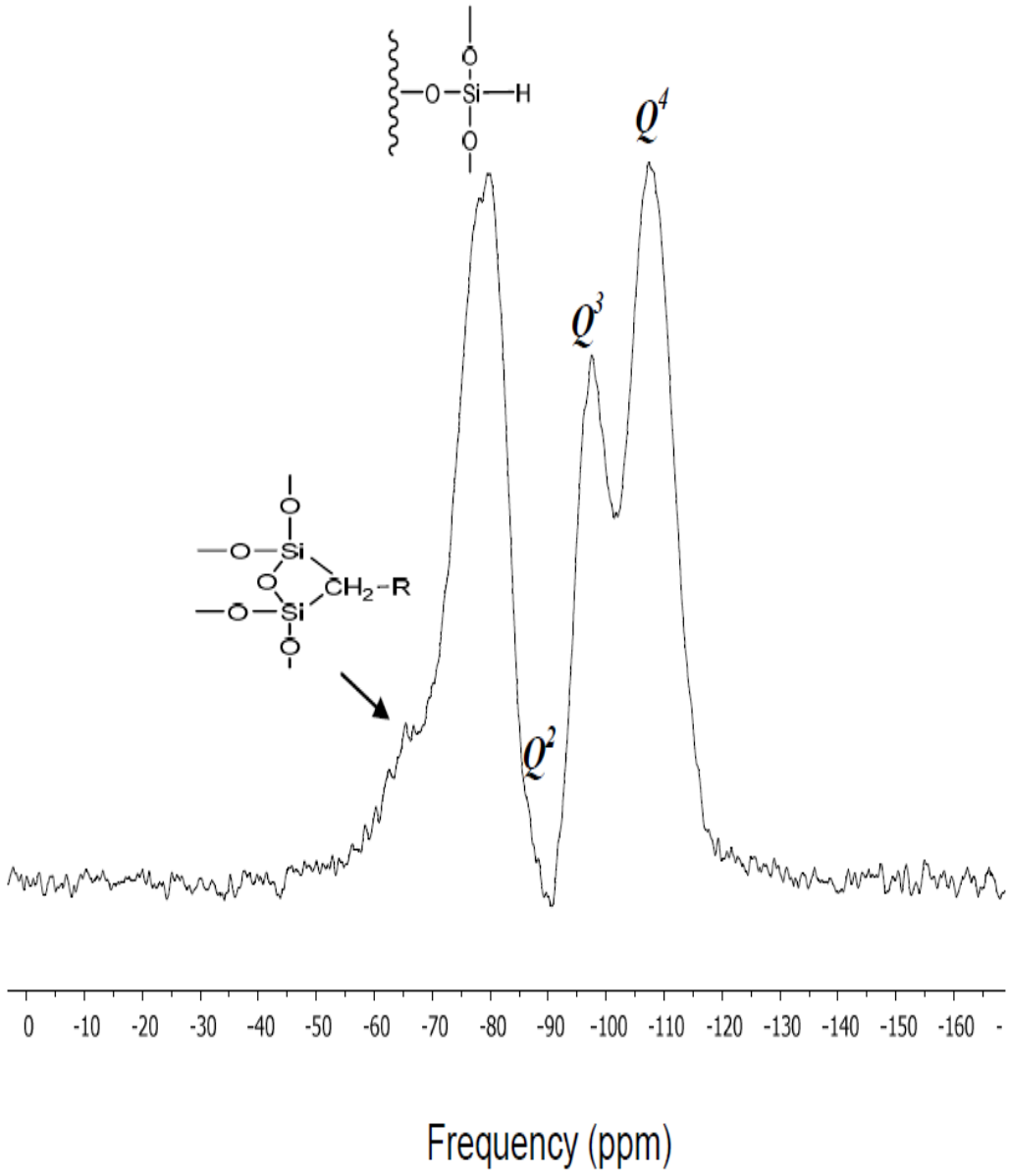

Figure 3.27. ^{29}Si CP-MAS spectrum of Cogent bidentate C_{18} on type-C silica.

Table 3.2. Peak assignment and their percentage distribution for Cogent bidentate C_{18} on type-C silica.

Chemical moiety		*Percentage (% by peak area)*	*Chemical shift (ppm)*
	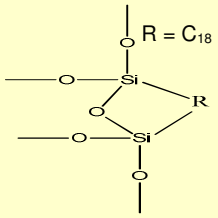	2.80 %	-65.47
	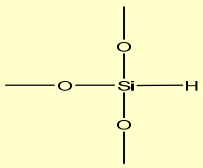	46.47 %	-80.72
(Q^2)	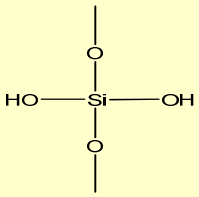	2.84 %	-89.90
(Q^3)	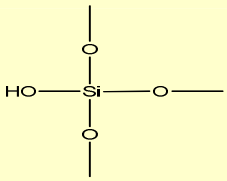	10.90 %	-99.55
(Q^4)	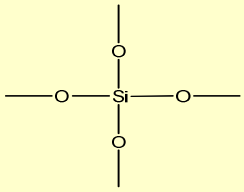	36.99 %	-110.00

However, it should be mentioned that, as determined by the ^{29}Si CP-MAS experiment (see Figure 3.27), a significant surface density of silanol groups (Q^2 and Q^3 sites) still persists on the surface of the Cogent bidentate C_{18} type-C silica. That is what prevents such a surface from being inactive. This observation is consistent with earlier findings of Gritti et al [107] who showed that the retention of basic compounds is an order of magnitude larger on Cogent than on the hybrid adsorbent (XTerra) and that peak tailings on Cogent are stronger than on XTerra. A reason that was postulated by Gritti et al. for this behavior of Cogent was the possible instability of the Si-H bond as silanol groups may rapidly form once the Cogent packing is in contact with aqueous mobile phases (due to fast hydrolysis of the Si-H bonds). Solid state NMR studies to test this latter suggestion are found in section 3.5.4.

3.5.2. Surface characterization of the XTerra packing material

The simplified molecular structure of the XTerra shown in Figures 1.10 and 1.11 will help in understanding the different Si sites expected to be represented in the CP-MAS spectra. Four silicon sites are observed in the ^{29}Si CP-MAS spectrum and are shown in Figures 3.28.

The chemical shift at -62.56 ppm is the trifunctional silicon and is attributed to a T^3 site, which is a silicon atom attached to a carbon atom ($[CSi(OSi)_3]$), while the shoulder at -53.45 ppm is attributed to the T^2 silicon site ($[CSi(OH)(OSi)_2]$). The Q^n silicon sites can be identified as well. The peak which has a -110.00 ppm shift is that of the siloxane group (Q^4), while the small peak at -99.93 ppm corresponds to the Q^3 site [71, 104].

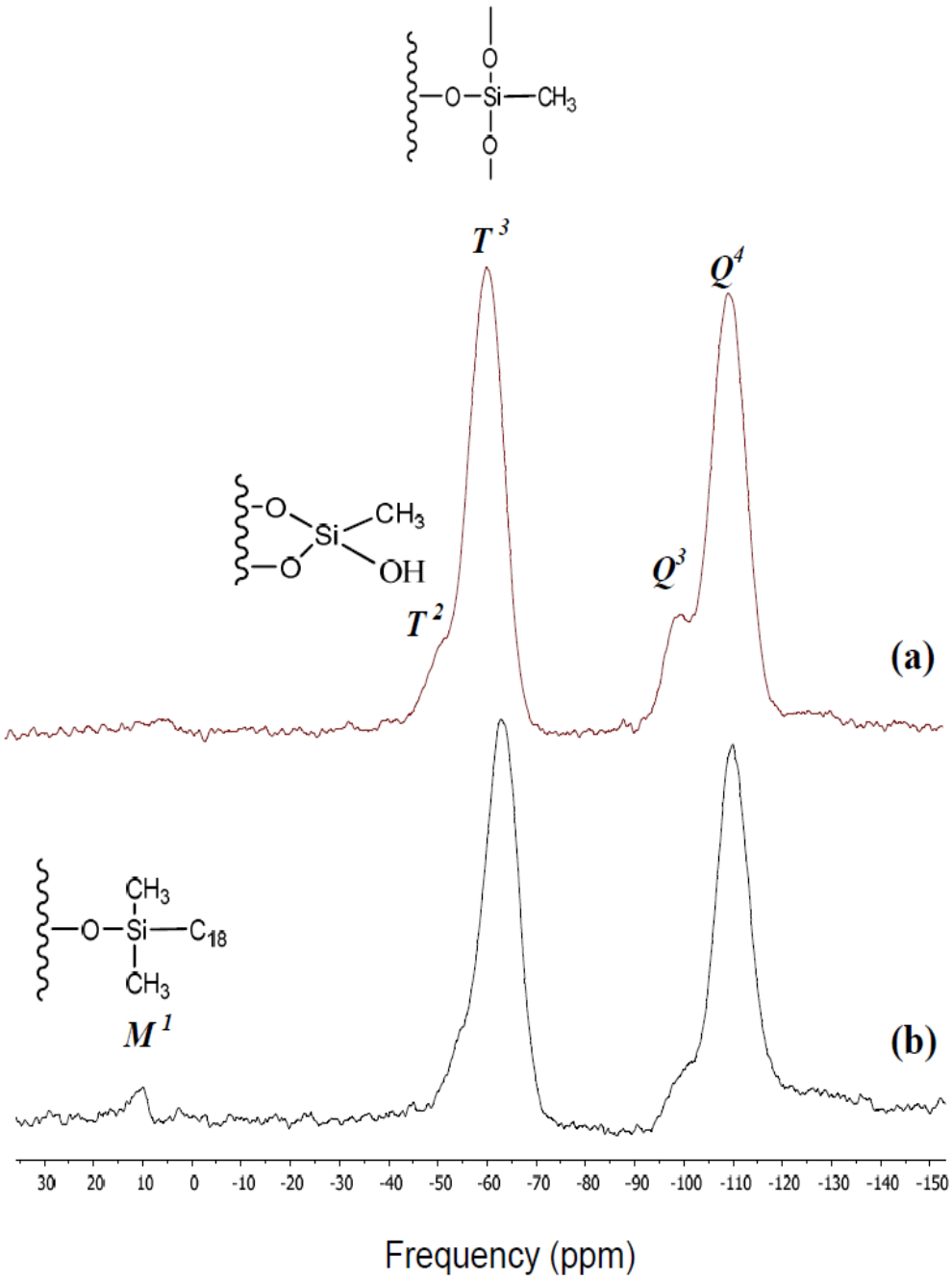

Figure 3.28. ^{29}Si CP-MAS spectrum of underivatized XTerra (a) and XTerra MS C_{18} (b)

By making relative comparisons between the T^2 and T^3 sites, it was determined that greater than 90% of the methyl silicon atoms are within the completely condensed T^3 environments. For XTerra MS C_{18}, the peak identities are the same for the silicon sites Q^4, Q^3, T^3, *and* T^2 as they are for the underivatized XTerra.

A notable addition for the XTerra MS C_{18} is the M^1 environment (peak at +11.27 ppm). This is expected because these hybrid packing materials have trimethyl endcapped units. Also, as can be expected, the relative intensity for the corresponding silanol peak (Q^3) is greatly diminished upon derivatization. The relative amount of Si-OH groups on the surface of the XTerra MS C_{18} is estimated to be less than 5%.

Therefore, a great majority of silicon atoms do not bear the silanol groups, which is consistent with earlier published chromatographic results showing that the retention of basic compounds is at least an order of magnitude smaller on XTerra MS C_{18} than on Cogent or other conventional material prepared by derivatizing high-purity B-type silica particles with monofunctional silanes [107].

To corroborate that the molecular structure of these hybrid packing materials contain both organic and silica units, ^{13}C CP-MAS spectrum was obtained for XTerra MS C_{18} and is shown in Figure 3.29. The bundle of peaks from +16 to +36 ppm is typical of the presence of the C_{18} ligands with the predominant peak at 32.33 ppm corresponding to the main $–CH_2$ chain [104]. The carbons of the endcapped trimethylsilane also show up at -0.36 ppm.

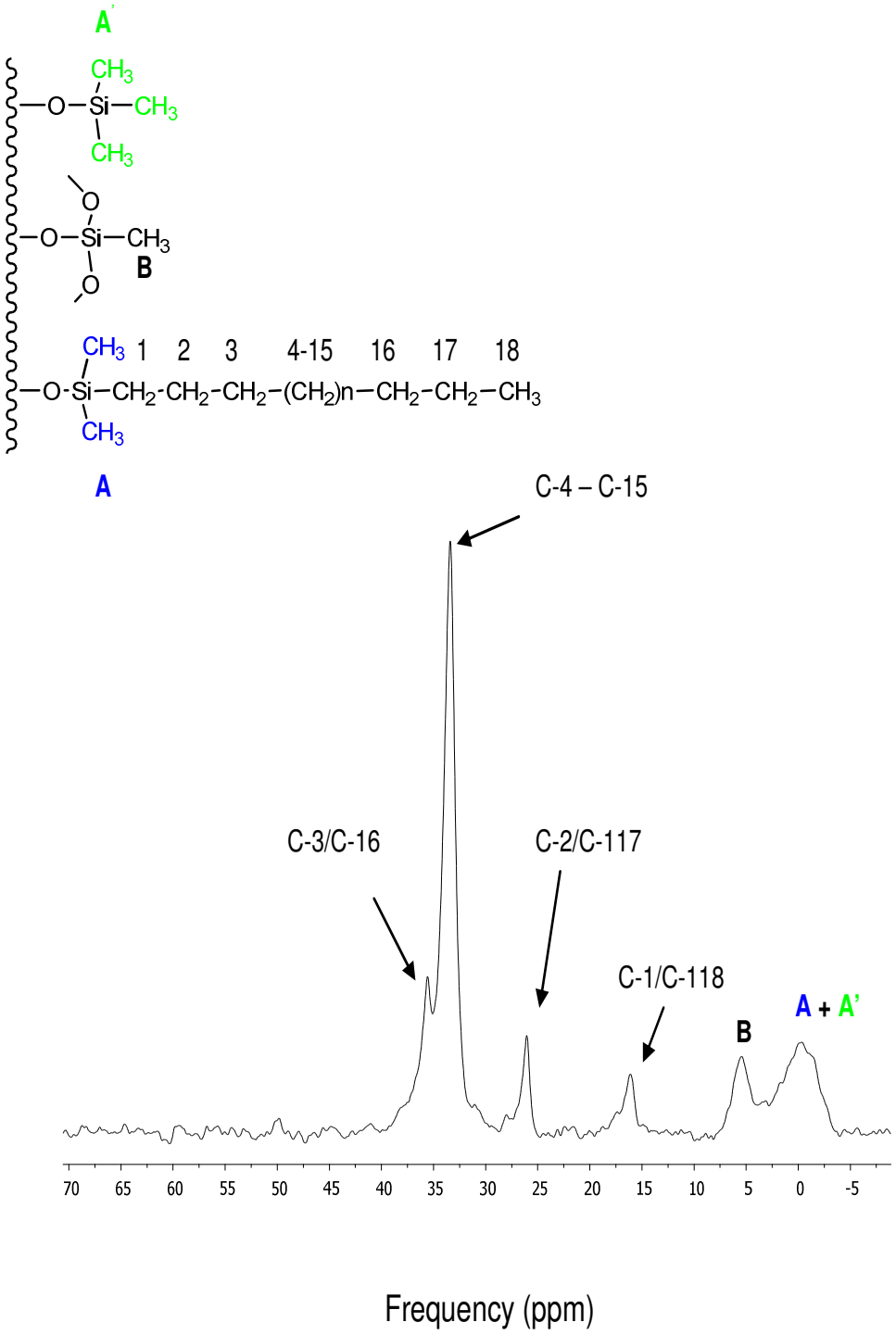

Figure 3.29. ^{13}C CP-MAS spectra and peak assignments for XTerra MS C_{18}.

3.5.3. Surface characterization of the XBridge packing material

The ^{29}Si CPMAS spectra acquired for the XBridge hybrid materials are shown in Figure 3.30. It can be seen that two main peaks are observed for the underivatized XBridge. The peak at -62.09 ppm (T^3) is attributed to silicon atoms attached to carbon atoms while the one at -110.00 ppm (Q^4) is that of a siloxane [104]. This also is evidence that the molecular structure of these hybrid packing materials contain both organic and silica units. The small peak at -100.05 ppm (Q^3) is attributed to a silanol group, while the shoulder at -53.16 ppm corresponds to the T^2 environment [106]. Similar to the XTerra, by making relative comparisons between the T^2 and T^3 sites, it was determined that the majority of ethyl bridged silicon atoms (> 90%) are also within the completely condensed T^3 environments.

For XBridge Prep C_{18} (see Figure 3.30b), the identities of the peaks Q^4, Q^3, T^3, *and* T^2 remain unchanged relative to the underivatized XBridge because these different silicon sites are the same. Noteworthy is the presence of the M^1 environment at resonance of +12.07 ppm. The peak intensity for the corresponding silanol peak (Q^3) is greatly diminished as is expected upon derivatization.

3.5.4. Hydrolytic Stability of packing materials in aqueous conditions

The incorporation of organic moieties in the silica matrix, which is achieved in XTerra and XBridge materials, reduces the silanols activity. Earlier experimental results showed that this was more successful in reducing the peak tailing of basic compounds than the Cogent bidentate C_{18} [107].

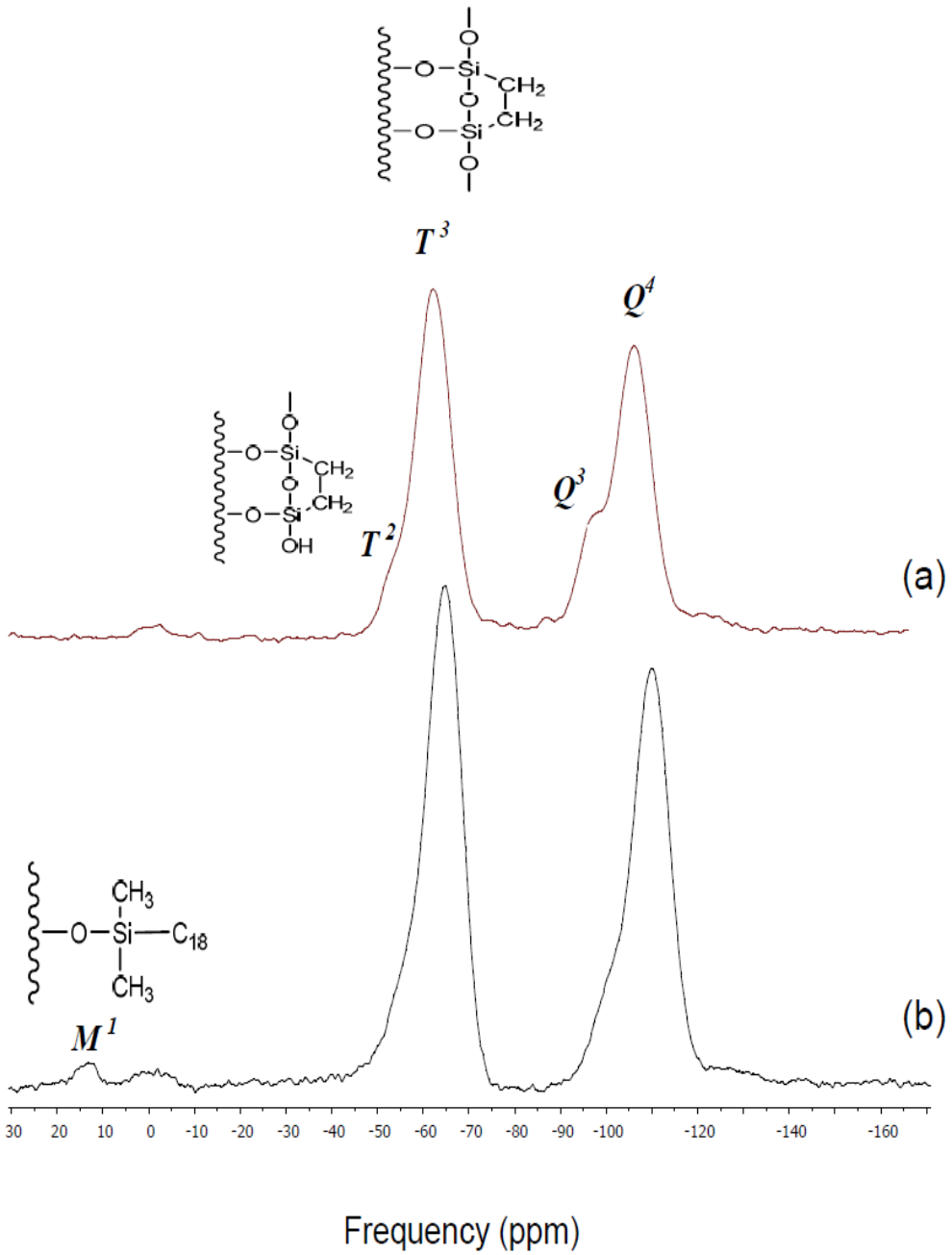

Figure 3.30. ^{29}Si CP-MAS spectra for underivatized XBridge (a) and XBridge prep C_{18}

The stability of the Si-H bond was questioned, in that silanol groups may rapidly form once the Cogent packing is in contact with aqueous mobile phases, due to the fast hydrolysis of the Si-H bonds. If this is true, then upon the hydrolytic treatment of the Cogent $C_{18,}$ a reduction in the intensity for the Si-H moiety can be expected in the ^{29}Si CP-MAS spectrum. The spectra obtained for XBridge and XTerra showed no significant difference from that of the initial bulk material. For the treated Cogent bidentate C_{18} packing material, some reduction in the peak intensity is observed for the peak corresponding to the Si-H moiety and this result is shown in Figure 3.31. As can be seen in Table 3.3, this reduction is more important for the sample that had undergone the hydrolytic treatment under more acidic conditions. Granted, we do not see many silanols on the dry powder, but earlier chromatographic evidence points to some increased silanol activity on packing Cogent C_{18} material [107]. Therefore, the hydrolytic instability of the Si-H bond is the point of reconciliation. Because the Si-H bond is not very hydrolytically stable, it gets hydrolyzed in the presence of water, especially under acid conditions. Here, we present NMR spectroscopic evidence that this possibility should not be ignored.

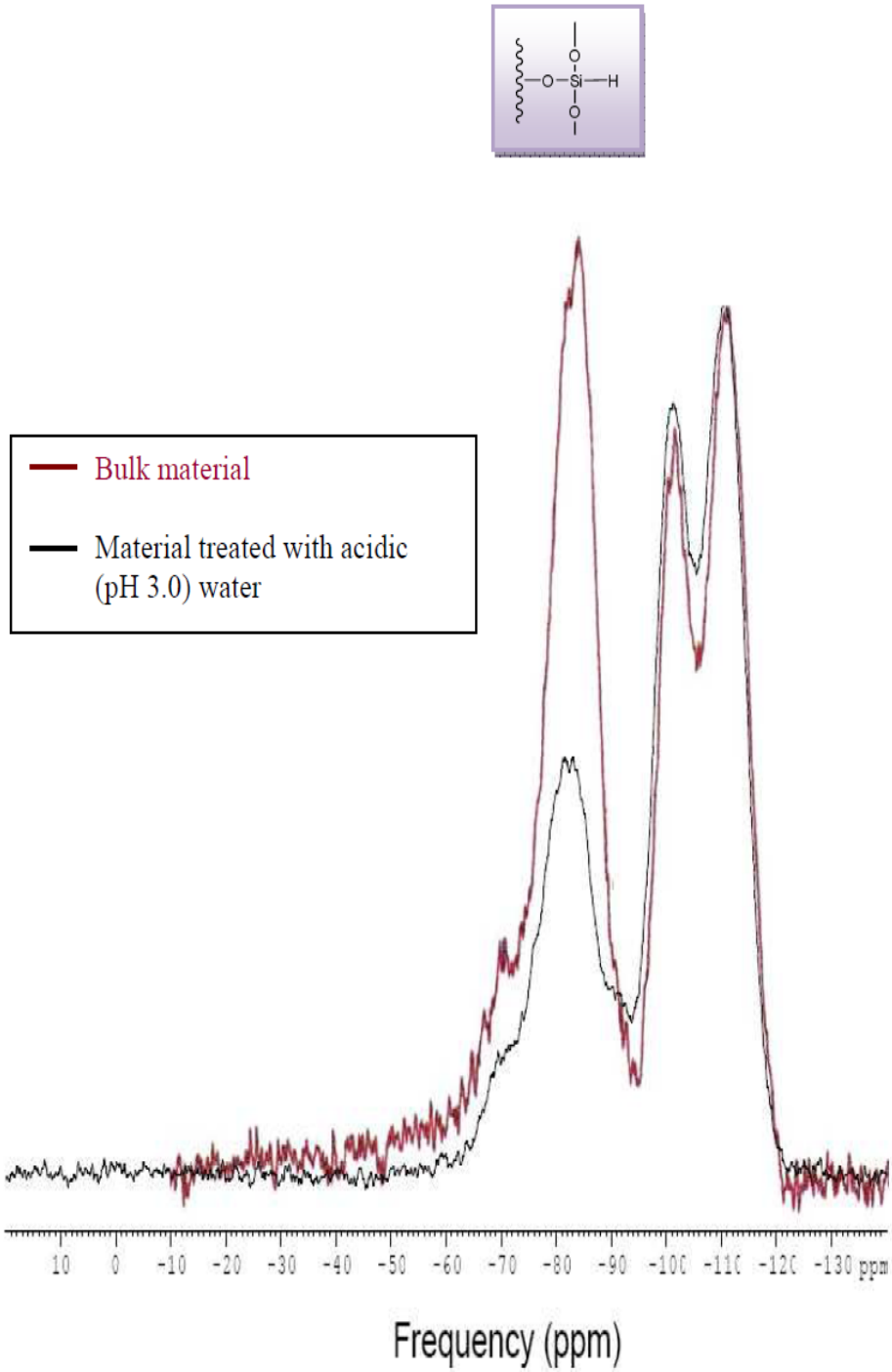

Figure 3.31. ^{29}Si CP-MAS spectra for bulk Cogent bidentate C_{18} and sample treated for five days with acidic water at pH 3.0.

Table 3.3. Effect of hydrolysis on the percentage distribution of the different peaks in the NMR spectra of Cogent bidentate C_{18}.

Chemical Moiety	**Percentage (% by peak area)**		
	Bulk material*	**Water (pH 7.0) treatment**	**Water (pH 3.0) treatment**
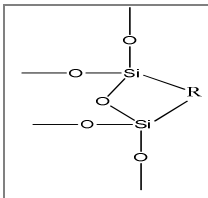	2.80 %	2.79 %	3.89 %
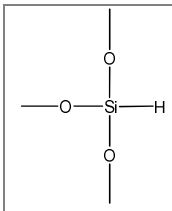	46.47 %	43.77 %	33.66 %
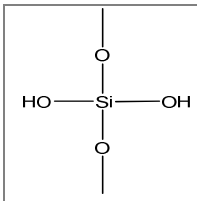	2.84 %	2.84 %	4.88 %
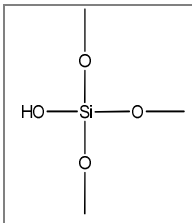	10.90 %	12.90 %	16.59 %
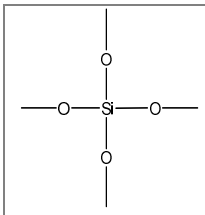	36.99 %	37.70 %	40.98 %

*Same as data as in Table 3.2.

CHAPTER 4

SUMMARY AND CONCLUSIONS

In this work, electrochemical detectors operated in the amperometric mode have been used to conduct a thorough investigation of heterogeneity for two categories of stationary phases commonly used in liquid chromatography. These categories are: particle-packed columns (columns studied were a 4.6 x 150mm HALO C18 column, packed with 2.7µm C18-bonded silica particles, and a 4.6 x 150mm LUNA C18 column, packed with 3µm C18-bonded silica particles); and monolithic columns (a 4.6 x 100 mm C18-bonded column, and a 10 × 100 mm Chromolith SemiPrep C18 column). The degree of each column's heterogeneity was assessed by measuring and mapping the radial distributions of the mobile phase velocity and efficiency at the exit cross section of each column. Furthermore, the technology used in fabricating the microelectrochemical detector was exploited to make an array of such detectors for online monitoring of eluent for a thin layer chromatographic bed (packed with 5µm silica gel material and measuring 10x10x0.1 cm). Finally, some novel unconsolidated bed material (Cogent bidentate C18 on type-C silica, XTerra MS C18, and XBridge Prep C18) were examined for their surface properties using solid state NMR.

All the chromatographic beds studied have a radially heterogeneous structure surrounding a fairly homogenous core. The elution profiles recorded at

the exit of these columns is not a simple consequence of the local axial dispersion, eddy dispersion, and mass-transfer phenomena taking place in these columns. It is strongly influenced by the radial heterogeneity of these columns.

For the particle-packed HALO and LUNA columns, the mobile phase velocities were found to be lower at the wall region by about 2.5-4.0%. Similarly, the efficiency was lower at this same wall region by about 35-50%. A denser packing of the wall region would be the consequence of the distribution of stress applied to the particles during the packing process, to their slippage with respect to each other and to the column wall, and to the strain distribution caused by this slippage. The higher strain regions are those where the local external porosity, hence the permeability, are reduced. In both cases, as demonstrated by our results, another net effect of the more heterogeneous wall region is a reduced local efficiency.

For the monolithic columns, the mobile phase velocity was found to be higher at the wall, while the efficiency was lower at this same wall region. The origin of the heterogeneity for the monolithic column described in this work is most likely the stress caused by the shrinkage of the monolithic rod during the process of its polymerization and drying. During this process, the silica layer close to the wall is inelastically deformed as it is pulled, and eventually snaps from the wall of the tube in which it is being prepared. The consequence of this is probably a slightly greater local porosity in the wall region, leading to a faster percolation of the mobile phase as evidenced by the higher mobile phase velocities recorded in the wall region. When the spatial distribution of the *A*, *B*,

and *C* terms of the Knox equation were determined for a SemiPrep monolithic column, the results demonstrate that the wall region of the column exhibits a greater tortuosity, as evidenced by the higher *A* values, and also a greater porosity, as evidenced by the smaller *C* values. Even though the monolithic rod is radially compressed during its encapsulation to shrink the external region of the silica layer, this compression is insufficient to compensate, to shrink back the silica layer, and to reduce sufficiently the initial expansion of the monolithic layer close to the wall, and to make radially homogeneous the distribution of the external porosity. The reason why this compression is insufficient may be explained by the silicagel having become more rigid during the last steps of the curing of the rod. The net effect is that the radial dependence of the local value of the mobile phase velocity causes a significant warping of the bands, hence an important loss of the column efficiency, as measured from the bulk detector signal.

Our savior faire in microelectrode fabrication was utilized in a setup that allows for online monitoring of eluent at the end of a flat wide column as well as an easy investigation of the lateral heterogeneity of the bed. Unlike traditional analyses made by thin layer chromatography where the detection of the sample components is made by scanning the bed using a spectrophotometer and making the relationship between the component concentrations and the signals detected quite complex, our approach was a far more practical one in that elution profiles are measured on-line in the same manner as it is done in HPLC. Our instrument construction allows for the mobile phase to flow out of the instrument

through a slit parallel to the bed exit edge, as a thin liquid curtain and over an array of microelectrochemical detectors. The instrument enables easy and accurate monitoring of the performance of the bed, its lateral homogeneity and the quality of the bed packing. This quality was assessed by measuring the retention times of p-benzoquinone at different locations and calculating the relative percent difference in retention times. The column bed was found to be fairly homogeneous and compared quite reasonably to those of columns used in HPLC.

Lastly, solid state CP-MAS NMR spectroscopy was used to detect the different chemical environments in which the silicon atoms exist on the surface of some novel solid packing materials used for HPLC columns. This allowed the observation of the surface substitution of silanol groups by hydrogen atoms and an estimate of the degree of surface coverage by Si-H for the Cogent type-C packing material. This coverage is high (~80%) for the bulk material. However, a significant surface density of silanol groups persists and this density increases when the Cogent material is treated with acidic water, preventing the surface from being inactive. Therefore, the hydrolytic instability of the Si-H bond is the point of reconciliation as this bond is hydrolyzed especially in acidic water to form silanol groups. Also, the ^{29}Si CP-MAS spectra obtained for the hybrid packing materials XTerra and XBridge show that there are silicon atoms in the structure of these adsorbents that are directly bonded to carbon atoms. This substitution of hydroxyl or siloxane groups by alkyl groups is not limited to the surface of the adsorbents but is a fundamental modification of the molecular structure of the

particles. By making relative comparisons between the T^2 and T^3 sites, it was determined that greater than 90% of the alkyl silicon atoms are within the completely condensed T^3 environments. The relative amount of Si-OH groups on the surface of the XTerra MS C_{18} and XBridge prep C_{18} is estimated to be ~ 2%. Therefore, a majority of silicon atoms are not bonded to silanol groups, which is consistent with earlier published chromatographic results showing that retention of basic compounds is at least an order of magnitude smaller on XTerra MS C_{18} than on Cogent or another conventional material prepared by derivatizing high-purity B-type silica particles with monofunctional silanes [107].

In conclusion, the recent advances in column technology that have lead to the development of materials like the Cogent type-C silica, the hybrid packing materials XTerra and XBridge, monolithic columns, and porous shell particle like the HALO should be applauded for their merits, as they have helped to extend the tools available to scientists in their quest to ameliorate different aspects in separation sciences, be it theoretical or practical. All columns investigated are not homogeneous but posses radial distributions of the mobile phase velocities and local column efficiencies. The root of all heterogeneity can be traced back to the manufacturing of the column. Granted, the results of this work do not provide any recommendations regarding possible improvements in the manufacturing process of columns. It might be that it is not possible to manufacture truly radially homogenous columns. However, it was worth investigating the heterogeneity and major contributions to band broadening in columns and to show that there are regions in the cross section of a column that contribute more than others to band

broadening. The demonstration of heterogeneity of the spatial structure may give us clues as to which stages of the manufacturing process may require some changes to ameliorate the overall column efficiency.

REFERENCES

[1] C. Poole, S. Poole, *Chromatography Today*, (1992) Elsevier, Amsterdam.

[2] D.J. Pietrzyk, P.R. Brown, R.A. Hartwick, *High Performance Liquid Chromatography*, (1989) Eds, Wiley, New York.

[3] L.R Snyder, J.J. Kirkland, *Introduction to Modern Liquid Chromatography*, (1977) 2nd Eds, Wiley, New York.

[4] L. C. Sander, S. A. Wise, *Crit. Rev. Anal. Chem.* **18** (1978) 299.

[5] J. Nawrocki, B. Buszewski, *J. Chromatogr.* **449** (1988) 1.

[6] R.E. Majors, *LC-GC.* **4** (1996) 214.

[7] G. Guiochon, A. Felinger, D. G. Shirazi, A.M. Katti. *Fundamentals of Preparative and Nonlinear Chromatography,* 2nd edition*,* Academic Press, Boston, MA (2006).

[8] G. Guiochon, T. Farkas, H. Guan - Sajonz, J.-H. Koh, M. Sarker, B. J. Stanley and T. Yun. *J. Chromatogr. A* **762** (1997) 83-88.

[9] J.H. Knox, G.R. Laird and P.A. Raven, *J. Chromatogr.* **122** (1976) 129.

[10] C.H. Eon, *J. Chromatogr.* **149** (1978) 29.

[11] J.E. Baur, E.W. Kristensen and R.M. Wightman, *Anal. Chem.* **60** (1988) 2334.

[12] J.E. Baur and R.M. Wightman, *J. Chromatogr.* **482** (1989) 65.

[13] T. Farkas, J.Q. Chambers, G.A. Guiochon, *J. Chromatogr. A*, **679** (1994) 231.

[14]T. Farkas, M.J. Sepaniak and G. Guiochon. *J. Chromatogr. A* **740** (1996) 169.

[15] E. Bayer, W. Müller, M. Ilg and K. Albert, *Angew. Chem. Intl. Ed.,* **28** (1989) 1029.

[16] U. Tallarek, E. Baumeister, K. Albert, E. Bayer and G. Guiochon. *J. Chromatogr. A* **696** (1995) 1.

[17] E. Bayer, E. Baumeister, U. Tallarek, K. Albert, G. Guiochon. *J. Chromatogr. A* **704** (1995) 37.

[18] E.J. Fernandez, C.A. Grotegut, G.W. Braun, K.J. Kirshner, J.R. Staudaher, M.L. Dickson and V.L. Fernandez, *Phys. Fluids* **7** (1995) 468.

[19] M.S. Smith and G. Guiochon, *J. Chromatogr. A* **827** (1998) 241.

[20] K. Freibaim, J. Knox, *Chromatographia* **19** (1984) 37-47.

[21] M. Martin, C. Eon, G. Guiochon, *J. Chromatogr.* **110** (1975) 213-32.

[22] J. Baur, H. Miller, M. Ritchadson, *Anal. Chimica Acta.* **397** (1999) 123-133.

[23] J. Baur, P. Wightman, *Anal. Chem.* **60** (1988) 2334-8.

[24] A. Fellinger, C. Pietrogrande, *Anal. Chem.* **73** (2001) 618-626.

[25] F. Gritti, I. Leornadis, D. Shock, P. Stevenson, *J. Chromatogr A.* **1217** (2010) 1589-1603.

[26] T. Farkas, G. Guiochon, *Anal. Chem*. **69** (1997) 4592.

[27] T. Farkas, M. J. Sepaniak, G. Guiochon, *AIChE J*. **43** (1997) 1464.

[28] B. Broyles, R. Shalliker, G. Guiochon, *J. Chromatogr. A.* **855** (1999) 367-382.

[29] K. S. Mriziq, J. A. Abia, Y. Lee, G. Guiochon, *J Chromatogr. A* **1193** (2008) 97.

[30] K. Miyabe, G. Guiochon, *J. Separat. Sci*. **27** (2004) 853.

[31] N. Vervoort, P. Gzill, G. V. Baron, G. Desmet, *J. Chromatogr. A* **1030** (2004) 177.

[32] K. Cabrera, *J. Sep. Sci*. **27** (2004) 843.

[33] A.-M. Siouffi, *J. Chromatogr. A* **1000** (2003) 801.

[34] F. Gritti, A. Cavazzini, N. Marchetti, G. Guiochon, *J. Chromatogr. A* **1157** (2007) 289.

[35] J. J. DeStefano, T. J. Langlois, J. J. Kirkland, *J. Chromatogr. Sci*. **46** (2008) 254.

[36] J. R. Mazzeo, U. D. Neue, M. Kele, *Anal. Chem*. **77** (2005) 460.

[37] U. D. Neue, M. Kele, *J. Chromatogr. A* **1149** (2007) 236.

[38] E. Heftmann, *Chromatography*, (1975) 3rd Eds, Van Nostrand Reinhold, New York, NY.

[39] A. Zlatkis, R.E. Kaiser, *High Performance Thin Layer Chromatography*, (1977) Elsevier, Amsterdam, The Netherlands.

[40] Z. Witkiewicz, J. Bladek, *J. Chromatogr.* **373** (1986) 111.

[41] F. Geiss, *Fundamentals of Thin-Layer Chromatography* (Planar Chromatography), (1987) Hüthig Verlag, Heidelberg, Germany.

[42] J.C. Touchstone, *Practice of Thin-Layer Chromatography,* (1992) Wiley, New York, NY.

[43] J. Sherma, B. Fried, *Handbook of Thin-Layer Chromatography*, (2003) Marcel Dekker, New York, NY.

[44] C.F. Poole, *J. Chromatogr. A* **1000** (2003) 963.

[45] C. F. Poole, *J. Chromatogr. A* **856** (1999) 399.

[46] M. Zakaria, M. Gonnord, G. Guiochon, *J. Chromatogr.* **271** (1983) 127.

[47] M. R. Schure, S. A. Cohen, *Multidimensional Liquid Chromatography: Theory and Applications in Industrial Chemistry and Life Science.* Wiley, NY.

[48] G. Guiochon, N. Marchetti, K. Mriziq, R. A. Shalliker, *J. Chromatogr. A,* **1189** (2008) 109.

[49] L.R. Snyder, J.J. Kirkland, *Introduction to Modern Liquid Chromatography*, Wiley, New York, 1974.

[50] C.F. Poole and S.K. Poole, *Chromatography Today*, Elsevier, Amsterdam, 2nd Ed., 1993 Section 4.3.

[51] H. Colin, P. Hilaireau, J. de Tournemire, *LC-GC*, 8 (1990) 302.

[52] D.-R. Wu, K. Lohse, *J. Chromatogr. A* **658** (1994) 381.

[53] M. Sarker and G. Guiochon, *J. Chromatogr. A*, **702** (1995) 27.

[54] J.N. Little, R.L. Cotter, J.A. Prendergast, and P.D. McDonald, *J. Chromatogr*. **126** (1976) 439.
[55] P.D. McDonald, R.V. Vivilecchia, D.R. Lorenz, *US Patent 4,211,658*, 1980.

[56] A. Berthod, *J. Liq., Chromatogr*. **12** (1989) 1187.

[57] C.W. Rausch, Y. Tuvin, U.D. Neue, *US Patent 4,228,007*,1980.

[58] G. Felix, K. Cabrera, D. Lubda, M. Roussel, *Chromatogria* **60** (2004) 3-8.

[59] F. C. Leinweber, D. Lubda, K. Cabrera, U. Tallarek, *Anal. Chem*. **74** (2002) 2470.

[60] F. Gritti, Y. Kazakevich, G. Guiochon, J. Chromatogr. A **1161** (2007) 157–169.

[61] J.J. van Deemter, F.J. Zuiderweg and A. Klinkenberg, *Chem. Eng. Sci*. **5** (1956), p.271.

[62] J.C. Giddings, *Dynamics of Chromatography*, Part 1, Marcel Dekker, New York (1965).

[63]N. Tanaka, H. Kobayashi, N. Ishizuka, H. Minakushi, K. Nakanishi, K. Hosoya, T. Itegami, *J. Chromatogr. A* **965** (2002) 35.

[64] J.F.K. Huber, *J. Chromatogr*. **7** (1969) 86.

[65] P. Bristow, J.H. Knox, *Chromatographia* **10** (1977) 219.

[66] A. M. Siouffi, *J. Chromatogr. A*, **1126** (2006) 86–94.

[67] P. Zollner, A. Leitner, D. Lubda, K. Cabrera, W. Lindnerl, *Chromatogria* **52** (2000) 818-820.

[68] R.A. Shalliker, B.S. Broyles, G. Guiochon, Anal. Chem. **72** (2000) 323.

[69] G. Guiochon, *J. Chromatogr. A* **1168** (2007) 101.

[70] H. Minakuchi, K. Nakanishi, N. Soga, N. Ishizuka, N. Tanaka, *Anal. Chem*. **68** (1996) 3498.

[71] Guiru Zhu, Qihua Yang, Dongmei Jiang, Jie Yang, Lei Zhang, Ying Li, Can Li *J. Chromatogr. A.* **1103** (2006), 257-264.

[72] J.J. Pesek, M. Matyska, *Chinese Journal of Chromatography* **23** (2005) 595-608.

[73] K. Unger, N. Becker, P. Roumeliotis, *J. Chromatog.* **125** (1976) 115.

[74] L. Zhanfei, M. Jingdong, P. Michael, L. Cindy, W. Stuartand, H. Patrick, *Geochimica et Cosmochimica Acta* **73** (2009) 1014-1026**.**

[75] G. R. Bogart, D. E. Leyden, T. M. Wade, W. Schafer, P. W. Carr, *J. Chromatogr*. **483** (1989) 209.

[76] K. Albert, E. J. Bayer, *J. Chromatogr.* **544** (1991) 345.

[77] K. Albert, R. Brindle, J. Schmid, B. BuszewskL E. Bayer, *Chromatographia* **38** (1994) 283.

[78] J.J. Pesek, M. T. Matyska, E. Soczewinski, P Christensen*, Chromatographia* **39** (1994) 520.

[79] J.J. Pesek, M. T. Matyska*, J. Chromatogr.* **667** (1994) 33.

[80] J. J. Pesek, M. T. Matyska, E. J. Williamsen, R. Tam, *Chromatographia* **41** (1995) 5.

[81] A. P. Legrand, *The Surface Properties of Silicas*, (1998) Wiley, Chichester.

[82] G. Maciel, C. Bronnimann, B. Hawkins, *Advances in Magnetic Resonance: The Waugh Symposium,* (1990) W. S. Warren, Ed., Academic Press, San Diego, 14, 125.

[83] G. Maciel, C. Bronnimann, R. Ziegler, S. Chuang, D. Kinney, A. Kettel, *The Colloid Chemistry of Silica* (H. E. Bergna, Ed.), **234** (1994).

[84] G. Maciel, P. Ellis, *NMR Techniques in Catalysis*, A. T. Bell, A. Pines, Eds. Dekker, New York, **231** (1994) 231.

[85] I. Chuang, G. Maciel, *J. Am. Chem. Soc.* **118** (1996) 401.

[86] S. Haukka, E. Lakornaa, A. Root, *J. Phys. Chem.* **97** (1993), 5085.

[87] M. Valtier, X. Drujon, M. Wilhelm, H. Spiess, *Macromol. Chem. Phys*. **202** (2001) 1262–1272.

[88] G. Engelhardt, D. Michel, *High resolution solid-state NMR of silicates and zeolites* (1987), John Wiley and Sons.

[89] A. Pines, M. Gibby, J. Waugh, *J. Chem. Phy*. **59** (1973) 569–590.

[90] K. Cabrera, Presented at the 31st International symposium on High Performance Chromatography and Related Techniques (HPLC-2007) Ghent, Belgium, June 17-21, 2007.

[91] N. Vervoort, H. Saito, K. Nakanishi, G. Desmet, *Anal. Chem*. **77** (2005) 3986.

[92] T. Yun, G. Guiochon, *J. Chromatogra. A* **760** (1997) 17-24.

[93] J. A. Abia, K. S. Mriziq, G. Guiochon, *J. Chromatogr A*, Submitted for publication.

[94] G. Guiochon, E. Drumm, D. Cherrak, *J. Chromatogr. A* **41** (1999) 835.

[95] B.G. Yew, E.C. Drumm, G. Guiochon, *AIChE J*. **49** (2003) 626.

[96] B.G. Yew, J. Ureta, R.A. Shalliker, E.C. Drumm, G. Guiochon, *AIChE J*. **49** (2003) 642.

[97] J. Abia, K. Mriziq, G. Guiochon, *J. Chromatogr. A*, **1216** (2009) 3185-3191.

[98] J. Abia, K. Mriziq, G. Guiochon. *J. Sep. Sci*. **32** (2009) 923-930.

[99] G. Guiochon, *J. Chromatogr. A* **1126** (2006) 6.

[100] Khaled S. Mriziq, Jude A. Abia, Youngmi Lee, George Guiochon, *J Chromatogr. A* **1193** (2008) 97-103.

[101] U. Tallarek, E. Bayer, G. Guiochon, *JACS* **120** (1998) 1494.

[102] S. Eeltink, W. M. C. Decrop, G. P. Rozing, P. J. Schoenmakers, W. Kok, *J. Sep. Sci*. **27** (2004) 1431.

[103] A.M. Siouffi, G. Guiochon, *J. Chromatogr. Sci.* **16** (1978) 470.

[104] K. Wyndham, J. O'Gara, T. Walter, K. Glose, N. Lawrence, B. Alden, G. Izzo, C. Hudalla, P. Iraneta, *Anal. Chem.* **75** (2003) 6781-6788.

[105] W. Sindorf, G. Maciel, *J. Am. Chem. Soc.* **105** (1983) 1487–1493.

[106] G. Maciel, W. Sindorf, *J. Am. Chem. Soc.* **102** (1980) 7606–7607.

[107] F. Gritti, C. Perdu, G. Guiochon, *J. Chromatogr. A,* **1180** (2008) 73–89.

Vita

Jude Atogho Abia was born on December 30, 1981 in Buea, Cameroon. He is married to Tomia Abia and have one daughter (Paris-Pearl Bessem Abia). Jude graduated from the University of Buea- Cameroon where he earned his BS degree in chemistry and materials technology and later moved to the United States of America in 2004 where he obtained an MS degree in chemistry at East Tennessee State University in 2006. He entered the doctoral program in chemistry at the University of Tennessee, Knoxville in August 2006 and earned his PhD in May 2010.